

Procedures for parameter estimates
of computational models for
localized failure

Proefschrift

ter verkrijging van de graad van doctor
aan de Technische Universiteit Delft,
op gezag van de Rector Magnificus prof. dr. ir. J.T. Fokkema,
voorzitter van het College voor Promoties,
in het openbaar te verdediging op 19 februari 2007 om 12:30 uur.

door

Cecilia IACONO

Laureata in Ingegneria Civile al Politecnico di Milano,
geboren te Ragusa, Italië.

Delft, 2007

Dit proefschrift is goedgekeurd door de promotoren:

Prof. dr. ir. L. J. Sluys

Prof. dr. ir. J. G. M. van Mier

Samenstelling promotiecommissie:

Rector Magnificus

Prof. dr. ir. L. J. Sluys

Prof. dr. ir. J. G. M. van Mier

Prof. dr. G. Maier

Prof. dr. ir. D. A. Hordijk

Prof. dr. ir. J. Carmeliet

Prof. dr. ir. J. G. Rots

Dr. ir. M. A. N. Hendriks

voorzitter

Technische Universiteit Delft, promotor

ETH Zurich, promotor

Politecnico di Milano

Technische Universiteit Eindhoven

Katholieke Universiteit Leuven

Technische Universiteit Delft

TNO DIANA BV.

This research is supported by the Dutch Technology Foundation (STW).

Copyright 2007, Cecilia Iacono.

Printed by Ponsen & Looijen B.V., The Netherlands.

All rights reserved. No part of this publication may be reproduced in any form, by print or photo print, microfilm or any other means, without written permission by the publishers.

*Dedicated to my parents,
to my husband Zaky,
to my daughter Leila.*

Acknowledgments

In the last years, I have been busy with two important projects. The first one has been my PhD research, carried out at the Faculty of Civil Engineering and Geosciences of Delft University of Technology, under the supervision of L. J. Sluys and J. G. M. van Mier. The present dissertation concludes this doctoral study, which has been financially supported by the Dutch Technology Foundation (STW). The second project has started later, affected the first project (a small delay in the time schedule), is self financed and it is a never ending project: the motherhood. The second project is performed under the highly demanding supervision of the two years old Leila El Hamel.

Here I would like to express my gratitude to all persons involved in the first project.

First of all, I thank Bert Sluys not only for his valid support as a supervisor, but also for his personal and friendly attitude. He always looked for my complete involvement in the decision making process of the main guide lines of the research, having understanding for all the delays imputable to all my efforts in the second project.

I am indebted to Jan van Mier for all his valuable suggestions and help, but also for his way of critically evaluating my results. His criticism has been always constructive and stimulating.

I am very grateful to Angelo Simone for having supplied the code related to the implementation of the gradient-enhanced model in the framework of the finite element program FEAP and also for his help and suggestions.

Further, I would like to acknowledge Chunxia Shi, Marcel van Vliet, Christian Feist and Karim Hariri, who kindly supplied the experimental results of their laboratory tests, fundamental for the solution of the analysed inverse problem.

Special thanks are due to Mrs. Dipl.-Phys. C. N. M. Jansz and to the entire STW users committee, specially to Ir. A. de Boer, also for having provided the numerical data used in Chapter 7, to Dr. ir. M. A. N. Hendriks and to Dr. ir. H. E. J. G. Schlangen, for the useful remarks, comments and feedback received during the periodical meetings.

Moreover, I sincerely thank Frank Everdij for his infinite patience and willingness in helping me in the struggles against my computer, Harm Askes for his valuable support in the programming part of my work, Federico Maggi for his appreciated advice in the use of the KNN method and Garth Wells for having given me the opportunity of experiencing some didactic activities besides my research work, as well as for their friendship.

I am grateful to all my colleagues and friends of TU Delft for having made my time enjoyable. In particular, my former room-mate Inna Gitman, Ahmed Elkadi, Tanyada Pannachet, Ivan Markovic, Sandra Pel, Ronnie Pedersen, Kristian Oelgaard, Peter Moonen, Ilse Vegt, Frank Radtke, Medhi Nikbakht, Giovanna Lilliu, Andrei Metrikine, Fabiana Maccarini, Alessandra Crosato, Andrea D'ariano, Stella Catalano.

I will be eternally grateful to my parents, constant source of support and encouragement, for having given to me the possibility of starting my scientific life and for enduring my being far away.

Last but not least an enormous thank to my husband Zaky, without whom this work would never have been possible, for his love, understanding and support in all the difficult and nervous moments and for his full time babysitting during the last conferences. I conclude with the biggest thank to my daughter Leila for having brought infinite happiness in my life, hoping that her supervision in the second project will never end for the rest of my life.....

Cecilia Iacono

Contents

List of symbols	iii
1 Introduction	1
1.1 Setting the problem	1
1.2 Scope and objectives of current research	2
1.3 Outline of the thesis	4
2 The forward problem	7
2.1 Softening, localization and size effect	7
2.2 Local damage model	9
2.3 Nonlocal damage model	12
2.3.1 Gradient enhanced damage formulation	14
2.4 The internal length scale	15
2.5 Governing equations of the forward problem	17
3 The inverse problem	21
3.1 Introduction	21
3.2 Inverse problems in Computational Mechanics	23
3.3 Setting an inverse problem	24
3.4 Inverse techniques	30
3.4.1 KNN method	32
3.4.2 Kalman Filter method	34
4 Experimental data	43
4.1 Series n. 1	43
4.2 Series n. 2	44
4.3 Series n. 3	45
4.4 Series n. 4	46

5	Numerical applications	49
5.1	Sensitivity analysis of model parameters	49
5.2	Inverse strategy implementation	53
5.3	KF method applications	55
5.3.1	Scalar KF procedure for c identification (KF _I and KF _{II})	57
5.3.2	Scalar KF procedure for β identification (KF _{III})	58
5.3.3	Bidimensional KF procedure for c and β identification (KF _{IV})	58
5.4	Uniqueness and stability of the solution	61
5.4.1	Global curve of one single size	62
5.4.2	Global curves of different sizes	74
5.5	Size effect	75
5.6	Global and local data	84
5.6.1	Global and local curves of one single size	84
5.6.2	Global and local curves of different sizes	99
5.6.3	Global and local curves of different sizes and different structures	103
6	Parameter identification strategy	105
6.1	Parameter identification procedure	105
7	Extension to other material models for localized failure	113
7.1	Higher order continuum models	114
7.2	Discrete crack models	114
7.3	Smeared crack model	115
7.4	Coupling data of different models	116
8	Conclusions and recommendations	119
8.1	Conclusions and achievements of the research	119
8.2	Open issues and future outlook	121
8.3	Recommendations	122
	Bibliography	125
	Summary	135
	Samenvatting	137
	Curriculum Vitae	139

List of symbols

Latin symbols

\mathbf{b}	body forces
c	gradient parameter ($= l^2/2$)
c_1	material parameter in the $\sigma - w$ law
c_2	material parameter in the $\sigma - w$ law
$d_{\text{comp}}^t(\mathbf{x})$	computational FPZ width at time t
d_{exp}^t	experimental FPZ width at time t
$\mathbf{d}_{\text{comp}}(\mathbf{x})$	computational vector of FPZ widths during fracture process
\mathbf{d}_{exp}	experimental vector of FPZ widths during fracture process
$\mathbf{e}^t(\mathbf{x})$	error between experimental and computational data ($= \mathbf{y}_{\text{exp}}^t - \mathbf{y}_{\text{comp}}^t(\mathbf{x})$)
f	loading function
$f(\mathbf{x})$	objective function in the inverse problem
f_{cc}	compressive strength
f_{ct}	tensile strength
$\mathbf{h}_t(\mathbf{x})$	forward operator at time t
l	length scale parameter
n_y	$\mathbf{y}_{\text{exp}}^t$ or $\mathbf{y}_{\text{comp}}^t$ vector dimension
n_x	\mathbf{x} vector dimension
\mathbf{n}	outward unit normal to Ω
p_1	weighting coefficient for the global data in $f(\mathbf{x})$
p_2	weighting coefficient for the local data in $f(\mathbf{x})$
s	standard deviation of repeated experiments
t	time, step
$\hat{\mathbf{t}}$	prescribed tractions
\mathbf{u}	displacement field
$\hat{\mathbf{u}}$	prescribed displacements
\mathbf{v}_t	experimental measurements noise
w	crack opening
w_c	critical crack opening (corresponding to zero stress in the $\sigma - w$ law)
x	Cartesian line coordinate
\mathbf{x}, \mathbf{y}	Cartesian spatial coordinates
\mathbf{x}	model parameters vector
$\hat{\mathbf{x}}_t$	mean value estimate of the model parameters vector at time t
$\hat{\mathbf{x}}_0$	initial guess of $\hat{\mathbf{x}}_t$

$\mathbf{y}_{\text{comp}}(\mathbf{x})$	computational data in a batch form
$\mathbf{y}_{\text{comp}}^t(\mathbf{x})$	computational data at time t
\mathbf{y}_{exp}	measured experimental data in a batch form
$\mathbf{y}_{\text{exp}}^t$	measured experimental data at time t
$\mathbf{y}_{\text{exp}}^*$	measurable response of the real system in a batch form
$\mathbf{y}_{\text{exp}}^{t*}$	measurable response of the real system at time t
$\mathbf{C}_{\text{exp}}^t$	experimental data covariance matrix at time t associated with $\mathbf{y}_{\text{exp}}^t$
$\hat{\mathbf{C}}_t$	model parameters covariance matrix at time t associated with $\hat{\mathbf{x}}_t$
$\hat{\mathbf{C}}_0$	initial model parameters guess covariance matrix associated with $\hat{\mathbf{x}}_0$
CMOD	crack mouth opening displacement of the specimen
\mathbf{D}^{el}	fourth-order linear elastic constitutive tensor linear elastic constitutive tangent matrix
E	Young's modulus
$E(\cdot)$	averaging operator
$F_{\text{comp}}^t(\mathbf{x})$	computational force applied to the specimen at time t
F_{exp}^t	experimental force applied to the specimen at time t
\mathcal{F}	symbolic representation of the Kalman filter process
G_f	fracture energy ($= \int \sigma dw$)
I_1'	first invariant of the strain tensor
J_2'	second invariant of the deviatoric strain tensor
\mathbf{K}_t	gain matrix at time t
\mathbf{L}	differential operator
\mathbf{N}	outward unit normal to Ω components matrix
P	probability density function
$P_{\mathbf{y} \mathbf{x}}$	conditional probability density function
RI	relative information index
\mathbf{S}_t	sensitivity matrix at time t

Greek symbols

α	softening parameter in damage evolution law
β	softening parameter in damage evolution law
ε_{eq}	local equivalent strain
$\bar{\varepsilon}_{eq}$	nonlocal equivalent strain

ε	strain tensor strain array in engineering notation
η	f_{cc}/f_{ct}
κ	deformation history variable
κ_i	strain threshold of damage initiation
κ_{max}	maximum value of equivalent strain
ν	Poisson's ratio
ρ	distance between points \mathbf{x} and \mathbf{y}
σ	stress tensor stress array in engineering notation
ψ	Gauss weight function in nonlocal averaging
ω	scalar damage variable
Ψ	weight function in nonlocal averaging
Ω	body volume or surface or length
$\partial\Omega$	boundary surface of Ω
$\partial\Omega_t$	boundary surface of Ω with prescribed tractions
$\partial\Omega_u$	boundary surface of Ω with prescribed displacements

Chapter 1

Introduction

1.1 Setting the problem

In the last three decades there has been an increasing interest in the study of the tensile behavior of concrete or, more generally, of quasi-brittle materials, and its role in the assessment of the performance of structures. Many computational models have been developed (following either the discrete modelling or the continuum modelling approach) to reproduce tensile fracture phenomena occurring in quasi-brittle materials.

Assuming that these models are capable of correctly describing the fracture process according to a qualitative point of view, their reliability, in reproducing quantitatively correct results, significantly relies on the identification of the constants characterizing the model equations (model parameters). However, some model parameters are defined at the material point level (constitutive law equations) and their real physical interpretation is not always clearly established. This is the case, for instance, for the length scale parameter, introduced in the nonlocal continuum models in order to regularize the local approach. Direct experimental estimates of these parameters are not possible and the parameter identification problem needs to be solved in the framework of the Inverse Problems Theory. The development of inverse procedures is required, which can provide the parameters estimate by minimizing, iteratively, the discrepancy between experimental and computational data. Hence, innovative computational and experimental techniques may be coupled to extract intrinsic material properties from measured structural responses.

1.2 Scope and objectives of current research

Scientific modelling of natural processes provides relations between causes and effects. Hence, considering the scheme of Figure 1.1, the following cases may be distinguished, according to the type of unknowns of the problem:

- the effects are unknown \implies the *forward problem* has to be solved;
- the causes are unknown \implies the *inverse problem* has to be solved;
- the model is unknown \implies both the forward and the inverse problem have to be solved.

In fact, solving the forward problem means to find analytical or numerical solutions for ordinary or partial differential equations with known initial conditions, boundary conditions and constants (or parameters) in the equations. On the contrary, in the inverse problem the solution is known and the objective is to determine the complete forward problem for which that solution is possible. When developing a model, which can be used for prediction or design purposes, the following three phases can be identified:

a) Model building

- idealization and simplification of the physics and/or mechanisms on the basis of the real process/phenomenon;
- conversion into equations or mechanical system(s);
- solution of a forward problem (causes and model are known);
- check on the model output: the response reproduced by the model should be *qualitatively* acceptable after comparison with the real response.

b) Model calibration

- A *real* situation (causes and effect known) is considered. The model is formulated, but not entirely, since model parameter estimation is necessary. Hence, an inverse problem needs to be solved for the model parameter identification. Starting from an initial guess of the model

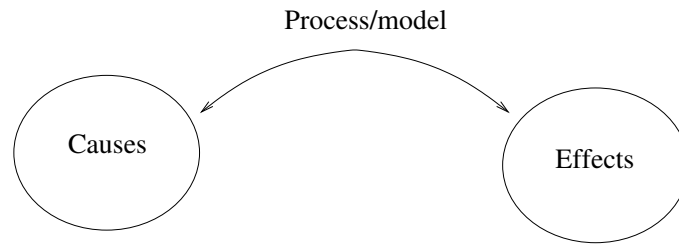


Figure 1.1: Modelling scheme of processes.

parameters, the computational output is compared to the known experimental response of the modelled system. On the basis of the discrepancy between the two outputs, the parameters estimate may be iteratively or directly updated.

This represents a first check for the model, because, already in this phase, weak points in the model may be detected. For instance, the solution of the inverse problem might not exist or it might be unstable.

However, error identification may require a significant effort, since causes of ill-posedness might not only be found in the model, but also in the type of experimental data used for the calibration (quality, quantity and type of data) or in the adopted inverse method (for instance, local searching techniques might stick into local minima of the function of the discrepancy between the computational and experimental data, whose minimization represents the identification process).

c) Model assessment

- various real situations are considered, *different* from the one(s) used for the model calibration, but still in the valid application range of the model (because they satisfy the assumptions on which the model is based). Forward problems are solved and a comparative study between the experimental and computational responses is performed. Hence, limits related to the predictive capacities and to the applicability of the model can be provided, establishing the conditions under which the model performs well and under which it fails.

The present thesis is situated mainly in phase b) and partially in phase c) of nonlocal continuum models for localized fracture in quasi-brittle material

and, particularly, of the gradient-enhanced continuum damage model¹. The first phase of the model development is not discussed. However, as already pointed out, if, on one hand solving a calibration problem neglects a debate on the model (the way the process has been modelled), on the other hand, *at the end* of this phase or in the model assessment phase, the presence of possible weak points can be highlighted. Hence, the inverse analysis might reveal limits in the basic assumptions of the model. A ‘proof ab absurdo’ of the model can be provided by the inverse analysis: starting from the hypothesis that the way the model describes the physical process is correct, possible flaws might be found, that lead to re-discuss the hypotheses, which give input when going back to phase a) of the model development.

Related to the identification of the parameters of nonlocal continuum models for localized failure in quasi-brittle materials, limited, though interesting, studies are available in literature (e.g. [22, 38, 55, 58]). However, the main issues remain the investigation of the well-posedness of the inverse problem (also influenced by the choice of experimental data, in terms of quality and quantity, involved in the solution), the choice of the adopted inverse strategy (as a suitable searching scheme in terms of effectiveness, efficiency and robustness) and the assessment of the so-calibrated numerical model (in terms of reliability, limits of the applicable domains and predictive capabilities). All these aspects are analyzed in the present work, examining issues related both to the *forward* model and to the *inverse* parameter identification problem.

1.3 Outline of the thesis

The essential phenomenological aspects of quasi-brittle materials and the numerical model used to reproduce these phenomena are presented in Chapter 2. Hence, this chapter is devoted to the forward problem and to some issues related to the length scale parameter characterizing nonlocal continuum models. The inverse problem is discussed in Chapter 3, presenting the inverse techniques used in the thesis. The solution of the inverse problem needs experimental results as target solutions. The experimental tests used for this purpose are reported in Chapter 4. In Chapter 5 the numerical applications are described. Hence, containing the main findings, Chapter 5 represents the core of the work. The developed inverse strategy for parameter identification, derived from the results in Chapter 5, is presented in Chapter 6. How

¹The optimal experiment design is not part of the scope of this thesis.

this strategy and the adopted inverse techniques may be extended to other material models for localized failure is discussed in Chapter 7. Finally, the summary of the main conclusions and achievements of the research, the open issues and future outlook and recommendations are presented in Chapter 8.

Chapter 2

The forward problem

2.1 Softening, localization and size effect

Deformation controlled tensile tests of quasi-brittle materials (such as concrete, rock and ice) are characterized by a gradual *softening* after reaching the maximum load. In a one-dimensional stress-strain relation or load-deformation relation, this means that after the peak load has been reached, the load-carrying capacity decreases until complete failure, as a result of collaborative structural and material effects. The distinction between aspects related only to the structural or to the material behaviour is very difficult, because structural effects may be minimized but never avoided. As a matter of fact, the causes of the softening behaviour are the irreversible processes of fracturing that first occur at the micro-level in the material and then, through the growth and coalescence of microcracks, at the macro-level, influenced by structural aspects (e.g. geometry, boundary and loading conditions) manufacturing factors and environmental conditions.

At a certain stage of the loading process, deformations grow in a small portion of the specimen, leading to strain *localization* phenomena which are responsible for the macroscopic failure of the structure. Hence, while damage continues to increase in a limited part of the structure, other parts unload releasing the elastically stored energy. The characteristic localization width, for a given structure, is material-dependent and therefore it represents additional experimental information that may be exploited in the parameter identification procedure.

The phenomenological behaviour of quasi-brittle materials presents another important aspect. Numerical and experimental investigations by many

researchers demonstrated the *size effect* phenomenon: the results obtained in the laboratory are influenced by the size of the specimen. Particularly, many models deal with the size effect on the nominal strength. In this category the Weibull weakest link theory [91], Bažant's Size Effect Law [2] and the Multi Fractal Scaling Law by Carpinteri [23] are the most well known. The real mechanisms that are behind the size effect phenomenon are not yet completely understood and they have been the topic of an extensive scientific discussion. The opinion of the author is that the stress-redistribution, consequence of micro and macrocracking, that are at the basis of the size effect phenomena, are governed by structural factors and by intrinsic local properties of the material [85]. In other words, the size effect is governed by deterministic and statistical phenomena. The boundary and loading conditions in the tensile experiments, for instance, are structural factors that have an important effect on the tensile strength and on the failure mechanism of the specimen: free or fixed rotations (together with the stiffness of the specimen) may or may not allow for some stress-redistribution after microcracking in the pre-peak regime [84]. On the other hand, particle density, particle distribution, relative stiffness, strength and amount of the constitutive phases of an heterogeneous medium define the intrinsic properties of the material influencing the local microcracking processes. Finally, differential deformations due to the hydration heat and drying and other manufacturing and environmental factors cause different local eigen-stresses depending on the size of the specimen. Small specimens, for instance, are relatively more affected by non-uniform drying than large specimens, since the effects are limited to the body skin and small size specimens have a bigger surface to volume ratio. Interesting investigations regarding the parameter identification problem are based on size effect phenomena (e.g. [22, 55, 73, 81]).

From the numerical point of view, over the past two decades, the simulation tools used in mechanics of materials have become increasingly powerful. Progress made in the field of scientific computation is giving rise to a new branch of mechanics called computational mechanics of solids [50], allowing the use of more realistic and more complex models. In the case of fracture behaviour of quasi-brittle materials, it may be numerically modeled following a *discrete* or a *continuum* approach. In the first case the failure of the mechanical system is reproduced by the definition of a fracture criterion and a cohesive law along the crack and linear elastic relations in the remaining part. In the second case, instead, the loss of mechanical integrity is accounted for in the constitutive relations. A zone of material degradation and local-

ized deformation, according to the standard continuum mechanics theory, represents fracture.

Of course, the complete computational descriptions of all the phenomenological aspects described above is very difficult and any discussion about the potentiality of continuum models versus discrete models, which is topic of a scientific debate in the last years, is neglected here. However, it suffices here to mention that the calibration of a numerical model reduces to a merely data fitting problem, if the parameter identification process is not driven by a critical assessment and awareness of the limits of applicability and of predictive capability of the model.

In the present work the continuum approach is chosen and briefly presented in this Chapter. However, many issues of the inverse problem remain valid also for other computational models. A discussion on this issue is added in Chapter 7.

2.2 Local damage model

The adopted numerical model is based on the isotropic continuum damage formulation of Lemaitre and Chaboche [56]. The material degradation due to thermal or chemical effects is neglected and only the damage caused by nucleation, coalescence and growth of microcracks is taken into account through a scalar damage variable ω . All dissipation phenomena are related to the growth of microcracks and therefore to the degradation of the elastic constitutive moduli, while plastic deformations are neglected. This model can describe the quasi-brittle fracture mechanisms in which a high number of micro-structural changes occurs before complete failure of the material takes place.

The range for ω is in the interval $[0,1]$: if $\omega = 0$ no damage has developed in the material that remains in the initial virgin state, while $\omega = 1$ corresponds to the completely damaged material without any residual load-carrying capacity. The damage scalar variable ω is responsible for the degradation of the elastic stiffness according to the following classical stress-strain relation

$$\boldsymbol{\sigma} = (1 - \omega)\mathbf{D}^{el}\boldsymbol{\varepsilon}, \quad (2.1)$$

in which \mathbf{D}^{el} represents the matrix of the virgin elastic stiffness moduli, governing the response of the undamaged material ($\omega = 0$) and $\boldsymbol{\sigma}$ and $\boldsymbol{\varepsilon}$ denote stress and strain, respectively. During damage evolution ω increases, reducing

the stress that can be transferred until complete failure of the material ($\omega = 1$) when the stiffness and load-carrying capacity has vanished.

A scalar invariant measure of strain, the equivalent strain ε_{eq} , is defined as function of the strain tensor components. Different definitions of ε_{eq} can be formulated [70] and here only the modified von Mises definition [90], adopted in the applications discussed in the thesis, is given

$$\varepsilon_{eq} = \frac{(\eta - 1)I'_1}{2\eta(1 - 2\nu)} + \frac{1}{2\eta} \sqrt{\frac{(\eta - 1)^2 I_1'^2}{(1 - 2\nu)^2} + \frac{12\eta J_2'}{(1 + \nu)^2}}, \quad (2.2)$$

where I'_1 and J'_2 are the first invariant of the strain tensor and the second invariant of the deviatoric strain tensor, respectively, given by

$$I'_1 = \varepsilon_{xx} + \varepsilon_{yy} + \varepsilon_{zz} \quad (2.3)$$

and

$$J'_2 = (\varepsilon_{xx}^2 + \varepsilon_{yy}^2 + \varepsilon_{zz}^2 - \varepsilon_{xx}\varepsilon_{yy} - \varepsilon_{yy}\varepsilon_{zz} - \varepsilon_{zz}\varepsilon_{xx})/3 + \varepsilon_{xy}^2 + \varepsilon_{yz}^2 + \varepsilon_{zx}^2. \quad (2.4)$$

In Eq. (2.2) η is a model parameter that represents the sensitivity in compression relative to that in tension. It is given by the ratio of the compressive and the tensile strength of the material: $\eta = f_{cc}/f_{ct}$. According the equivalent strain definition of Eq. (2.2), compressive and tensile actions of the same magnitude on the material have different effects on the damage growth only if $\eta \neq 1$.

As long as the equivalent strain ε_{eq} is smaller than a strain threshold κ_i , no damage occurs in the material that remains in the linear elastic regime. Damage growth is determined by means of a damage loading function which is expressed in terms of the equivalent strain

$$f(\varepsilon_{eq}) = \varepsilon_{eq} - \kappa(\varepsilon_{eq}), \quad (2.5)$$

where κ is a history variable representing the most severe deformation undergone by the material

$$\kappa(\varepsilon_{eq}) = \max(\varepsilon_{eq}, \kappa_{max}), \quad (2.6)$$

being κ_{max} the maximum value of equivalent strain occurred in the material. However, when $\varepsilon_{eq} = \kappa_i$ the damage process starts, evolving according to a damage evolution law

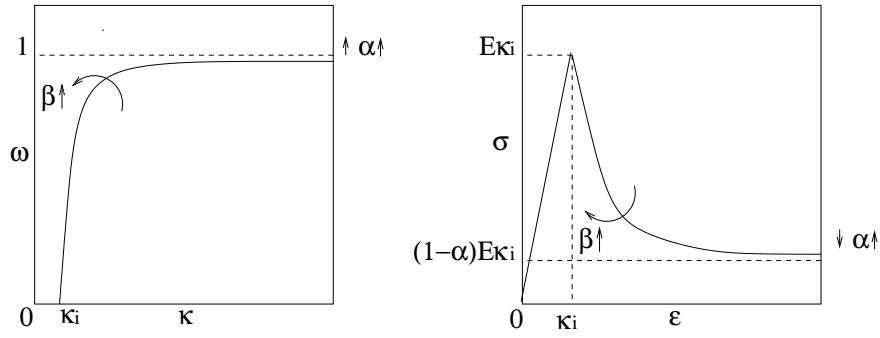


Figure 2.1: (a) Exponential softening damage evolution law (b) uniaxial stress-strain curve.

$$\omega = \omega(\kappa). \quad (2.7)$$

The magnitude of the loading function is governed by the Kuhn-Tucker relations

$$f\dot{\kappa} = 0, \quad f \leq 0, \quad \dot{\kappa} \geq 0. \quad (2.8)$$

For $f < 0$ no growth of damage can take place ($\dot{\kappa} = 0$) and the response remains linear elastic. Damage increases ($\dot{\kappa} > 0$) only if the strain state satisfies the equation $f = 0$ and during this increment the consistency condition $\dot{f} = 0$ must be satisfied as well.

The complete formulation of the model requires the explicit definition of the damage evolution law Eq. (2.7). Here, the following *exponential softening* damage evolution law is chosen

$$\omega = 1 - \frac{\kappa_i}{\kappa} [1 - \alpha + \alpha e^{-\beta(\kappa - \kappa_i)}], \quad (2.9)$$

where α and β are two additional model parameters that govern the softening curve. As schematically represented in Figure 2.1, α determines the residual stress of the damaged material and β sets the negative slope of the softening branch.

However, strain localization arising from a material instability poses considerable difficulties in numerical solutions. In fact, the standard local damage model presented above can reproduce the global softening behaviour of the material, but it presents what is commonly known as *mesh dependence*. The

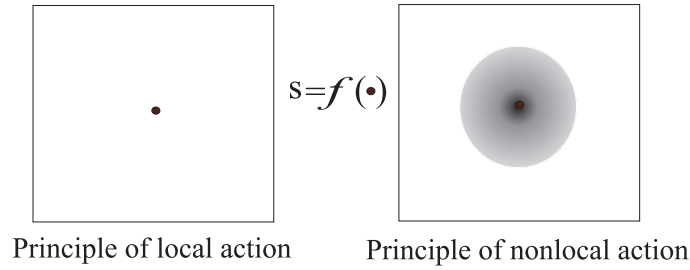


Figure 2.2: The principle of local and nonlocal action [37].

width of the zone where damage localises depends on the used finite element size: decreasing the element size leads to a decrease of the strain localisation band and, consequently, the numerical analysis depends on the spatial discretisation. In the limit case the growth of damage tends to localise in a portion of material of zero volume, the crack propagation becomes instantaneous and no work is necessary to produce the fracture process (zero fracture energy). This non physical behaviour, predicted by the local damage theory, is mathematically explained by a local loss of ellipticity of the set of partial differential equations governing the rate of deformation. The boundary value problem becomes ill-posed, i.e. it does not have a unique solution with continuous dependence on the given data (an infinitesimal change in the data can cause a finite change in the solution). To recover the mathematical well-posedness of the boundary value problem a length scale must be incorporated, implicitly or explicitly, into the material description or into the formulation of the problem. A number of approaches have been proposed in the last years [25, 77] to remedy this difficulty, giving rise to different types of *regularized* models. The model adopted here belongs to the class of nonlocal regularized models.

2.3 Nonlocal damage model

The basic idea of the nonlocal model is that a state variable in a material point depends on state variables (and/or history) in the considered point (local action principle) and in the neighboring points (see Figure 2.2). The introduction of this principle of nonlocality in the constitutive equations was first considered by Kröner [49] and Eringen and Edelen [31]. It was first applied to regularization of material instability problems using imbricate el-

ements by Bažant *et al.* [4] and Belytschko *et al.* [14] for strain-softening materials and then applied to continuum damage mechanics by Pijaudier-Cabot and Bažant [10, 72], with several versions of nonlocal models later proposed by Bažant and co-workers [6, 8] based on similar concepts. Many studies, applications, developments and enrichment have later emerged from the nonlocal damage theory [5, 18, 26, 52, 90, 93].

The nonlocality in the constitutive model may be introduced in different ways: directly in the constitutive equation $\boldsymbol{\sigma}(\boldsymbol{\varepsilon})$ or, alternatively, in the evolution law of an internal variable. Within continuum damage mechanics, the nonlocality is usually embedded in the damage evolution. The constitutive relation Eq. (2.1) remains unaltered, while the computation of damage is modified through the following history variable definition, substituting Eq. (2.6) by

$$\kappa(\bar{\varepsilon}_{eq}) = \max(\bar{\varepsilon}_{eq}, \kappa_{max}), \quad (2.10)$$

where $\bar{\varepsilon}_{eq}$ is the so-called nonlocal equivalent strain. In the nonlocal damage theory the nonlocal equivalent strain $\bar{\varepsilon}_{eq}$ can be defined as a spatially averaged quantity and, as a consequence, a smooth damage field is obtained avoiding the ill-posedness of the boundary value problem and the mesh sensitivity of the discretised problem as discussed for the local approach. The definition of the non local equivalent strain is given by

$$\bar{\varepsilon}_{eq}(\mathbf{x}) = \frac{1}{\Psi(\mathbf{x})} \int_{\Omega} \Psi(\mathbf{y}; \mathbf{x}) \varepsilon_{eq}(\mathbf{y}) d\Omega, \quad (2.11)$$

where \mathbf{y} points to the positions of the infinitesimal volume $d\Omega$ and $\Psi(\mathbf{x})$ is defined as

$$\Psi(\mathbf{x}) = \int_{\Omega} \Psi(\mathbf{y}; \mathbf{x}) d\Omega. \quad (2.12)$$

The weighted average is defined such that for homogeneous strain states the local and nonlocal equivalent strain are equal. As weighting function $\Psi(\mathbf{y}; \mathbf{x})$ the homogeneous and isotropic Gauss distribution is usually adopted

$$\psi(\rho) = \frac{1}{(2\pi)^{3/2} l^3} \exp\left[-\frac{\rho^2}{2l^2}\right], \quad (2.13)$$

where $\rho = |\mathbf{y} - \mathbf{x}|$ and the factor $(2\pi)^{-3/2} l^{-3}$ normalizes the weight function such that in \mathbb{R}^3

$$\int_{\mathbb{R}^3} \psi(\rho) d\Omega = 1. \quad (2.14)$$

The length parameter l in Eq. (2.13) gives the size of the neighborhood that determines the nonlocality of the model.

2.3.1 Gradient enhanced damage formulation

Instead of an integral type nonlocal model also a differential type nonlocal model may be used, a so-called gradient model. For instance, gradient plasticity models have been derived [63, 78]. For sufficiently smooth fields of the local equivalent strain, it is possible to apply a Taylor series expansion [71]

$$\begin{aligned} \varepsilon_{eq}(\mathbf{y}) = & \varepsilon_{eq}(\mathbf{x}) + \frac{\partial \varepsilon_{eq}}{\partial x_i} (y_i - x_i) + \frac{1}{2!} \frac{\partial^2 \varepsilon_{eq}}{\partial x_i \partial x_j} (y_i - x_i)(y_j - x_j) + \\ & \frac{1}{3!} \frac{\partial^3 \varepsilon_{eq}}{\partial x_i \partial x_j \partial x_k} (y_i - x_i)(y_j - x_j)(y_k - x_k) + \\ & \frac{1}{4!} \frac{\partial^4 \varepsilon_{eq}}{\partial x_i \partial x_j \partial x_k \partial x_l} (y_i - x_i)(y_j - x_j)(y_k - x_k)(y_l - x_l) + \dots \end{aligned} \quad (2.15)$$

Substituting Eq. (2.15) into Eq. (2.11) and carrying out some calculus for the problem in \mathbb{R}^3 , the integral Eq. (2.11) can be rewritten as a differential equation in terms of gradients of the local equivalent strain ε_{eq}

$$\bar{\varepsilon}_{eq}(\mathbf{x}) = \varepsilon_{eq}(\mathbf{x}) + \bar{c}_2 \nabla^2 \varepsilon_{eq}(\mathbf{x}) + \bar{c}_4 \nabla^4 \varepsilon_{eq}(\mathbf{x}) + \dots, \quad (2.16)$$

where the Laplacian ∇^n is defined by $\nabla^2 = \sum_i \partial^2 / \partial x_i^2$, $\nabla^{2n} = (\nabla^2)^n$ and the coefficients by $\bar{c}_2 = (1/2)l^2$ and $\bar{c}_4 = (1/8)l^4$.

Odd derivative terms vanish in Eq. (2.16) for the problem in \mathbb{R}^3 as a consequence of the isotropy of the Gaussian weight function, while this is no longer true for a problem in finite domains $\Omega \subset \mathbb{R}^3$. However Eq. (2.16) remains an approximation of the integral Eq. (2.11).

Multiplying Eq. (2.16) with $\bar{c}_2 \nabla^2$ and subtracting the result from Eq. (2.16) the following relation can be obtained [70]

$$\bar{\varepsilon}_{eq} - \bar{c}_2 \nabla^2 \bar{\varepsilon}_{eq} = \varepsilon_{eq} + (\bar{c}_4 - \bar{c}_2^2) \nabla^4 \bar{\varepsilon}_{eq} + \dots \quad (2.17)$$

Neglecting terms of order four and higher in the right-hand side of Eq. (2.17) yields

$$\bar{\varepsilon}_{eq} - c\nabla^2\bar{\varepsilon}_{eq} = \varepsilon_{eq}, \quad (2.18)$$

where it has been assumed that $\bar{c}_2 = c$. Eq. (2.18) is the differential approximation of the integral Eq. (2.11) and, since the nonlocal variable $\bar{\varepsilon}_{eq}$ depends implicitly on the corresponding local variable ε_{eq} , it is referred to as an *implicit gradient-enhancement* [70].

The solution of Eq. (2.18) requires extra boundary conditions. Two different boundary conditions may be given

$$\bar{\varepsilon}_{eq} = \hat{\varepsilon} \quad \text{Dirichlet boundary condition,} \quad (2.19)$$

$$\mathbf{n}^T \nabla \bar{\varepsilon}_{eq} = \hat{\varepsilon}_n \quad \text{Neumann boundary condition,} \quad (2.20)$$

where \mathbf{n} is the boundary unit normal. In most cases the natural boundary condition is used even if the physical interpretation of it is still an open issue

$$\mathbf{n}^T \nabla \bar{\varepsilon}_{eq} = 0 \quad \text{natural boundary condition.} \quad (2.21)$$

2.4 The internal length scale

The length scale l (or alternatively the gradient parameter c) is an additional parameter that is necessarily introduced in the constitutive equations to regularize continuum models. In fact, without the length scale parameter, the strain-softening continuum models for damage can only correctly describe situations in which the damage remains distributed and not localised. The length scale gives information on the limited possible volume in which damage may localise, so that it is called *localization limiter*.

Moreover, only with the introduction of the length scale the failure models may describe the size effect phenomena. Therefore, fitting of the size effect curve is often used for the identification of the length scale parameter (e.g. [22, 55]).

However, it remains unclear whether this model parameter represents only a mathematical trick to remedy the loss of ellipticity of the governing equations or that it can be considered as a material property related to the microstructure of the material. As a matter of fact, interesting studies have been made to justify the length scale in the nonlocal approach by microstructure [11] and physical justifications. The introduction of the principle of nonlocal action is suggested by micromechanics motivations in [3, 9]. Two arguments

seem to be relevant: (i) the inelastic strain caused by damage is the consequence of the release of stored energy from a microcracked neighborhood, the size of which is not negligible (ii) the interaction among microcracks in a certain neighborhood implies nonlocality. The size of this neighborhood or interaction radius depends on the characteristic micro-structure of the material and it is related to the length scale, which supports the necessity of introducing information on the microlevel in the constitutive model. In fact, an important continuum model requirement for a brittle heterogeneous material such as concrete, for instance, is that it must correctly represent the consequences of heterogeneity of the microstructure. This can be taken into account by the use of the nonlocal concept and so of the length scale parameter, which permits to obtain a microstructural dependent model. Hence, the internal length scale may be considered as a mathematical tool necessary to translate the mechanics of the discrete microstructure into a continuum approach.

Although some studies indicate a fixed ratio between l and the maximum aggregate size (e.g. [11, 59, 60]), the optimum values of that ratio show substantial variation from one type of structure to another [67]. Hence, it is suggested to consider the length scale not as a material constant but as a material function depending on the structure (e.g. bending vs. tension tests) and on the stress-strain field in the neighborhood of a point, especially for points in the fracture process zone.

In addition, other researchers [34, 38, 62, 68, 85] conclude that the internal length scale depends on the initial undamaged microstructure and also on all deformation mechanisms occurring during the damage process. These mechanisms change the microstructure in a progressive way. In other words, the length scale could not be constant during the entire fracture process, but it could be variable according a suitable evolution law, for instance, in terms of cracking strain or damage variable, in a sort of self-adaptive strategy implemented at the level of the material constitutive law.

All the hypotheses that consider the possibility of an internal length scale that is not a constant material parameter rise essentially from two facts: i) only one parameter can not be sufficient to describe all the complex microstructural processes that characterize the material behaviour and which define the response at the structural level, ii) the nonlocal continuum approach suffers from the drawback of preserving continuum mechanics, whereas, due to crack propagation, a transition from a continuous towards a discontinuous medium actually occurs [33, 76].

Regardless of the interpretation of the length scale, this model parameter can not be directly measured during laboratory tests and direct accurate links between l and any measurable microscopic material property have not been established. Hence, only by using inverse problem methods, as valid tools for extracting local material parameters from structural experimental response, the length scale parameter may be estimated and the related issues can be investigated [22, 38, 55, 58]. However, the main issues remain the well-posedness of the identification problem (also influenced by the choice of experimental data, in terms of quality and quantity, involved in the solution), the choice of the adopted inverse technique (as a suitable searching tool in the parameters space that is capable of avoiding eventual sticking into local minima) and the assessment of the so calibrated numerical model (in terms of reliability, validity domains and predictive capabilities). All these aspects are analyzed in the present work.

2.5 Governing equations of the forward problem

Let Ω be an open bounded domain of \mathbb{R}^d , with $d = 1, 2, 3$ representing a general mechanical system. If $\partial\Omega$ is defined as the continuous boundary of Ω , it can be split into two parts: $\partial\Omega_u$ where displacements $\hat{\mathbf{u}}$ are prescribed and $\partial\Omega_t$ where surface tractions $\hat{\mathbf{t}}$ are prescribed. The equilibrium and kinematics of the system, under the action of body forces \mathbf{b} and surface tractions $\hat{\mathbf{t}}$, assuming the hypothesis of small deformations, are governed by the following set of equations

$$\mathbf{L}^T \boldsymbol{\sigma} + \mathbf{b} = \mathbf{0}, \quad (2.22)$$

$$\boldsymbol{\varepsilon} = \mathbf{L}\mathbf{u}, \quad (2.23)$$

where the differential operator \mathbf{L} is defined as

$$\mathbf{L}^T = \begin{bmatrix} \frac{\partial}{\partial x} & 0 & 0 & \frac{\partial}{\partial y} & 0 & \frac{\partial}{\partial z} \\ 0 & \frac{\partial}{\partial y} & 0 & \frac{\partial}{\partial x} & \frac{\partial}{\partial z} & 0 \\ 0 & 0 & \frac{\partial}{\partial z} & 0 & \frac{\partial}{\partial y} & \frac{\partial}{\partial x} \end{bmatrix} \quad (2.24)$$

and the stress and strain components are assembled in the following vectors

$$\boldsymbol{\sigma}^T = [\sigma_{xx} \quad \sigma_{yy} \quad \sigma_{zz} \quad \sigma_{xy} \quad \sigma_{yz} \quad \sigma_{zx}], \quad (2.25)$$

$$\boldsymbol{\varepsilon}^T = [\varepsilon_{xx} \quad \varepsilon_{yy} \quad \varepsilon_{zz} \quad 2\varepsilon_{xy} \quad 2\varepsilon_{yz} \quad 2\varepsilon_{zx}], \quad (2.26)$$

with boundary conditions

$$\mathbf{N}^T \boldsymbol{\sigma} = \hat{\mathbf{t}} \quad \text{on } \partial\Omega_t, \quad (2.27)$$

$$\mathbf{u} = \hat{\mathbf{u}} \quad \text{on } \partial\Omega_u, \quad (2.28)$$

where

$$\mathbf{N}^T = \begin{bmatrix} n_x & 0 & 0 & n_y & 0 & n_z \\ 0 & n_y & 0 & n_x & n_z & 0 \\ 0 & 0 & n_z & 0 & n_y & n_x \end{bmatrix}. \quad (2.29)$$

Considering the gradient-enhanced damage formulation presented in Section 2.3.1, the diffusion problem (Eq. (2.18)) is solved, with the natural boundary condition (Eq. (2.21)), in addition to the previous equilibrium problem. The constitutive equations are similar to those presented in Section 2.2 replacing properly the local equivalent strain $\varepsilon_{eq}(\mathbf{x})$ with the nonlocal counterpart $\bar{\varepsilon}_{eq}(\mathbf{x})$. The complete set of equations is summarised in Table 2.1. This set represents a fully coupled problem, in the sense that the solution of the diffusion equation is not possible without the solution of the equilibrium equations and vice versa.

The numerical implementation of the gradient-enhanced damage model in the finite element framework requires spatial discretisation, by means of different shape functions for the displacement field \mathbf{u} and the non local equivalent strain $\bar{\varepsilon}_{eq}$ [70].

The model parameters for the complete problem of Table 2.1 can be assembled in the following vector

$$\mathbf{x}^T = [E \quad \nu \quad \kappa_i \quad \alpha \quad \beta \quad c \quad \eta], \quad (2.30)$$

where

- E = Young's modulus
 ν = Poisson's ratio
 κ_i = strain threshold for damage initiation
 α = softening curve parameter (related to the residual stress)
 β = softening curve parameter (related to the stiffness of softening branch)
 c = gradient parameter (related to the internal length scale l) = $l^2/2$
 η = ratio of compressive and tensile strength = f_{cc}/f_{ct}

The inverse problem reduces to the identification of vector \mathbf{x} .

Governing equations:	
$\mathbf{L}^T \boldsymbol{\sigma} + \mathbf{b} = \mathbf{0}$	equilibrium equations in Ω
$\bar{\varepsilon}_{eq} - c \nabla^2 \bar{\varepsilon}_{eq} = \varepsilon_{eq}$	diffusion equation in Ω
Boundary conditions:	
$\mathbf{N}^T \boldsymbol{\sigma} = \hat{\mathbf{t}}$	b. c. on $\partial\Omega_t$
$\mathbf{u} = \hat{\mathbf{u}}$	b. c. on $\partial\Omega_u$
$\mathbf{n}^T \nabla \bar{\varepsilon}_{eq} = 0$	natural b. c. on $\partial\Omega$
Kinematic equations:	
$\boldsymbol{\varepsilon} = \mathbf{L}\mathbf{u}$	kinematic equations in Ω
Constitutive equations:	
$\boldsymbol{\sigma} = (1 - \omega) \mathbf{D}^{el} \boldsymbol{\varepsilon}$	stress-strain relations
$\omega = \omega(\kappa) = 1 - \frac{\kappa_i}{\kappa} [1 - \alpha + \alpha e^{-\beta(\kappa - \kappa_i)}]$	damage evolution law
$\kappa(\bar{\varepsilon}_{eq}) = \max(\bar{\varepsilon}_{eq}, \kappa_{max})$	history variable definition
$\varepsilon_{eq} = \varepsilon_{eq}(\boldsymbol{\varepsilon})$	equivalent strain definition
$f(\bar{\varepsilon}_{eq}) = \bar{\varepsilon}_{eq} - \kappa(\bar{\varepsilon}_{eq})$	loading function
$f \dot{\kappa} = 0 \quad f \leq 0 \quad \dot{\kappa} \geq 0$	Kuhn-Tucker loading-unloading conditions

Table 2.1: Set of equations.

Chapter 3

The inverse problem

3.1 Introduction

Inverse problems can be characterized as problems where the answer is known, but not the question, or where the results, or consequences are known, but not the cause. Citing Oleg Mikailivitch Alifanov, great proponent of inverse methods, ‘the solution of an *inverse problem* entails determining unknown causes based on observation of their effects. This is in contrast to the corresponding *direct or forward problem*, whose solution involves finding effects based on a complete description of their causes’ [1]. In direct problems, in fact, analytical or numerical solutions are found for ordinary or partial differential equations with known initial conditions, boundary conditions and constants (or parameters) in the equations. On the contrary, in the inverse problem the solution is known (analytically, numerically or experimentally) and the objective is to determine the complete forward problem for which that solution is possible.

Inverse problems have applications in different engineering fields, such as navigation, oil drilling, water and air quality control, medical diagnostics (tomography), electrical imaging, acoustics, satellite positioning, atom investigation, economy modelling, non-destructive machines testing (e.g. crack identification), adaptive control, robotics, optimal design etc. However, the main contribution in the development of the inverse problem theory, in the sense of systematic exploration of the mathematical structure of the inverse problems and development of quantitative methods for extracting information data, has been given by geophysicists in the 1960s. They considered the necessity of studying the Earth’s interior using only data collected at the

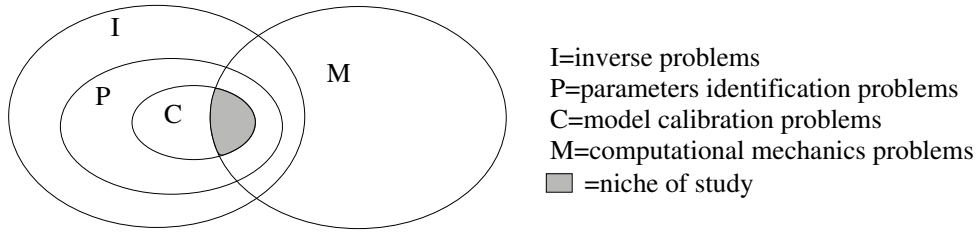


Figure 3.1: Inverse problem subsets and niche of interest for the present work.

Earth's surface. While the simultaneous evolution of computers has made the solution of inverse problems possible for a great array of applications.

There are many ways of classifying inverse problems and one is by the type of information that is sought in the solution procedure, so that we can distinguish:

backward or retrospective problems: the initial conditions are to be found

coefficient inverse problems or parameter identification problems: constant multipliers in the governing equations are to be found

boundary inverse problems: missing information at the boundary of the domain is to be found and this could also be a function estimation problem if the sought boundary condition changes with time.

Hence, parameter identification problems represent a subset of the Inverse Problems (see Figure 3.1) and within this class other subsets can be distinguished. In Continuum Mechanics, for instance, the constants to be identified could be inhomogeneous in the body, so that areas of degradation or variation of the mechanical properties of the material may be characterized. This is the case for *damage/crack/inclusion/defect identification* or *damage monitoring*, in which the identification involves localization of micro-defects or inclusions more than the estimation of constant (homogeneous) material parameters (e.g. [16, 21, 28]). Moreover, another subset of the parameter identification problems are the *inverse parameters design problems* characterized by the fact that the target solution is known exactly, by designer specifications, instead of being represented by experimentally measured data. Finally, the class of *model calibration problems* on which the present work is focused.

3.2 Inverse problems in Computational Mechanics

In the last years a considerable effort has been made in the development of numerical models that can reproduce the mechanical behaviour of materials. However, assuming that these models are capable of correctly describing the real phenomena that the material structure undergoes (at different scales) according to a qualitative point of view, their reliability significantly relies on the correct identification of the constants characterizing the phenomenological model equations. Although, these parameters may not all be directly measurable in the laboratory, more and more sophisticated experimental tools and techniques have been used in a large number of experiments carried out in the past years to measure other important quantities in order to gain insight into the physical mechanisms governing the material behaviour. Thus, the great difficulties in establishing a link between the experimental and the computational world arise from the fact that during laboratory tests a combination of structural and material behaviour responses is measured, while computational continuum models require the identification of the constitutive model parameters at a material point level. Within the Inverse Problems framework there are techniques available to close this gap, extracting information at material point level from the observed structural response. Hence, besides the continuous qualitative updating of models, the Inverse Problem Theory is concerned with the development of rules for quantitative updating of models [20, 82].

The Inverse Problem Theory offers also useful tools for continuous and simultaneous assessment and improvement of models and experiments. In this regard, it seems interesting to cite here the three research cases in science and engineering implied in inverse problems [13], in order to understand what is commonly done and what would be ideal to do. The cases are called A, B and C. In the first case, a simple model in algebraic form is adopted and the parameters are identified using simple equation inversions and measurements from experiments which are not necessarily simple. In the case B, a poorly-understood process is studied using complex models and complex experiments. However, they are kept scrupulously apart until a comparison of the result is made at the end by plotting them on the same figure. Adjustment of the model parameters may be done, for instance using inverse techniques, concluding that the ‘model is satisfactory’. The last case is the ideal situation in which complex models and experiments are used, but experiments and model interact continuously in a fully coupled analysis of the phenomenon, with the objective of improving both. In this case C the study of

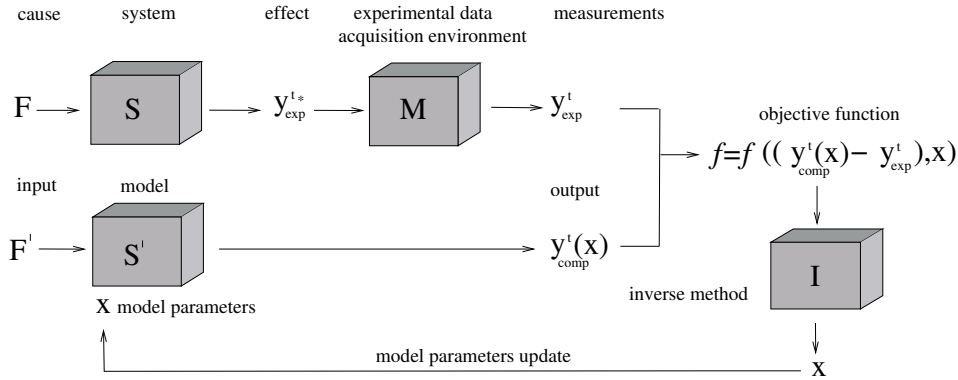


Figure 3.2: Schematic representation of a real and modelled system.

the design of the optimal experiment is extremely important, because many choices have to be made that can greatly affect the values and the accuracy of the model parameters estimate. These choices may, for instance, concern the number of sensors, their location, geometry and size of the specimen, boundary and loading conditions, duration of the experiment. Hence, the numerical model may be a useful tool for the optimal experiment design (several criteria and methods are available [30]). While, on the other hand, the experimental data may be used for qualitative and quantitative updating of the numerical model. This continuous integration and interaction of model building with experimental design, data acquisition and data analysis allows not only extraction of the maximum information out of the examined process, but also significant improvement of the model as basis for predictions and design problems.

3.3 Setting an inverse problem

Let S be the real mechanical system (see Figure 3.2) represented by a numerical model S' containing n_x model parameters assembled in the vector \mathbf{x} , e.g. Eq. (2.30). If a perturbation F is applied on S , the system reacts giving a certain response that, at different 'instants' t , may be represented by n_y *measurable* quantities collected in a \mathbf{y}_{exp}^{t*} vector. Through an 'in situ' or laboratory measurement equipment, the system response may be acquired, so that a vector \mathbf{y}_{exp}^t of *measured* quantities may be obtained. The variable t represents a time ordering variable and it can also be the amplitude of the

imposed external action on the system. If the n_y quantities are experimentally measured at different ‘instants’ t , the measurements acquisition system gives a flow of experimental data $\mathbf{y}_{\text{exp}}^t$ for $t = 1, 2, 3, \dots, n$. Different types of measurable quantities can be assembled in the $\mathbf{y}_{\text{exp}}^t$ vector. For structural mechanics problems these can be forces, the crack mouth opening displacements (CMOD), relative displacements measured by an interferometry technique, strains measured by strain gauges or embedded optical fibers, width of the localisation zone etc. On the other hand, the numerical model of the system, S' , given the model parameter vector \mathbf{x} , is able to compute at every ‘instant’ t , the solution of the forward problem, with numerical values for the n_y quantities that may be collected in a vector $\mathbf{y}_{\text{comp}}^t$. This vector is the corresponding computational counterpart of $\mathbf{y}_{\text{exp}}^t$ and it depends on the model parameters \mathbf{x} according to the following general relation

$$\mathbf{y}_{\text{comp}}^t = \mathbf{h}_t(\mathbf{x}), \quad (3.1)$$

where $\mathbf{h}_t(\mathbf{x})$ is referred to as the *forward operator* and it is non linear in the case of the gradient-enhanced continuum damage model used in this study.

Without solving any inverse problem the two vectors $\mathbf{y}_{\text{exp}}^t$ and $\mathbf{y}_{\text{comp}}^t$ are different. This can be due to different reasons that may be classified depending on whether they are intrinsic deficiencies of the ‘S’ or the ‘M’ box (see Figure 3.2). Numerical models, in fact, are an approximation of reality and they can not include all complex factors that may play a role in the real system. Particularly, regarding structural mechanics problems, weak points are:

modelling of loading and boundary conditions. For instance, constraints modelled as fixed points while in the real system small displacements are allowed, or the external load considered as a perfectly centered point load or a uniformly distributed load, while a small eccentricity may be present in the real tests.

material modelling. The choice of the constitutive framework, for instance a plasticity model, a damage model or a fracture model, is an a priori limiting factor. Subsequently, within each constitutive framework, a series of possible sources of error may be identified. Firstly, the model parameters are considered constant while, in the real system, they could be a function of time (due to e.g. corrosion, degradation etc.), microstructure, structure (in the sense of size, geometry and loading conditions), temperature, stress or strain state etc. Moreover, rela-

tively simple constitutive relations are used for the material behaviour, often neglecting large deformation plasticity, viscoplasticity etc. In addition, the material is generally assumed to be orthotropic or isotropic with the same behaviour in tension and compression. Finally, poor information at microstructural level is available or, even if images of the microstructure are obtained, poor knowledge exists on the modelling of the interaction and connection between the various microstructural elements and on their intrinsic properties. This results in a standard continuum modelling approach, for the description of accumulated and localised damage. Particularly, for the case of the gradient-enhanced continuum damage model, considered in the present thesis, the following limitations can be mentioned: the damage is isotropic, the fracture process is restricted to mode I, permanent deformations, viscous effects, load rate dependency and moisture effects are not included in the model. These limitations might represent possible sources of error, if one of the neglected aspects are instead present in the experimental tests.

deterministic versus stochastic modelling. Parameters with a stochastic nature are often neglected or assumed to be deterministic in the numerical model. Except from the meso- or microstructure, this may be due to manufacturing processes (concrete casting) or environmental conditions (humidity, temperature).

structure modelling. For instance, the three-dimensional reality, the environmental interactions (e.g. soil-structure) and the modelling of the complete experimental set up (e.g. loading plates) are often neglected.

dynamic versus static analysis. Small dynamic effects are neglected in static analyses and it is difficult to describe the damping properties of all parts of the structure.

On the other hand, also the passage of the $\mathbf{y}_{\text{exp}}^{t*}$ vector through the ‘M’ box (see Figure 3.2) does not occur without intrinsic deficiencies. The main differences between the two vectors $\mathbf{y}_{\text{exp}}^{t*}$ and $\mathbf{y}_{\text{exp}}^t$ are due to the so-called *measurement noise* (non systematic measurements errors). The following factors may be responsible for this discrepancy:

tolerance and reliability of the measurement devices. Bad accuracy of the measurement devices leads to systematic errors. These kind of er-

rors, however, may not only be intrinsically related to the measurement instruments, but also to an inaccurate or incorrect use of them.

debatable outline of the measurements statistics. i.e. bad quality of the statistics of the measurement data, characterized by a big scatter due to an insufficient number of repeated experiments. Moreover, the accuracy of the measurement data is often compromised by the averaging operation. For instance, the average load-deformation curve may be characterized by a peak load that is different from the average of the peaks, since the various curves, corresponding to repeated experiments, may be slightly shifted along the strain axis. In general, it is advisable to consider not only the average curves, but also the scatter bands in the numerical versus experimental comparison.

accidental errors. For instance in the placement of strain gauges or other displacement measurement devices.

experimental modelling. The experimental measurements are interpreted according to a certain simplified model of reality, built in the experimentalist mind, with some assumptions and inferences that may correspond to the computational model. Moreover, a good quality of the experiment should be guaranteed in order to avoid measurement of the external load that include uncontrolled reactions, loading system-specimen interactions or uncontrolled third dimension eccentricities.

Basically, all the above sources of errors may be synthesized in one unique aspect of reality that is never a closed system [66]. This implies a series of external uncontrolled and unpredictable factors that makes the demonstration of the truth, *verification*, of a numerical model impossible in the deepest and widest sense. A series of hypothesis and assumptions are necessary setting the model, that not always and not exactly may be verified in reality. Models are always approximations of the reality, being not always capable of capturing all aspects of the observed reality. On the other hand, experiments are always true, but their interpretation may contain errors.

However, a model that does not contain known or detectable flaws, is internally consistent and represents a reasonable logic description of the phenomenon can be *calibrated* or *validated*. This requires the comparison, at every ‘instant’ t , between the experimental data $\mathbf{y}_{\text{exp}}^t$ and the corresponding computed values assembled in $\mathbf{y}_{\text{comp}}^t(\mathbf{x})$, minimizing iteratively the error $\mathbf{e}(\mathbf{x})$ between the two vectors, until an acceptable solution is achieved. Hence, the

final estimate of the model parameter vector $\hat{\mathbf{x}}_t$ corresponds to the minimizer of an objective function that may be generally written as

$$f(\mathbf{x}) = (\mathbf{y}_{\text{exp}}^t - \mathbf{y}_{\text{comp}}^t(\mathbf{x}), \mathbf{x}_0) = (\mathbf{e}^t(\mathbf{x}), \mathbf{x}_0), \quad (3.2)$$

where also an initial starting point, *initial guess* of the model parameters, \mathbf{x}_0 may be included. The consequence of such a calibration process is that all discrepancies between the real system response and the output of the numerical model, due to the various mentioned reasons, are assumed to be covered only by adjustment of the model parameters. The result is that model parameters supposed to be constant are found to be variable according to, for instance, the structure geometry, size, time etc. Hence, variable model parameters may be the consequence of erroneous modelling. On the other hand, since the model parameters could be, on their own, dependent on all already mentioned different factors (e.g. time, strain state etc.), considering them as constant may be cause of erroneous modelling. This is, in the opinion of the author, the *loop of material modelling*: variable model (material) parameters are the cause and the effect of erroneous modelling.

Moreover, also the set up of the ‘I’ box can be a cause of possible sources of deficiencies. A crucial point, in fact, is the choice of experimental data that are to be included in the definition of the objective function of Eq. (3.2). Essentially, two types of problems may be encountered in this case depending on whether the considered experimental data set *under-determines* or *over-determines* the model parameters (or some of them) [82]. In the first case, the *intrinsic lack of data* can be responsible for the indetermination in two different ways. In one case, the used experimental data do not depend on the values of the model parameters to be identified. This is the trivial case. For instance, using force values along the tail of a softening force-deformation curve to identify elastic material properties, such as the Young’s modulus E and Poisson’s ratio ν is meaningless. In this regard, a *sensitivity analysis* is important in order to acquire knowledge on the effect that a certain parameter has on a given output variable. Moreover, the sensitivity analysis may be useful for the experiment design, for instance positioning displacement transducers in optimal information points of the specimen. This is referred to as *optimal experiment design* or *data acquisition planning* [30]. In the other case, the experimental data depend on the values of the model parameters to be identified, but do not guarantee uniqueness of the inverse solution. It is well known, for instance, that it is impossible to have a unique solution of the inverse problem of estimating the density distribution of a mass inside

a planet from gravitational field data on its surface, since infinitely many different mass density distributions correspond to the same external gravitational field (Gauss' theorem). Additional data or a priori assumptions are necessary. More specifically, in the case of the examined continuum damage model, it will be illustrated in Chapter 4 that correlation between two model parameters spoils the uniqueness of the solution if only the structural force-deformation curve of one single specimen size is involved in the inverse procedure. Also in this case, additional experimental data are requested.

On the contrary, regarding the second problem of over-determination of the model parameters, the *data redundancy* can, in general, easily be handled with methods that, still in the present days, do not differ essentially from those used, for instance, by Laplace [51] (who introduced the 'least-absolute-values' and the 'minimax' criterion to obtain the 'best' solution), Legendre [53] or Gauss [35] (who introduced the 'least-squares' criterion).

All the above mentioned weak points, related to the computational model, to the experiments and to the objective function definition may lead to the so-called *ill-posedness* of the inverse problem. This occurs when one or more of the following properties is not guaranteed for the solution of the inverse problem:

existence or identifiability: no model parameters set can reproduce the target response of the system. In fact, it is worthwhile to recall that the assigned target solution is an experimental response and not a computational solution. Hence, it is not known in advance if the adopted model can properly reproduce the system behaviour, so that the existence of the inverse solution is not a priori guaranteed. Then, the parameter identification problem may be used to assess if the adopted computational model can properly simulate the real system behaviour, highlighting its deficiencies, inadequacies and limitations.

uniqueness: different model parameter sets give equivalent computational responses of the system. This is typically the case of saddles or multiple absolute minima in the objective function, as schematically shown in Figure 3.3 for mono-dimensional problems.

stability: solutions that slightly differ may correspond to significantly different model parameter sets. Hence, small measurement errors cause significant errors in the identified parameters (see Figure 3.4).

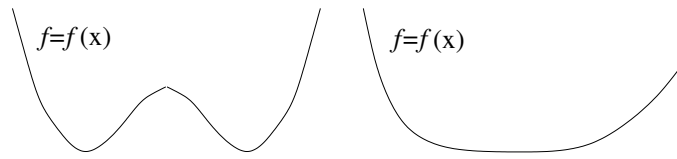


Figure 3.3: Examples of objective functions with non unique solutions for one-dimensional inverse problems.

In addition, once the objective function is defined, a proper inverse technique is required for the search of the ‘best’ model parameters estimate in the parameters space. In this case, the possible weak point is that a local search method is used starting from an inappropriate initial guess of the model parameters, in the case of *multi-extremality of the objective function* (see Figure 3.5). As a result, the inverse procedure may stick into local minima with a completely wrong estimate of the \mathbf{x} vector.

The conclusion is that calibrations of numerical models as tools for prediction and decision making problems, not only rely on a good choice of the ‘S’ box itself (see Figure 3.2), but also on a proper choice of the ‘M’ and ‘T’ boxes, and not only for one specific circumstance, but for a reasonable number of applications that tests the limits of the model.

Finally, it is worthwhile to notice that when the comparison between the result predicted by a model and the observed data is unfavorable, deficiencies in the model are searched for and an update of the model can be made until a good fit between the experimental data and the computational results is achieved. But when the match between computational and experimental data is reached, using different models (for instance continuum versus discrete fracture models or the case of all different size effect laws) then a dilemma may arise: it is the problem of equivalence between models or non-uniqueness of the theoretical description for a certain phenomenon. Then, there is no way to choose between them unless claiming extra considerations like simplicity, elegance, personal, political and philosophical preferences [66].

3.4 Inverse techniques

The first inverse technique dates back to the beginning of the nineteenth century. Gauss was the first who used, in his classic paper [35], the method of least squares (still adopted in parameter estimation) to determine the planets orbit. Since then, many different inverse techniques have been developed [12,

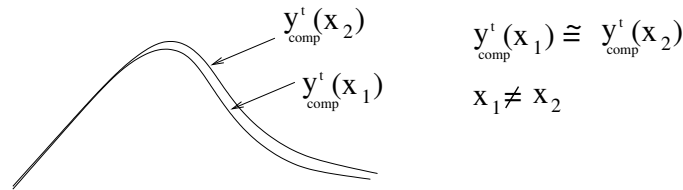


Figure 3.4: Example of unstable solution for one-dimensional inverse problems.

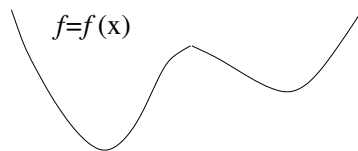


Figure 3.5: Example of objective functions with multiple minima for one-dimensional inverse problems.

69, 82], although only since the late 1950s the availability of both digital computational and data acquisition facilities have made parameter estimation practicable for a great array of applications.

A possible criterion of classification of the inverse methods is represented by the level of information on the objective functions (see Eq. (3.2)) required in the method for its minimization. Hence, zero order methods involve only calculations of the objective functions (e.g. direct search methods), first order methods need derivatives of the objective function (e.g. steepest descent method, trust region method) and second order methods require information on the Hessian (i.e on the curvature) of the objective function (e.g. (modified) Newton method, Marquardt method). Moreover, some methods are based on the idea of building an approximation of the objective function (construction of meta-models as models of models), for instance artificial neural networks (general approximators), radial basis functions, kriging and response surface methodology. Finally, there are methods that are characterized by being ‘local searchers’ and others by being ‘global searchers’ (e.g. genetic algorithms). In fact, as already mentioned in the previous Section, in case of multi-extremality of the objective function and an inaccurate initial guess of the model parameters, local search methods may not be able to find the global minimum, while, on the other hand, higher computational cost are generally related to global search methods. Hence, the choice of the inverse

technique is very important in order to identify the correct solution of the parameter estimation problem.

More general, the question should be addressed in terms of the *inverse strategy*, in the sense that more inverse techniques may be used, for instance in cascade, in order to optimize *effectiveness* (how close the estimation is to the exact solution), *efficiency* (time saving) and *robustness* (reliability or repeatability of the solution, for instance using different experimental data that are equivalent in terms of identifiability or starting from different initial guess of the model parameters) of the inverse method. The robustness of an inverse technique may be tested, for instance, by adding noise to the experimental data and checking that the identified parameters are not very sensitive to that noise.

For this purpose, two inverse techniques are used in the present work, with different features, so that a compromise of local-global search tool is obtained: the K-Nearest Neighbors (KNN) method (zero order method) and the Kalman filter (KF) method (first order method). While the KNN method belongs to the class of ‘discrete grid methods’, the KF technique solves the parameter identification problem in a statistical context, with a Bayesian approach, iteratively updating the parameters estimate starting from an initial guess. Since the final solution may be strongly influenced by the starting point of the search process, the KNN method is proposed for a first preliminary study of the parameters space. Hence, the so-identified parameters vector may be used as initial guess in the KF method in order to refine the inverse solution. Moreover, the KNN method provides a general overview of the parameters space, so that ill-posedness of the inverse problem, for instance in terms of non-uniqueness of the solution, may be easily captured, as will be shown in the numerical applications. This method is also suggested when a rough tuning of a model is required because it may be easily handled (derivative free method) and implemented for any computational model (without changing the forward problem code, but as an external tool) and also by users that are not familiar with the inverse problem theory. On the other hand, the KF method offers the advantage of a subsequent parameters update during the fracture process and the possibility of treating the data with their associated uncertainty.

3.4.1 KNN method

The experimental data which are generally available and which should be reproduced by the numerical model are force-deformation data. Hence, if

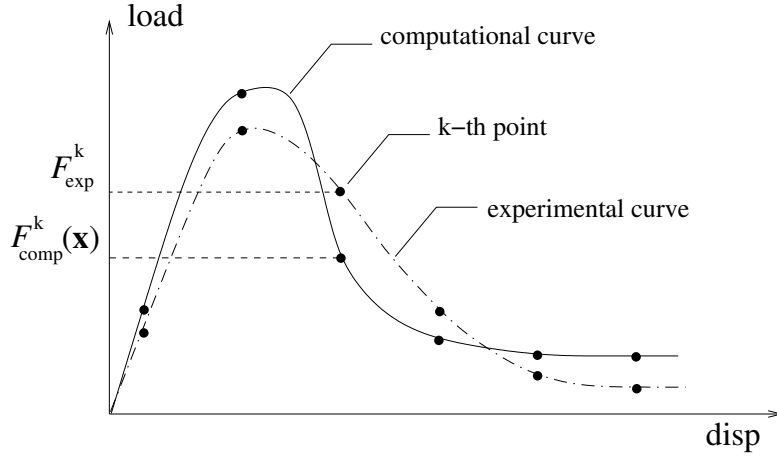


Figure 3.6: Fixed equally spaced intervals of deformations selected along the global force-deformation curves whose corresponding forces are collected in the vectors $\mathbf{y}_{\text{comp}}(\mathbf{x})$ and \mathbf{y}_{exp} for the KNN method.

fixed equally spaced intervals of deformations are selected, the corresponding forces may be considered as measured and computed quantities (see Figure 3.6), so that

$$\mathbf{y}_{\text{comp}}(\mathbf{x}) = [F_{\text{comp}}^1(\mathbf{x}) \quad F_{\text{comp}}^2(\mathbf{x}) \quad \cdots \quad F_{\text{comp}}^{n_y}(\mathbf{x})]^T, \quad (3.3)$$

$$\mathbf{y}_{\text{exp}} = [F_{\text{exp}}^1 \quad F_{\text{exp}}^2 \quad \cdots \quad F_{\text{exp}}^{n_y}]^T. \quad (3.4)$$

The vector \mathbf{y}_{exp} represents a point in the n_y -dimensional space, therefore a valid estimation of the initial guess \mathbf{x}_0 is the parameter set that corresponds to the nearest neighbour $\mathbf{y}_{\text{comp}}(\mathbf{x}_0)$ to \mathbf{y}_{exp} , between all the possible points $\mathbf{y}_{\text{comp}}(\mathbf{x}_i)$ (see Figure 3.7). In other words, the a priori guess of the model parameters corresponds to the minimum of the following function $f(\mathbf{x})$

$$f(\mathbf{x}) = (\mathbf{y}_{\text{exp}} - \mathbf{y}_{\text{comp}}(\mathbf{x}))^T \mathbf{C}_{\text{exp}}^{-1} (\mathbf{y}_{\text{exp}} - \mathbf{y}_{\text{comp}}(\mathbf{x})), \quad (3.5)$$

which represents the squared weighted distance between the two vectors \mathbf{y}_{exp} and $\mathbf{y}_{\text{comp}}(\mathbf{x})$. Hence, the initial guess \mathbf{x}_0 may be estimated using the K-Nearest Neighbours (KNN) method (K=1), that builds an approximation of the function $f(\mathbf{x})$ represented in Eq. (3.5). In fact, once a population of \mathbf{x}_i is chosen, the function $f(\mathbf{x}_i)$ can be evaluated at each point \mathbf{x}_i in a sort of

'discrete grid method' [74]. The parameter set \mathbf{x}_i that corresponds to the minimum value of $f(\mathbf{x}_i)$ can be considered as the initial guess \mathbf{x}_0 . Hence, no derivative of the function $f(\mathbf{x})$ is necessary, but only evaluations of the function at each point \mathbf{x}_i of an appropriate population of parameter sets, offering the advantage of performing parallel runs of different forward problems for the computation of $f(\mathbf{x}_i)$. \mathbf{C}_{exp} is the matrix of the error covariance of the measurements and may be computed using the standard deviation s of repeated experiments.

3.4.2 Kalman Filter method

In 1960, R. E. Kalman published his famous paper on recursive minimum variance estimation in dynamical systems [47]. This paper introduced a new algorithm, known as the Kalman filter, that represented a virtual revolution in the field of system engineering. Detailed treatments can be found in e.g. [15, 19, 20, 24, 39, 40, 45, 46, 57, 61, 79].

The Kalman filter methodology recursively solves parameter identification problems in a statistical context. In fact, the most general formulation of an inverse problem can be obtained using the framework of probability calculus and considering the uncertainties involved in the system. Hence, the right question should be addressed in the following way: given a certain amount of (a priori) information on some model parameters, and given an uncertain physical law relating some observable quantities to the model parameters, in which sense should we modify the a priori information, given the uncertain results of some experiments? However, the uncertainties related to the computational model (or physical law) are here neglected and the computational model is considered to be deterministic. The KF procedure considered herein is based on the following assumptions:

all the random variable vectors involved follow a Gaussian distribution (completely characterized by the mean value vector and a covariance matrix);

the computational model, i.e. the forward operator $\mathbf{h}_t(\mathbf{x})$, is considered as deterministic;

measurement uncertainties, represented by the vector \mathbf{v}_t , are considered as Gaussian white noises, i.e. as stochastic processes characterized by a Gaussian (or "normal") probability distribution with zero mean value and without correlation between different instants.

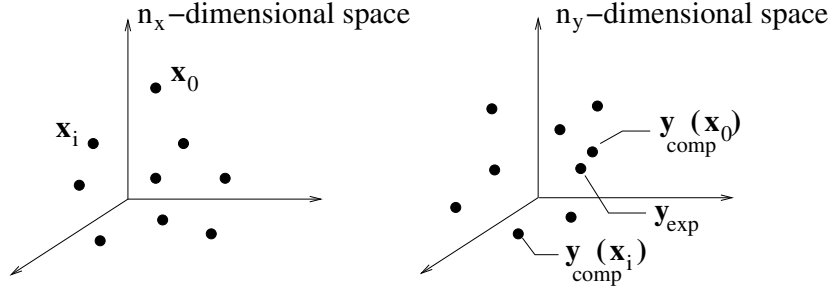


Figure 3.7: KNN method.

In other words, the measurements of the n_y quantities, collected in the $\mathbf{y}_{\text{exp}}^t$ vector, at every instant t , are characterized by an uncertainty vector \mathbf{v}_t for which we assume the following probability function $P(\mathbf{v}_t)$

$$P(\mathbf{v}_t) = ((2\pi)^{n_y} \det(\mathbf{C}_{\text{exp}}^t))^{-\frac{1}{2}} \exp \left\{ -\frac{1}{2} \mathbf{v}_t^T (\mathbf{C}_{\text{exp}}^t)^{-1} \mathbf{v}_t \right\}, \quad (3.6)$$

$$E(\mathbf{v}_t) = \mathbf{0} \quad E(\mathbf{v}_t \mathbf{v}_t^T) = \mathbf{C}_{\text{exp}}^t \quad E(\mathbf{v}_t \mathbf{v}_s^T) = \mathbf{0} \quad s \neq t, \quad (3.7)$$

where $E(\cdot)$ represents the averaging operator, $E((\cdot - E(\cdot))(\cdot - E(\cdot))^T)$ is the covariance operator and $\mathbf{C}_{\text{exp}}^t$ is the covariance matrix.

Since the forward operator has been assumed to be deterministic, the measurements noise \mathbf{v}_t determines the difference between experimental and computed observable quantities. Namely considering Eq. (3.1)

$$\mathbf{y}_{\text{exp}}^t = \mathbf{y}_{\text{comp}}^t + \mathbf{v}_t = \mathbf{h}_t(\mathbf{x}) + \mathbf{v}_t. \quad (3.8)$$

As previously outlined, next to the experimental ($\mathbf{y}_{\text{exp}}^t$) and computed ($\mathbf{y}_{\text{comp}}^t$) data, the KF procedure relies on a third independent information source, namely an initial ‘a priori’ estimate of the model parameter vector \mathbf{x} (i.e. for $t = 0$). This initial guess (Bayesian approach) can be chosen by the expert or can be based on engineering experience of the material under consideration.

Also the a priori information on the n_x parameters is assumed to be statistically characterized by a Gaussian distribution with \mathbf{x}_0 mean and $\mathbf{C}_0 = E((\mathbf{x} - \mathbf{x}_0)(\mathbf{x} - \mathbf{x}_0)^T)$ covariance matrix by means of probability function $P_{\mathbf{X}}$

$$P_{\mathbf{x}}(\mathbf{x}) = ((2\pi)^{n_x} \det(\mathbf{C}_0))^{-\frac{1}{2}} \exp \left\{ -\frac{1}{2} (\mathbf{x} - \mathbf{x}_0)^T \mathbf{C}_0^{-1} (\mathbf{x} - \mathbf{x}_0) \right\}. \quad (3.9)$$

A Gaussian probability distribution is assumed, as simplifying idealization, for the estimates computed up to time t . Substitution of the measurement noise \mathbf{v}_t into Eq. (3.6), as the difference between the experimental vector and the forward operator according to Eq. (3.8), gives the following conditional probability density of experimental data with respect to the parameters

$$P_{\mathbf{y}|\mathbf{x}}(\mathbf{x}, \mathbf{y}_{\text{exp}}^t) = ((2\pi)^{n_y} \det(\mathbf{C}_{\text{exp}}^t))^{-\frac{1}{2}} \exp \left\{ -\frac{1}{2} (\mathbf{y}_{\text{exp}}^t - \mathbf{h}_t(\mathbf{x}))^T (\mathbf{C}_{\text{exp}}^t)^{-1} (\mathbf{y}_{\text{exp}}^t - \mathbf{h}_t(\mathbf{x})) \right\}. \quad (3.10)$$

The two independent information sources of experimental data and a priori guess of model parameters in Eqs. (3.9) and (3.10) can be combined obtaining the a posteriori information as the following conditional probability density function (Bayes' theorem) ([82])

$$P_{\mathbf{x}|\mathbf{y}}(\mathbf{x}, \mathbf{y}_{\text{exp}}^t) = \frac{P_{\mathbf{y}|\mathbf{x}}(\mathbf{x}, \mathbf{y}_{\text{exp}}^t) P_{\mathbf{x}}(\mathbf{x})}{\mu}, \quad (3.11)$$

where $\mu \equiv P_{\mathbf{y}}(\mathbf{y}_{\text{exp}}^t)$ does not depend on the model parameter vector \mathbf{x} , and acts as a normalizing factor. Substitution of Eq. (3.10) and Eq. (3.9) into Eq. (3.11) results in the following relation

$$P_{\mathbf{x}|\mathbf{y}}(\mathbf{x}, \mathbf{y}_{\text{exp}}^t) = \frac{1}{\mu^*} \exp \{-S_t(\mathbf{x})\}, \quad (3.12)$$

in which

$$2S_t(\mathbf{x}) = (\mathbf{y}_{\text{exp}}^t - \mathbf{h}_t(\mathbf{x}))^T (\mathbf{C}_{\text{exp}}^t)^{-1} (\mathbf{y}_{\text{exp}}^t - \mathbf{h}_t(\mathbf{x})) + (\mathbf{x} - \mathbf{x}_0)^T \mathbf{C}_0^{-1} (\mathbf{x} - \mathbf{x}_0), \quad (3.13)$$

$$\frac{1}{\mu^*} = \frac{((2\pi)^{n_x} \det(\mathbf{C}_0))^{-\frac{1}{2}} ((2\pi)^{n_y} \det(\mathbf{C}_{\text{exp}}^t))^{-\frac{1}{2}}}{\mu}. \quad (3.14)$$

The unknown parameter vector \mathbf{x} corresponds to the maximum conditional probability density. In other words, the solution of the identification problem is the vector \mathbf{x} which follows from the optimization problem

$$\max_{\mathbf{x}} \left\{ P_{\mathbf{x}|\mathbf{y}}(\mathbf{x}, \mathbf{y}_{\text{exp}}^t) \right\}, \quad (3.15)$$

which equals

$$\min_{\mathbf{x}} \{ S_t(\mathbf{x}) \}. \quad (3.16)$$

The minimization of the function $S_t(\mathbf{x})$ consists of two parts (see Eq. (3.13)): (i) the first represents the difference between the experimental and computed n_y quantities at a certain instant t (or load level t) (ii) the second contains the a priori guess of the model parameters and improves the convergence of the minimization procedure.

If the forward operator $\mathbf{h}_t(\mathbf{x})$ is linear, the a posteriori conditional probability density $P_{\mathbf{x}|\mathbf{y}}(\mathbf{x}, \mathbf{y}_{\text{exp}}^t)$, given by Eq. (3.12), is a Gaussian (normal) distribution. However, this is not the case for the gradient-enhanced damage model, which is considered here, in which the dependence between the computed vector $\mathbf{y}_{\text{comp}}^t$ and the model parameters \mathbf{x} is nonlinear. In this case an iterative inverse procedure can still be formulated, introducing a step-by-step linearization of the forward operator and assuming a normal distribution of $P_{\mathbf{x}|\mathbf{y}}(\mathbf{x}, \mathbf{y}_{\text{exp}}^t)$ within each step. In this case no proof exists about the convergence properties of the procedure, however computational experience showed good convergence and stability properties of the method (see e.g [80]). For the linearization of the forward operator, the 1st-order Taylor expansion can be used around the initial guess of the model parameters \mathbf{x}_0 :

$$\mathbf{h}_t(\mathbf{x}) \simeq \mathbf{h}_t(\mathbf{x}_0) + \mathbf{S}_0(\mathbf{x} - \mathbf{x}_0), \quad (3.17)$$

in which:

$$\mathbf{S}_0 \equiv \frac{\partial \mathbf{h}_t}{\partial \mathbf{x}}(\mathbf{x}_0, t). \quad (3.18)$$

The tangent operator \mathbf{S}_0 is denoted as the *sensitivity matrix* and it quantifies the influence of the model parameters on the computed quantities $\mathbf{y}_{\text{comp}}^t$. When no closed form expression for \mathbf{S}_0 can be given, which is the usual case, the numerical computation of the sensitivity matrix represents a significant

part of the computing effort. In this case interpolations in the space of the parameters are necessary to numerically evaluate the derivatives of the forward operator, e.g. using the following three point formula

$$\frac{\partial h_{i,t}}{\partial x_j}((x_{1,t-1}), \dots, (x_{n,t-1}), t) \simeq \{h_i((x_{1,t-1}), \dots, (x_{j,t-1} + \Delta x_j), \dots, (x_{n,t-1}), t) - h_i((x_{1,t-1}), \dots, (x_{j,t-1} - \Delta x_j), \dots, (x_{n,t-1}), t)\} / 2\Delta x_j. \quad (3.19)$$

Consequently, for each time step t of the KF procedure, several forward analyses are carried out, in order to evaluate the forward operator \mathbf{h}_t at the points $(\mathbf{x}_0 + \Delta \mathbf{x})$ and $(\mathbf{x}_0 - \Delta \mathbf{x})$. If the number of parameters to identify is large, the computing time increases significantly because of this numerical determination of \mathbf{S}_0 . Alternatively, the derivatives of the sensitivity matrix might be determined, at each step t of the KF procedure, as part of the solution of the forward problem, at integration point level, by differentiation of the variables of the forward problem with respect to the model parameters (e.g. [41, 48]). This would save time for computing the sensitivity matrix, but it would require enhancement of the software code, reducing the simplicity and flexibility of the implemented inverse procedure regarding its applications to other computational models.

Substituting Eq. (3.17) into Eq. (3.13) and then into Eq. (3.12) and using matrix algebra rules results in the following equation

$$P_{\mathbf{x}|\mathbf{y}}(\mathbf{x}, \mathbf{y}_{\text{exp}}^t) = ((2\pi)^{n_x} \det(\hat{\mathbf{C}}))^{-\frac{1}{2}} \exp \left\{ -\frac{1}{2} (\mathbf{x} - \hat{\mathbf{x}})^T \hat{\mathbf{C}}^{-1} (\mathbf{x} - \hat{\mathbf{x}}) \right\}, \quad (3.20)$$

where

$$\begin{aligned} \hat{\mathbf{x}} &= \mathbf{x}_0 + [\mathbf{S}_0^T (\mathbf{C}_{\text{exp}}^t)^{-1} \mathbf{S}_0 + \mathbf{C}_0^{-1}]^{-1} \mathbf{S}_0^T (\mathbf{C}_{\text{exp}}^t)^{-1} (\mathbf{y}_{\text{exp}}^t - \mathbf{h}_t(\mathbf{x}_0)) \\ &= \mathbf{x}_0 + \mathbf{C}_0 \mathbf{S}_0^T [\mathbf{S}_0 \mathbf{C}_0 \mathbf{S}_0^T + \mathbf{C}_{\text{exp}}^t]^{-1} (\mathbf{y}_{\text{exp}}^t - \mathbf{h}_t(\mathbf{x}_0)), \end{aligned} \quad (3.21)$$

$$\begin{aligned} \hat{\mathbf{C}} &= E((\mathbf{x} - \hat{\mathbf{x}})(\mathbf{x} - \hat{\mathbf{x}})^T) = [\mathbf{S}_0^T (\mathbf{C}_{\text{exp}}^t)^{-1} \mathbf{S}_0 + \mathbf{C}_0^{-1}]^{-1} = \\ &= \mathbf{C}_0 - \mathbf{C}_0 \mathbf{S}_0^T [\mathbf{S}_0 \mathbf{C}_0 \mathbf{S}_0^T + \mathbf{C}_{\text{exp}}^t]^{-1} \mathbf{S}_0 \mathbf{C}_0. \end{aligned} \quad (3.22)$$

Vector $\hat{\mathbf{x}}$ is the mean value vector of the normal distribution $P_{\mathbf{x}|\mathbf{y}}$ given by Eq. (3.20), while $\hat{\mathbf{C}}$ is the corresponding covariance matrix. The values

assembled in $\hat{\mathbf{x}}$ are the estimates of the mean value of the model parameters and it is the solution of the optimization problem represented by Eq. (3.15). Eq. (3.21) and Eq. (3.22) can be rewritten in a more compact form

$$\hat{\mathbf{x}} = \mathbf{x}_0 + \mathbf{K}_0(\mathbf{y}_{\text{exp}}^t - \mathbf{h}_t(\mathbf{x}_0)), \quad (3.23)$$

$$\hat{\mathbf{C}} = \mathbf{C}_0 - \mathbf{K}_0 \mathbf{S}_0 \mathbf{C}_0, \quad (3.24)$$

where

$$\begin{aligned} \mathbf{K}_0 &= \mathbf{C}_0 \mathbf{S}_0^T [\mathbf{S}_0 \mathbf{C}_0 \mathbf{S}_0^T + \mathbf{C}_{\text{exp}}^t]^{-1} = \\ &= [\mathbf{S}_0^T (\mathbf{C}_{\text{exp}}^t)^{-1} \mathbf{S}_0 + \mathbf{C}_0^{-1}]^{-1} \mathbf{S}_0^T (\mathbf{C}_{\text{exp}}^t)^{-1}. \end{aligned} \quad (3.25)$$

If we assume

$$\begin{aligned} \hat{\mathbf{x}} &= \hat{\mathbf{x}}_t, & \hat{\mathbf{C}} &= \hat{\mathbf{C}}_t, \\ \mathbf{x}_0 &= \hat{\mathbf{x}}_{t-1}, & \mathbf{C}_0 &= \hat{\mathbf{C}}_{t-1}, \end{aligned} \quad (3.26)$$

Eqs. (3.21- 3.25) and Eq. (3.18) can be rewritten in the following format

$$\mathbf{S}_t = \frac{\partial \mathbf{h}_t}{\partial \mathbf{x}}(\hat{\mathbf{x}}_{t-1}, t), \quad (3.27)$$

$$\mathbf{K}_t = \hat{\mathbf{C}}_{t-1} \mathbf{S}_t^T [\mathbf{S}_t \hat{\mathbf{C}}_{t-1} \mathbf{S}_t^T + \mathbf{C}_{\text{exp}}^t]^{-1}, \quad (3.28)$$

$$\hat{\mathbf{x}}_t = \hat{\mathbf{x}}_{t-1} + \mathbf{K}_t (\mathbf{y}_{\text{exp}}^t - \mathbf{h}_t(\hat{\mathbf{x}}_{t-1})), \quad (3.29)$$

$$\hat{\mathbf{C}}_t = \hat{\mathbf{C}}_{t-1} - \mathbf{K}_t \mathbf{S}_t \hat{\mathbf{C}}_{t-1}. \quad (3.30)$$

Eqs. (3.27-3.30) define a procedure (schematically represented by the “KF” box in Figure 3.8) that, gives at each step t a better estimate of the mean value of the model parameters and the corresponding covariance matrix. The initialization of the iterative scheme (i.e. for $t = 1$) requires the

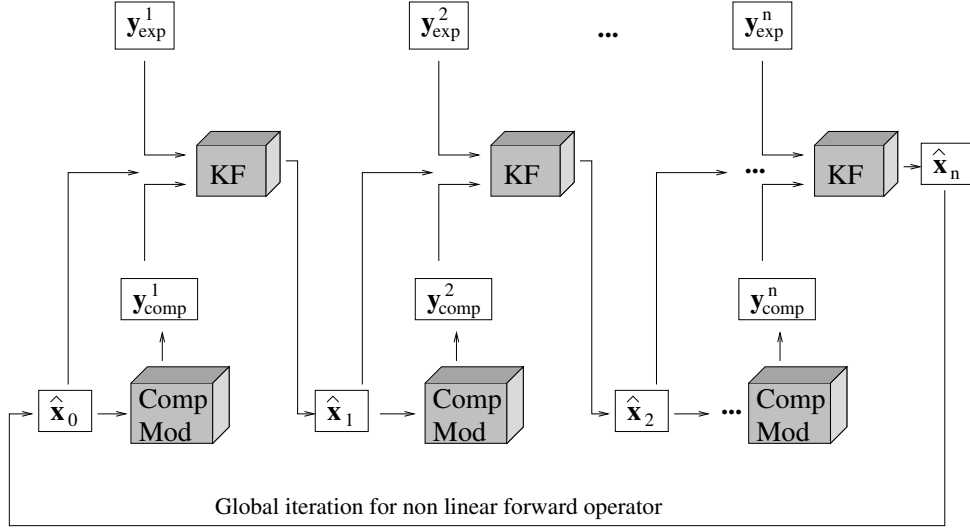


Figure 3.8: Parameter identification procedure.

initial guess $\hat{\mathbf{x}}_0$ and $\hat{\mathbf{C}}_0$. The a priori information on the model parameters is the input also for the computational model (represented by the “Comp. Mod.” box in Figure 3.8) in order to calculate the $\mathbf{y}_{\text{comp}}^1$ vector as a solution of the forward analysis. The three information sources $\mathbf{y}_{\text{exp}}^1$, $\mathbf{y}_{\text{comp}}^1$ and $\hat{\mathbf{x}}_0$ are processed by the Kalman filter scheme and, as a result, a new improved estimation $\hat{\mathbf{x}}_1$ is obtained and the next step (i.e. $t = 2$) can be analyzed.

The \mathbf{K}_t matrix is denoted as the *gain matrix* and, according to Eq. (3.29), it transforms the difference between the computed $\mathbf{y}_{\text{comp}}^t$ (or $\mathbf{h}_t(\hat{\mathbf{x}}_{t-1})$) and experimental $\mathbf{y}_{\text{exp}}^t$ vectors, at each step t , into a correction for the new estimate of the parameters $\hat{\mathbf{x}}_t$.

The Kalman filter process applied to the flow of experimental data $\mathbf{y}_{\text{exp}}^t$ with uncertainty $\mathbf{C}_{\text{exp}}^t$, starting from the a priori information $\hat{\mathbf{x}}_0$ with its uncertainty $\hat{\mathbf{C}}_0$, can symbolically be represented by

$$[\hat{\mathbf{x}}, \hat{\mathbf{C}}] = \mathcal{F}(\hat{\mathbf{x}}_0, \hat{\mathbf{C}}_0; \mathbf{y}_{\text{exp}}^t, \mathbf{C}_{\text{exp}}^t, t = 1, 2 \dots n). \quad (3.31)$$

If the forward operator $\mathbf{h}_t(\mathbf{x})$ is linear, it can be proven ([24], [47]) that the final estimates of the model parameters $[\hat{\mathbf{x}}, \hat{\mathbf{C}}]$ do not depend on the initial guess $[\hat{\mathbf{x}}_0, \hat{\mathbf{C}}_0]$. If, on the contrary, as in the present case of the gradient-enhanced damage model, the forward operator is nonlinear (even if not rigorously proven) this independence can be valid for the asymptotic result $[\bar{\mathbf{x}}, \bar{\mathbf{C}}]$

of an iterative application of the KF procedure on the same experimental data at the same KF steps

$$[\bar{\mathbf{x}}, \bar{\mathbf{C}}] = \mathcal{F}^{N \rightarrow \infty}(\hat{\mathbf{x}}_{N-1}, \hat{\mathbf{C}}_{N-1}; \mathbf{y}_{\text{exp}}^t, \mathbf{C}_{\text{exp}}^t, t = 1, 2 \dots n). \quad (3.32)$$

In this latter case, as schematically represented in the Figure 3.8, the final estimates $[\hat{\mathbf{x}}, \hat{\mathbf{C}}]$ of one KF procedure are used as initial guess for the subsequent KF process. For a finite number N of global iterations of the KF process, the resulting estimate of the model parameters may depend on the initial guess since multiple local minima and corresponding attraction basins may exist. The KF procedure, in fact, implicitly minimizes a norm of the difference between the experimental and computed data which is a non-convex function of the parameter vector \mathbf{x} , and therefore local minima may exist. The initial guess should be selected such that a point within the right attraction basin, and also as close as possible to the absolute minimum, is chosen, in order to speed up the convergence of the method, as will be analyzed in the numerical application.

3.2.2.1 Confidence indicators

Two indicators can be important in order to review the KF process carried out for a given experimental test. They are briefly presented in what follows, while the entire treatment of the subject can be found in [82].

The uncertainty domain

At each step t of the KF procedure, it is possible to associate with each model parameter estimation $\hat{\mathbf{x}}_t$ an ellipsoid which contains information on the correct values of \mathbf{x} . This ellipsoid is centered in point $\hat{\mathbf{x}}_t$ and is defined, in the space of the parameters, by the quadratic form associated to the inverse of its covariance matrix, namely:

$$(\mathbf{x} - \hat{\mathbf{x}}_t)^T \hat{\mathbf{C}}_t^{-1} (\mathbf{x} - \hat{\mathbf{x}}_t) = 1. \quad (3.33)$$

For the ellipsoid of Eq. (3.33) the following geometric properties can be proven [82]:

the square lengths of the principal diameters of the ellipsoid are equal to the eigenvalues of the current covariance matrix $\hat{\mathbf{C}}_t$;

the volume of the ellipsoid is proportional, through factor π , to the product of the lengths of the principal axes, i.e. to the $\det(\hat{\mathbf{C}}_t)$.

As a consequence, the ellipsoid obtained homotetically amplifying by a factor 3 that of Eq. (3.33) contains the correct values of the model parameters with a probability of 99%. If the KF identification process converges, the volume of the ellipsoid decreases at each step t , since the covariance matrix $\hat{\mathbf{C}}_t$ decreases, while its center moves towards the final correct estimation of the model parameters.

The relative information index

For sake of completeness also the relative information index is reported here (not used in the numerical applications). This index points out the test ranges that are the most productive information for the parameter identification procedure. In fact, it measures the informative content of the probability density P^t with respect to the probability density at the previous instant $t - 1$:

$$RI(P^t, P^{t-1}) = \int_{R^{n_x}} P^t(\mathbf{x}) \log \frac{P^t(\mathbf{x})}{P^{t-1}(\mathbf{x})} d\mathbf{x}. \quad (3.34)$$

If P^t is a Gaussian probability density, the expression 3.34 can be rewritten in a closed form:

$$RI(P^t, P^{t-1}) = (\hat{\mathbf{x}}_t - \hat{\mathbf{x}}_{t-1})^T \hat{\mathbf{C}}_{t-1}^{-1} (\hat{\mathbf{x}}_t - \hat{\mathbf{x}}_{t-1}) + \log \frac{\det(\hat{\mathbf{C}}_t)}{\det(\hat{\mathbf{C}}_{t-1})} + Trace[\hat{\mathbf{C}}_{t-1} \hat{\mathbf{C}}_t^{-1} - \mathbf{I}]. \quad (3.35)$$

The evaluation of the relative information index can be useful in order to determine the measurements intervals in the experimental test.

Chapter 4

Experimental data

The identification problem of model parameters needs experimental results as target solutions. The four experimental data series, used for this purpose in the present work, are briefly described in this Chapter.

4.1 Series n. 1

The uniaxial tensile test is considered to be the most objective test for determining tensile parameters that are needed as input in modeling of fracture in quasi brittle materials. Hence, cable-loaded uniaxial tensile tests performed on single-edge notched sandstone specimens in the Microlab of Delft University of Technology [86] are considered as a first series of experimental data.

The specimen geometry and boundary conditions are shown in Figure 4.1. Freely rotating boundary conditions provide a well-defined loading condition for the specimen and, in this problem with a single notch, they result in the initiation and propagation of a single crack in the notched area. However, it is difficult to make perfect hinges and often some small constraints are unintentionally imposed in one or more directions. These constraints are fundamentally unknown and it makes it difficult to reproduce experimental results by means of computational analyses. In order to reduce the effects of these constraints, cable supports are used for the uniaxial tensile tests. Moreover, using the cable supports the loading point is uniquely defined during the test, while in fixed platen tests stress-redistributions cause the specimen loading to change continuously. The experimental load-CMOD (crack mouth opening displacement) curves are obtained by means of a control system based on the maximum deformation rate of the control LVDTs, which is im-

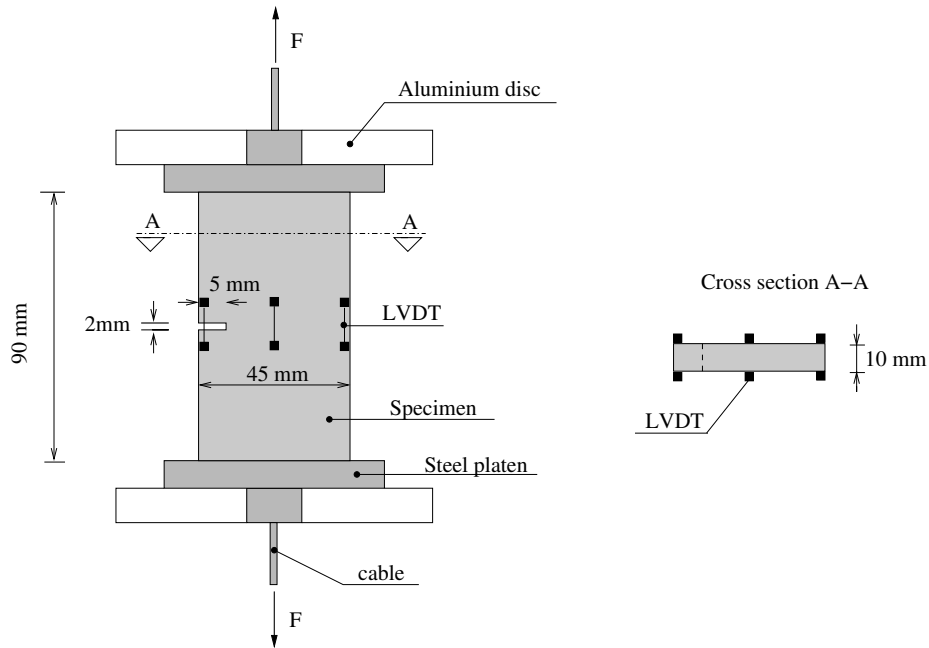


Figure 4.1: Specimen geometry and dimensions of experimental series n. 1.

portant for obtaining stable test results. The load-CMOD curves used in the numerical applications are related to the average CMOD measured by the two LVDTs placed close to the notch (see Figure 4.1).

4.2 Series n. 2

In order to investigate the predictive capabilities of the adopted constitutive model related to the size effect phenomenon, tensile size effect tests on concrete dog-bone shaped specimens carried out in the Stevin laboratory of Delft University of Technology [87, 88] are adopted as series n. 2.

The specimen geometry and dimensions, for all six different sizes, are shown in Figure 4.2. The specimens tested during these experiments may be divided into two groups according to the curing conditions after demoulding: the 'DRY' series (specimens placed in the laboratory under the approximate conditions of 20 degrees Celsius and 60% of relative humidity) and the 'WET' series (specimens placed in the climate room with temperature kept constant at 20 degrees Celsius and a relative humidity of 95%). For the numerical

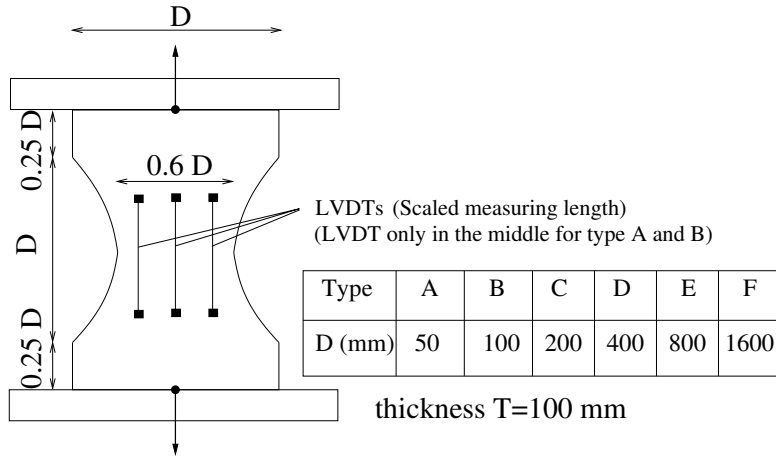


Figure 4.2: Specimen geometry and dimensions of experimental series n. 2.

applications presented in this thesis only the experimental results regarding the first group are used.

The available experimental data are the *global* load-displacement curves for the various specimen sizes. The displacement along the abscissas axis of these diagrams is represented by the average of the deformations measured by LVDTs with a measuring length that is scaled with the size of the specimen. Considering only the peak loads of the load-displacement curves of the various specimen size, a relation between the nominal strength and the characteristic specimen dimension may be found, which represents the size effect curve. For the experimental series n. 2 the width D of the basis of the specimen is considered as characteristic specimen dimension, while the nominal strength is computed from the maximum force F_{max} according to

$$\sigma = \frac{F_{max}}{0.6DT}, \quad (4.1)$$

in which T is the constant thickness of the specimen.

4.3 Series n. 3

Experimental results of three-point bending tests on notched concrete beams [32] (see Figure 4.3) have been used and are denoted as series n. 3.

In this case, in fact, in addition to the global force-deformation curve, deformations in some points in the neighborhood of the macrocrack are also

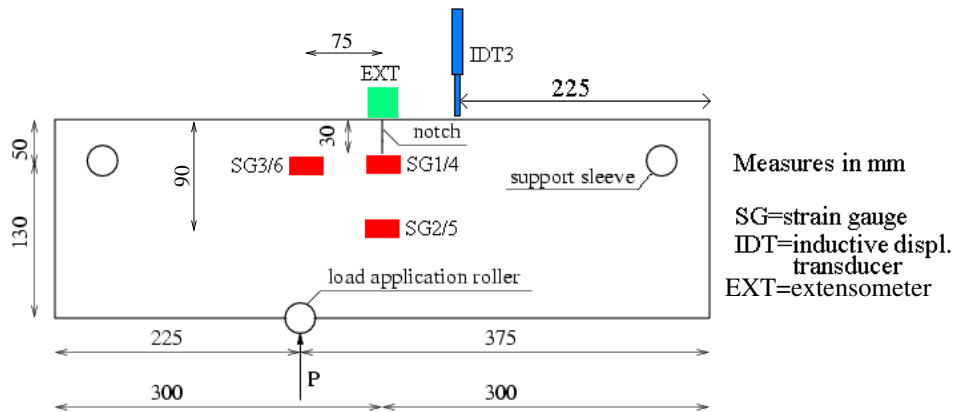


Figure 4.3: Specimen geometry and dimensions of experimental series n. 3.

registered by means of strain gauges (measuring length 10 mm) during the fracture process (see strain gauges positions in Figure 4.3).

4.4 Series n. 4

This series consists of double-edge notched uniaxial tensile tests and single-edge notched bending tests on specimens made of the same concrete [42, 43].

The specimen geometries and dimensions are shown in Figure 4.4 (not scaled saw-cut notches). In this case, besides conventional measurement techniques such as using LVDTs, in-plane Electronic Speckle Pattern Interferometry (ESPI) is used leading to whole field displacement and strain distribution along the main sensitivity direction perpendicular to the notches. Hence, the available experimental data consist of global data (force vs. deformation curves) and *local* data (width of the fracture process zone vs. deformation curves) for the different specimen sizes and geometries. For the double-edge notched uniaxial tensile tests the average of the CMODs measured at the two specimen sides is considered. Although, in the case of local data, the way of determining the size of the fracture process zone (FPZ) could be debatable and arbitrary (see Section 5.6), it is kept consistent for all the specimen sizes and loading conditions, so that this allows a relevant investigation of four essential aspects: i) which kind of experimental data is necessary for the identifiability of the model parameters and the well-posedness of the inverse problem (local/global data), ii) how are the estimated parameters influenced

by the experimental data involved in the inverse problem and iii) their dependency on structural effects and iv) the assessment of the reliability of the model predictions, in terms of loading conditions and size effects.

For representing the size effect curve of the bending specimens of the experimental series n. 4, the ligament height $W_{eff}=H-a_0$ is considered as characteristic specimen dimension and the nominal flexural strength is computed via

$$\sigma = \frac{3F_{max}S}{2W_{eff}^2T}, \quad (4.2)$$

in which T is the constant thickness of the specimen and S is the distance between the two loads.

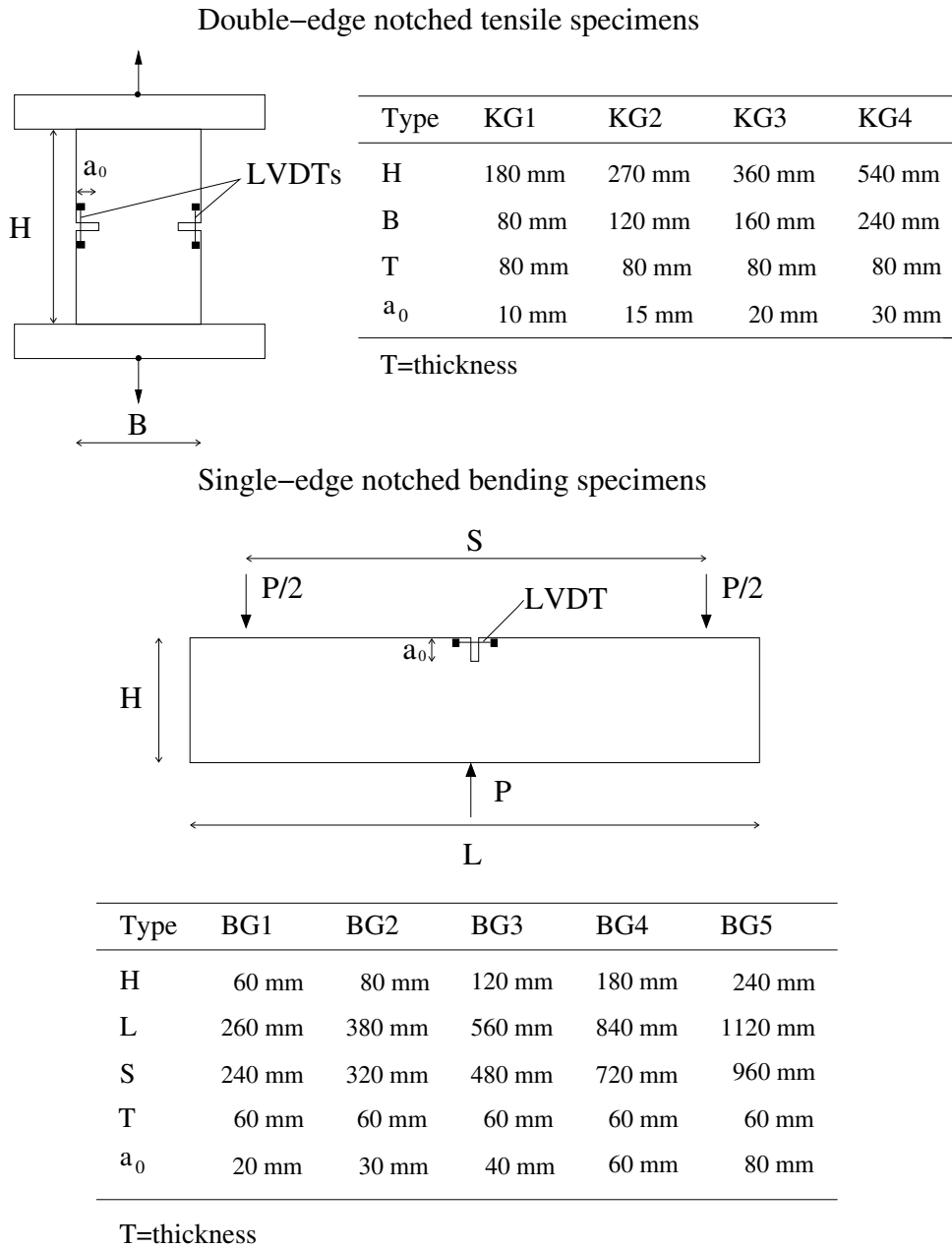


Figure 4.4: Specimens geometry and dimensions of experimental series n. 4.

Chapter 5

Numerical applications

In this Chapter the inverse methods presented in Chapter 3 are numerically applied for the solution of the identification problem of the gradient-enhanced continuum damage model (described in Chapter 2), using the experimental data reported in Chapter 4.

A preliminary sensitivity analysis, necessary to investigate the influence of the unknown model parameters on the force-deformation response of the specimen, is reported in Section 5.1. The inverse strategy implementation is briefly described in Section 5.2. Subsequently, applications of the inverse KF method are described in Section 5.3. The well-posedness of the inverse problem and factors of influence on the final parameter estimates are presented in Section 5.4. Finally, the issue of the choice of the set of experimental data to be used in the identification procedure and the predictive capabilities of the considered numerical model, in terms of size effects and loading condition effects, are discussed in the last two Sections.

5.1 Sensitivity analysis of model parameters

The term ‘sensitivity’ defines analyses that are performed in order to study the variation of the output (response) of the modelled system as effect of a variation of a single model parameter.

As already mentioned in Chapter 3, in general, the sensitivity analysis is important both for the choice of the experimental data, in order to avoid under-determined problems, and for the optimal experimental design. Although the used experimental series have been carried out earlier than the computations, the sensitivity analysis is performed in order to acquire knowl-

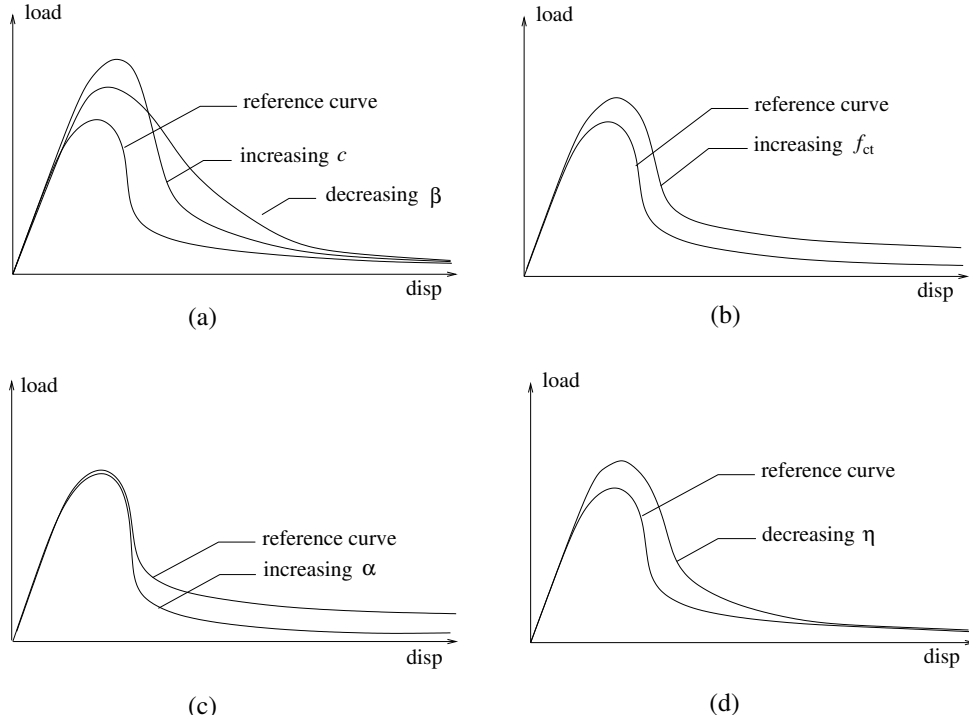


Figure 5.1: Influence of (a) the c and β parameters (b) the tensile strength parameter f_{ct} (c) the α parameter and (d) the η parameter on the global load-displacement curve.

edge on the effect that each model parameter has on the different parts of the global load-displacement curve (i.e. pre-peak, post-peak and tail), that means on the different phases of the fracture process. After that, a first rough fitting of the experimental curves through a trial and error method [82] can be easier performed.

In Figure 5.1 the influence of the various model parameters on the load-displacement curve is schematically reported in the case of three point bending tests. Increasing the gradient parameter c (or equivalently the length scale parameter l) induces the load-displacement curve to move towards higher load values (see Figure 5.1a), while the effect on the tail of the curve is smaller. Decreasing parameter β , not only corresponds to higher values of the load, but also to a more ductile behaviour in the post peak regime, while the effect on the tail of the load-displacement curve is smaller (see Figure

5.1a). In fact, shape changes in the post peak part of the curve are expected, since β mainly governs the slope of the softening branch of the constitutive law at material point level (see Figure 2.1b). The effects of an increment of the tensile strength f_{ct} are equally distributed through the entire curve (see Figure 5.1b), while only the tail of the curve is involved by changing the α parameter, as shown in Figure 5.1c. Finally, decreasing the η parameter the load-carrying capacity increases (see Figure 5.1d), except in the tail of the curve, so that an effect is obtained that is qualitatively similar to that caused by the gradient parameter c .

The described influences of the model parameters on the global response of the specimen are shown in Figure 5.2 in the case of the smallest size of the single-edge notched bending specimens of the experimental series n. 4 (note that the stress reported in the ordinates axis of the stress-CMOD curves for the three point bending tests are computed according to Eq. (4.2)).

Independently from the adopted inverse technique, the solution of a parameter identification problem may be very time consuming if the number of the unknown parameters is high and the numerical solution of the non-linear forward problem is complex. Hence, if possible, a reduction of the model parameters vector should be adopted, since it may significantly decrease the computing effort required in the inverse problem. In the present case, the described model contains seven parameters to be identified (see Eq. (2.30)). Two parameters are the elastic moduli (E and ν), which can be determined from standard uniaxial tests, and two parameters are related to the tensile and compressive strength of the material (f_{ct} and $\eta = f_{cc}/f_{ct}$). Although these parameters are subject of an extended debate on how they can be estimated, in the present study they are considered as a priori known. Moreover, as already shown through the sensitivity analysis, the α parameter mainly governs the tail of the softening curve (or the residual load carrying capacity when all damage has developed) and experimental evidence suggests values for it between 0.9 and 0.99. Hence, few corrections through the trial and error fitting method [82] can provide a reasonable good estimation for this parameter. As a consequence, the parameter identification problem presented in this thesis mainly focuses on the gradient parameter c (or equivalently on the length scale parameter l) and on the slope of the softening branch of the constitutive law β .

Regarding the tensile strength parameter f_{ct} , some additional comments can be made. As previously reported and shown in Figures 5.1 and 5.2, the peak load and the post peak branch of the load-deformation curve are mainly

STRESS–CMOD curves (BG1)

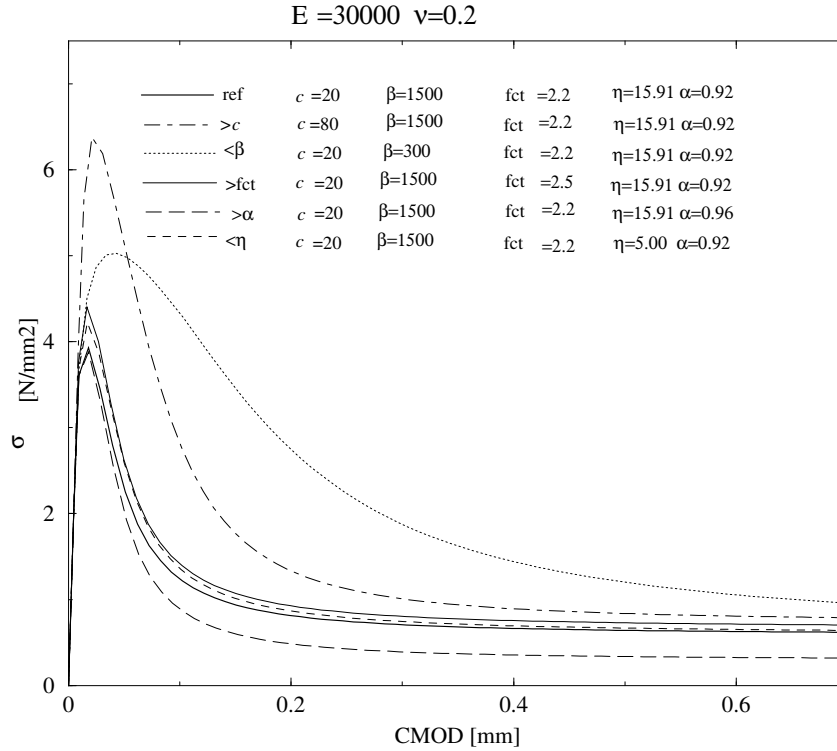


Figure 5.2: Influence of the various model parameters on the global load-displacement curve in the case of BG1 specimen of the experimental series n. 4 (see Figure 4.4) (the model parameters units are consistent with the stress and CMOD units. $E=30000$ MPa, $\nu=0.2$).

governed by three parameters: the tensile strength f_{ct} , the gradient parameter c and parameter β . The experimental value measured during tensile tests on cubic specimens may be taken as starting point for the tensile strength, although the parameter f_{ct} in the adopted computational model might have a different value. Successively, it is possible to carry out (more time consuming) inverse procedures for the identification of all three parameters, both with the KNN method and with the KF method. However, when applying the KNN method on a grid of the tensile strength parameter f_{ct} and the gradient parameter c , a correlation results between the two parameters, as it can be

also expected considering Figure 5.1a and b. Hence, additional experimental data might be necessary for the well-posedness of the inverse problem with simultaneously identification of tensile strength f_{ct} , gradient parameter c and parameter β , with respect to the case in which only the last two parameters are estimated.

5.2 Inverse strategy implementation

The KF procedure, as well as the KNN method, is implemented outside the finite element code FEAP. The finite element (FE) analyses are necessary to carry out the forward numerical analysis at each step t in the inverse procedure. Hence, the code related to the two inverse methods may be built as an external program, with the advantage that no modification of the FE code is needed and, as a consequence, the strategy is easy adaptable for different forward models.

The code related to the implementation of the KNN method is entirely separate from the FE code. The method may be coded in different programming environments and in the present work it has been done in a Matlab framework. The solution of the KNN method is used as initial parameters vector value in that part of the FE input file related to the material property description (see Figure 5.3).

The KF procedure is executed using two additional ‘loop’ commands in the input file of the FE analysis (see Figure 5.3), which are placed externally to the usual loops related to the iterative solving scheme of the non-linear forward analysis. One loop is necessary in order to numerically evaluate the sensitivity matrix according to the three points formula of Eq. (3.19) for each KF step. Hence, the forward analysis is stopped and repeated two additional times for each model parameter to be identified (with plus and minus a small variation of that parameter) for each KF step. The other loop is related to the number of KF steps, so that the forward analysis is stopped at the end of one KF step and repeated for the next KF step with the updated estimation of the model parameters. Between the two loops a user subroutine is called where the iterative KF procedure, represented by the Eqs. (3.27-3.30), is implemented. The subroutine provides the new parameters estimate, which have to be substituted into the previous value in the allocated memory, before the following KF step starts. Hence, two ‘loop’ commands and few user-subroutines, called between the usual three parts of the FE input file (see dashed boxes in Figure 5.3), may be used for the implementation of the

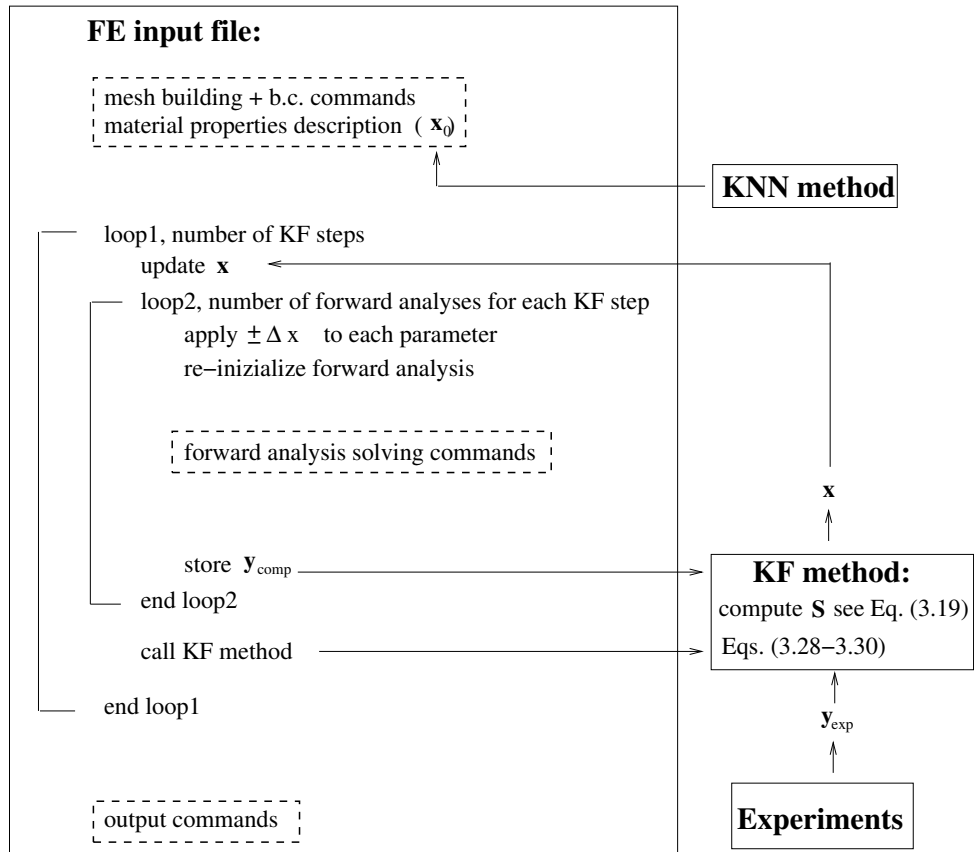


Figure 5.3: Inverse methods implementation scheme.

$F_{\text{exp}}[\text{N}]$	$C_{\text{exp}}^t[\text{N}^2]$	t	CMOD[mm]
50.107	0.70	1	0.007
46.526	0.60	2	0.037
29.715	0.25	3	0.067
20.694	0.12	4	0.097
14.021	0.05	5	0.127
10.580	0.03	6	0.157

Table 5.1: Experimental values for series n. 1.

adopted inverse method.

5.3 KF method applications

Applications of the KF method are presented using the data of the sandstone specimens of the experimental series n. 1 [86]. Analogous features, issues and results are encountered for the other experimental series.

The relative vertical displacement of the opposite faces of the notch, i.e. the ‘crack mouth opening displacement’ CMOD (see Figure 4.1) is a monotonically increasing quantity in time t . As observable quantity, the force F applied at the cables is considered at each time t

$$y_{\text{exp}}^t = [F_{\text{exp}}^t], \quad (5.1)$$

$$y_{\text{comp}}^t = h_t(\mathbf{x}) = [F_{\text{comp}}^t(\mathbf{x})]. \quad (5.2)$$

The measurement noises are taken proportional to the measured force F_{exp}^t considering measurement accuracies of $\pm 5\%$ [17]:

$$C_{\text{exp}}^t = \left(\frac{0.05}{3} F_{\text{exp}}^t\right)^2. \quad (5.3)$$

In Table 5.1 the experimental values for F and the relative covariance (computed according to Eq. (5.3)) for each KF step t are listed.

The values of the model parameters considered as a priori known for the experimental series n. 1 are listed in Table 5.2.

Conventional spatial discretisation by quadrilateral 4-node finite elements is used in the domain Ω with bilinear shape functions for the displacements

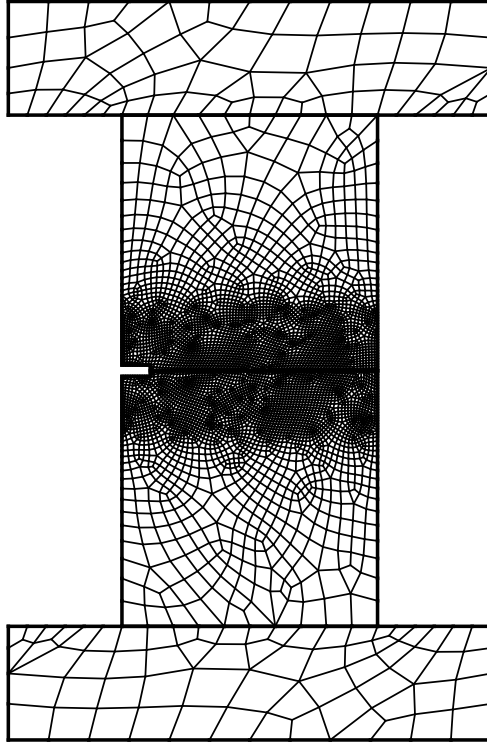


Figure 5.4: Mesh used for the forward analyses in KF procedure for the experimental series n. 1: 2763 quadrilateral 4-noded elements.

	E[MPa]	ν	f_{ct} [MPa]	α	η
specimen (sandstone)	7000	0.2	2.3	0.96	12.0
loading platen	210000	0.3	-	-	-
cables	195000	0.3	-	-	-

Table 5.2: Values of the a priori known model parameters for the experimental series n. 1 [86].

and linear shape functions for the non-local equivalent strains (see Figure 5.4). For reasons of vertical equilibrium all vertical displacements along the horizontal symmetry line at the notch are kept zero. The test is numerically simulated assuming a plane stress situation. The steel platens are also modelled contrary to the aluminium discs which are assumed to have a small in-

fluence on the global response. The loads are applied by means of an indirect displacement control procedure with the crack mouth opening displacement (CMOD) taken as control parameter. The displacement norm criterion with a tolerance of 10^{-6} is used as convergence criterion and a full Newton-Raphson scheme is used to solve the nonlinear system of equations.

5.3.1 Scalar KF procedure for c identification (KF_I and KF_{II})

The term ‘*scalar*’ is used for a KF procedure for the identification of only one model parameter. Since also one observable quantity is taken into account, the entire KF procedure involves, in this case, only scalar quantities.

The first KF process, marked as KF_I, concerns the identification of the gradient parameter c , i.e.

$$\hat{x} = [\hat{c}]. \quad (5.4)$$

The β parameter is considered in this case as a priori known and its value is set equal to 150. The following values are chosen for the initial guess of the gradient parameter and its covariance (the last corresponding to an uncertainty of about 25%):

$$\hat{x}_0 = [\hat{c}_0] = 0.8 \text{ mm}^2, \quad (5.5)$$

$$\hat{C}_0 = 0.005 \text{ mm}^4. \quad (5.6)$$

In order to limit the computing time, six steps are considered for the KF_I procedure (i.e. $t=1,2,3,4,5,6$). Three forward analysis for each KF step are necessary in order to numerically compute the derivatives of the forward operator $h_t(x)$, considering a fixed variation of $\Delta c = 0.05 \text{ mm}^2$.

The gradient parameter mean value estimates and the corresponding covariances during KF_I are illustrated in Figure 5.5 (square points). The c parameter estimate converges towards a constant value, while the covariance, related to the uncertainty on the parameter estimate, reduces progressively to zero.

In Figure 5.6 the global load-CMOD curves are plotted for all steps of KF_I (three curves per step). Since all forward analyses are carried out sequentially without any interruption, the straight lines towards the origin correspond to each analysis re-initialization. The experimental curve is fitted well by the numerical one if it is computed using the KF_I converged value of the gradient parameter.

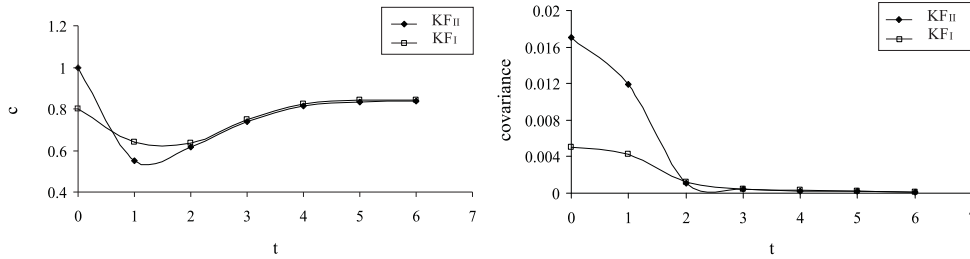


Figure 5.5: KFII and KFI estimations of the (a) c parameter and (b) covariance of c .

An analogous KF identification process, KFII, is carried out starting from a different value of the a priori guess. The gradient parameter initial estimate is taken equal to 1.0 mm^2 and the covariance equal to 0.017 mm^4 .

As shown in Figure 5.5, after the third step, the two KF processes result in similar estimations of the parameter, with similar fitting of the global load-CMOD curve (see Figure 5.7).

5.3.2 Scalar KF procedure for β identification (KFIII)

A ‘scalar’ KF procedure, referred to as KFIII, is also applied for the identification of the β parameter. The gradient parameter c is considered in this case as a priori known and set equal to 0.83 mm^2 (close to the previous KFs converged value). The β parameter initial estimate is taken equal to 100.0 and the covariance equal to 70.0, while a fixed variation $\Delta\beta = 10.0$ is applied to β at each of the three forward analyses.

The β parameter and covariance estimates during the KFIII procedure are plotted in Figure 5.8. The a priori guess of β is underestimated resulting in a higher load value around the peak of the global load-CMOD curve (see Figure 5.9). After the third KFIII step the final value of β is approximately found. The procedure converges towards a constant value that is very close to the a priori fixed one of the two previous KF procedures.

5.3.3 Bidimensional KF procedure for c and β identification (KFIV)

The term ‘*bidimensional*’ is used for a KF procedure in which the identification of two model parameters is done. A bidimensional KF procedure, referred

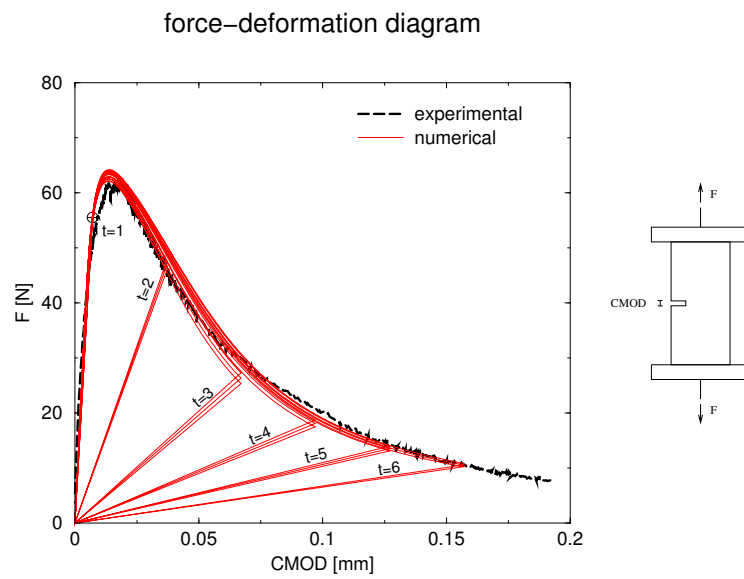


Figure 5.6: KFI fitting of the global Load-CMOD response of the experimental series n. 1 [86].

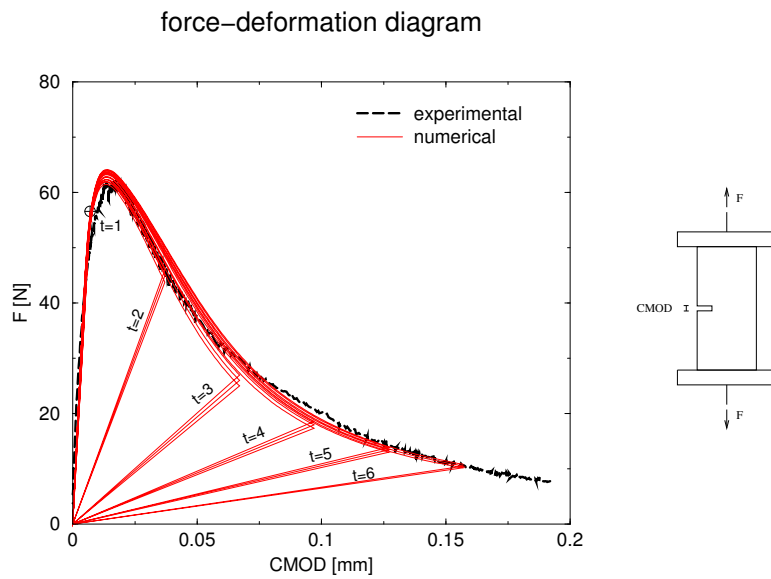


Figure 5.7: KFII fitting of the global Load-CMOD response of the experimental series n. 1 [86].

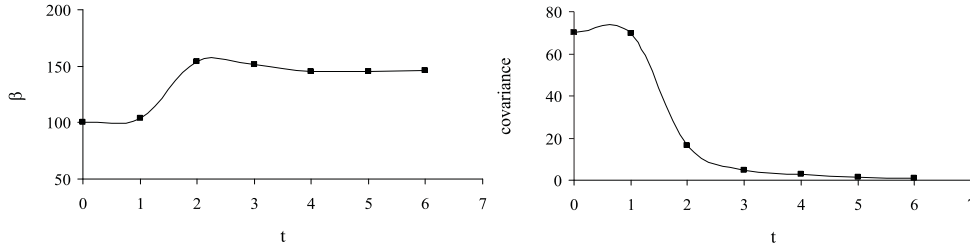


Figure 5.8: KFIII estimations of the (a) β parameter and (b) covariance of β .

to as KFIV, is carried out for the identification of the c and β parameters simultaneously. In this case the vector \mathbf{x} is defined as

$$\hat{\mathbf{x}}^T = [\hat{c} \quad \hat{\beta}]. \quad (5.7)$$

The initial guess values for \mathbf{x} and \mathbf{C} are

$$\hat{\mathbf{x}}_0^T = [1.0 \quad 200.0], \quad (5.8)$$

$$\hat{\mathbf{C}}_0 = \begin{bmatrix} 0.017 & 0.0 \\ 0.0 & 270.0 \end{bmatrix}. \quad (5.9)$$

Considering the following model parameter variation vector:

$$\Delta \mathbf{x}^T = [0.05 \quad 10.0], \quad (5.10)$$

in order to numerically evaluate the sensitivity matrix \mathbf{S} , five forward analyses have been carried out for each KFIV step.

The c and β mean value estimates and the corresponding covariances during the KFIV process are plotted in Figures 5.10 and 5.11. The simultaneous identification of the β parameter results in different c mean value estimates during KFIV in comparison with the ones obtained during KFII. It is worth noting that, for computing time reasons, a fixed number of KF steps has been considered. However, in the case of the KFIV procedure the convergence of the identification process towards a constant value for c is slower than in KFI or KFII. The final value for the covariance of c , in fact, is significantly larger in case of KFIV. Consequently a bigger uncertainty domain (see Section 3.2.2.1) is present for KFIV, as illustrated in Figure 5.12. A larger band of 99% confidence limits characterizes the mean value of the gradient parameter

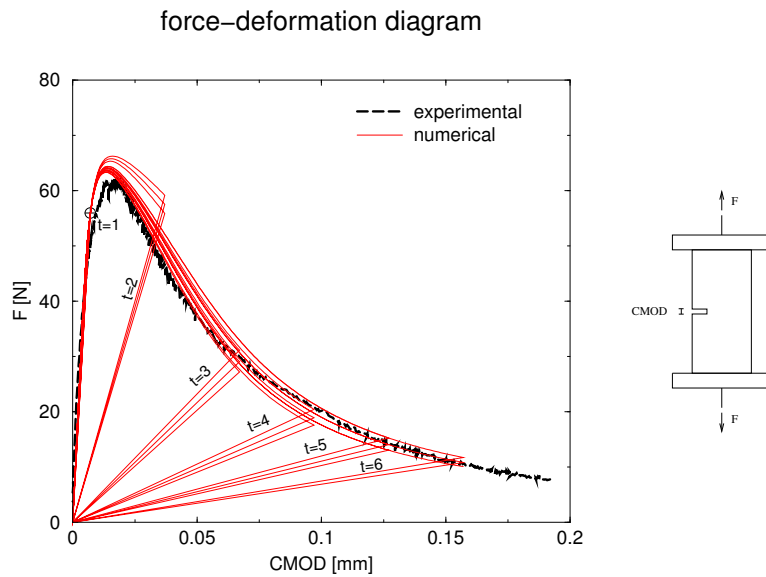


Figure 5.9: KFIII fitting of the global Load-CMOD response of the experimental series n. 1 [86].

c in case of KFIV, i.e. the area that contains the correct value of c with a probability of 99% is wider for the bidimensional KF procedure.

This suggests the necessity of increasing the number of steps in the bidimensional identification process or to perform an iterative application of the KF procedure with the same experimental data according to Eq. (3.32).

In Figure 5.13 the global numerical and experimental load-CMOD curves are plotted for the case of KFIV (note the five forward analyses per KF step).

5.4 Uniqueness and stability of the solution

The application of the KF procedure described in the previous Section shows that the method is a powerful tool, which not only identifies the required model parameters, but also provides a quantitative assessment of the uncertainties related to their estimates. Moreover, the experimental global response of the specimen, represented by the load-CMOD curve, is well fitted by the numerical curves corresponding to the model parameters identified by the KF procedure. However, other aspects arise when the choice of the initial guess of the model parameters is not so appropriate and a preliminary study

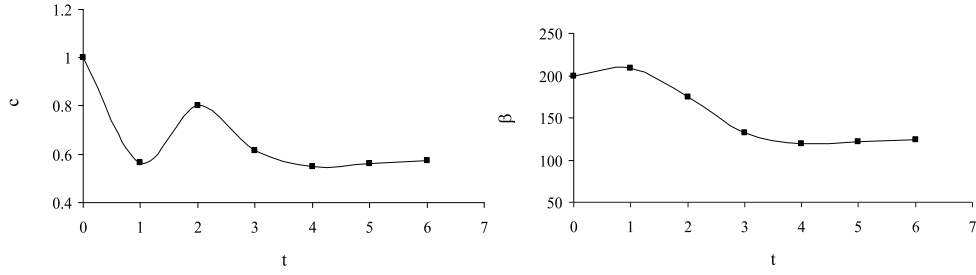


Figure 5.10: KFIV estimations of (a) the c parameter and (b) the β parameter.

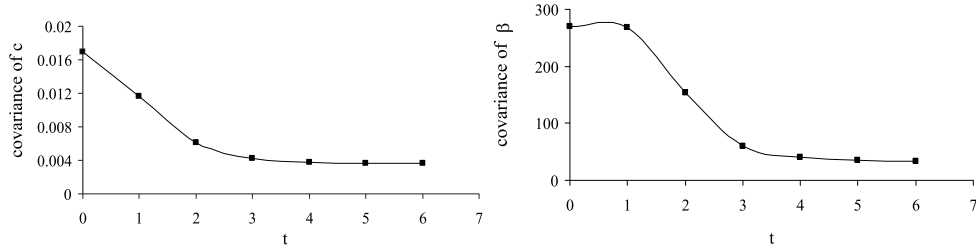


Figure 5.11: KFIV estimations of the covariance of (a) the c parameter and (b) the β parameter.

of the parameters space is performed, through the KNN method, for that purpose. The problem is examined considering first only the global response (force-deformation curve) of one single size.

5.4.1 Global curve of one single size

The data related to the concrete dog-bone shaped specimens of the experimental series n. 2 [87, 88] is used in this application. The values of the model parameters not involved in the identification procedure (valid for all specimen sizes of the series) are presented in Table 5.3.

	E[MPa]	ν	f_{ct}	η
specimen (concrete)	33000	0.2	3.3	14.55
loading platen	210000	0.3	-	-

Table 5.3: Values of the a priori known model parameters for the experimental series n. 2 [87, 88].

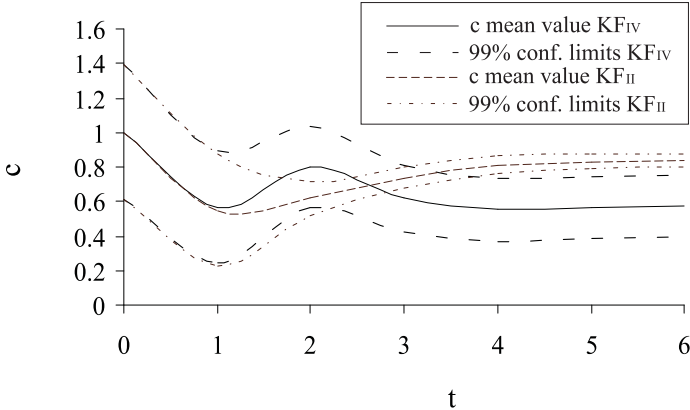


Figure 5.12: c mean values and corresponding 99% confidence limits for KFII and KFIV.

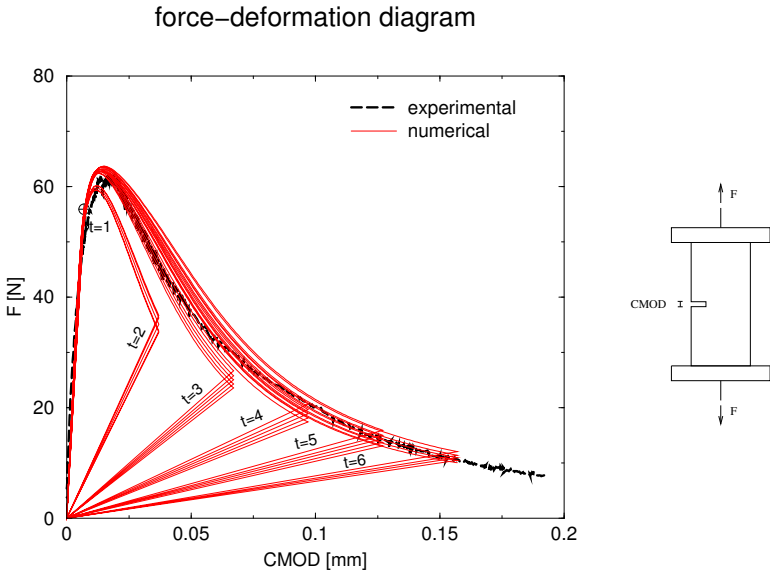


Figure 5.13: KFIV fitting of the global Load-CMOD response of the experimental series n. 1 [86].

Parameter	c [mm ²]	β	α
Value n. 1	20.0	1500.0	0.93
Value n. 2	25.0	1400.0	0.94
Value n. 3	30.0	1300.0	0.95
Value n. 4	35.0	1200.0	-
Value n. 5	40.0	1100.0	-
Value n. 6	45.0	1000.0	-
Value n. 7	50.0	900.0	-
Value n. 8	-	800.0	-
Value n. 9	-	700.0	-

Table 5.4: Parameter values for the generation of the parameter sets population for the experimental series n. 2.

The experimental quantities collected in the vector \mathbf{y}_{exp} are represented by 100 points along the global load-displacement curve of one single specimen size. In other words, 100 total forces are considered corresponding to 100 fixed and equally spaced deformations (see Figure 3.6). Hence, Eq. (3.5), considering Eqs. (3.3) and (3.4) and that the matrix \mathbf{C}_{exp} is assumed to be diagonal (uncorrelated data), may be rewritten as

$$f(\mathbf{x}) = \sum_{k=1}^{100} \frac{1}{C_{\text{exp}}^k} [F_{\text{comp}}^k(\mathbf{x}) - F_{\text{exp}}^k]^2. \quad (5.11)$$

The parameters population selected for the evaluation of \mathbf{y}_{comp} is represented by the sets generated by all combinations of the values given in Table 5.4.

For each specimen size a total number of $9 \times 7 \times 3 = 189$ forward problems have to be solved in order to compute the \mathbf{y}_{comp} vector corresponding to each parameters set \mathbf{x}_i . Hence, for each fixed value of $\alpha = \alpha_j$ (with $j = 1, 2, 3$), a population of couples $[\beta_i, c_i]$ (with $i = 1, 2, \dots, 63$) is selected. From the values of the function of Eq. (5.11) calculated in these points, the approximation of the surface $f_{\alpha=\alpha_j}(\beta, c)$ can be built and the minimum can be selected according to the KNN method. The plot of the approximated surface $f(\mathbf{x})$ is shown in Figure 5.14, for all specimen sizes (except type F, omitted because of the large computational effort). Figure 5.14 is related to $\alpha=0.93$, while analogous results for other values of α have been obtained.

The objective function $f(\mathbf{x})$ basically has a saddle shape and the promising region for the parameter estimation is a diagonal area in the $c - \beta$ plane.

Sections of $f(\mathbf{x})$ with planes perpendicular to the β axis may be approximated by the following regression formula

$$f(c) \Big|_{\substack{\alpha = \bar{\alpha} \\ \beta = \bar{\beta}}} = b_1 c^3 + b_2 c^2 + b_3 c + b_4, \quad (5.12)$$

where b_1 , b_2 , b_3 and b_4 are regression coefficients that depend on β and α .

The cubic curves represented by Eq. (5.12) are plotted in Figure 5.15 for all values of β and for $\alpha=0.93$, in case of specimen type B. The envelope of the different minima of the cubic curves of Eq. (5.12) is represented by a line that is almost horizontal. This means that a correlation exists between the length scale parameter (related to c) and the slope of the softening branch β , if only global measurements regarding the structural load vs. deformation curve of one specimen size are collected in the vector \mathbf{y}_{exp} . Consequently, the inverse problem is ill-posed, since no unique solution is guaranteed or, if a minimizer exists, the solution is not stable (for the ill-posedness definition see Section 3.3 and Figures 3.3 and 3.4). Two similar global responses may be obtained considering two different parameter sets. In Figure 5.16 the case of specimen type C is shown for two equivalent parameter sets $\mathbf{x}_1^T : [c = 50 \text{ mm}^2 \ \beta = 1200]$ and $\mathbf{x}_2^T : [c = 20 \text{ mm}^2 \ \beta = 800]$.

The equivalence between two different parameter sets may be more general than that shown in Figure 5.16, since it does not necessarily mean that the two parameter sets correspond to identical global force-deformation curves. In fact, the objective function of Eq. (5.11) is defined as a summation of differences between the computational and experimental curve. Hence, also different computational curves may correspond to identical global balance between parts of the curve that fit better and parts of the curve that fit worse with the experimental target curve.

It is worthwhile to recall here that a non-uniform distribution of experimental scatter along the entire load-displacement curve leads to parameter estimates that correspond to the optimum fitting of those parts of the curve characterized by lower scatters. In fact, data characterized by a significant uncertainty are less weighted in the computation of the objective function of Eq. (5.11). Hence, as a consequence, computational curves that provide the best fitting in these areas do not correspond to the optimal parameters estimate. Highly non-uniform scatter distributions may lead to insignificant fitting of the average experimental curve. In Figure 5.17 the experimental and computational curves related to $\mathbf{x}_1^T : [c = 80 \text{ mm}^2 \ \beta = 700]$ and $\mathbf{x}_2^T : [c = 30 \text{ mm}^2 \ \beta = 500]$ are reported for the concrete specimen BG4 of

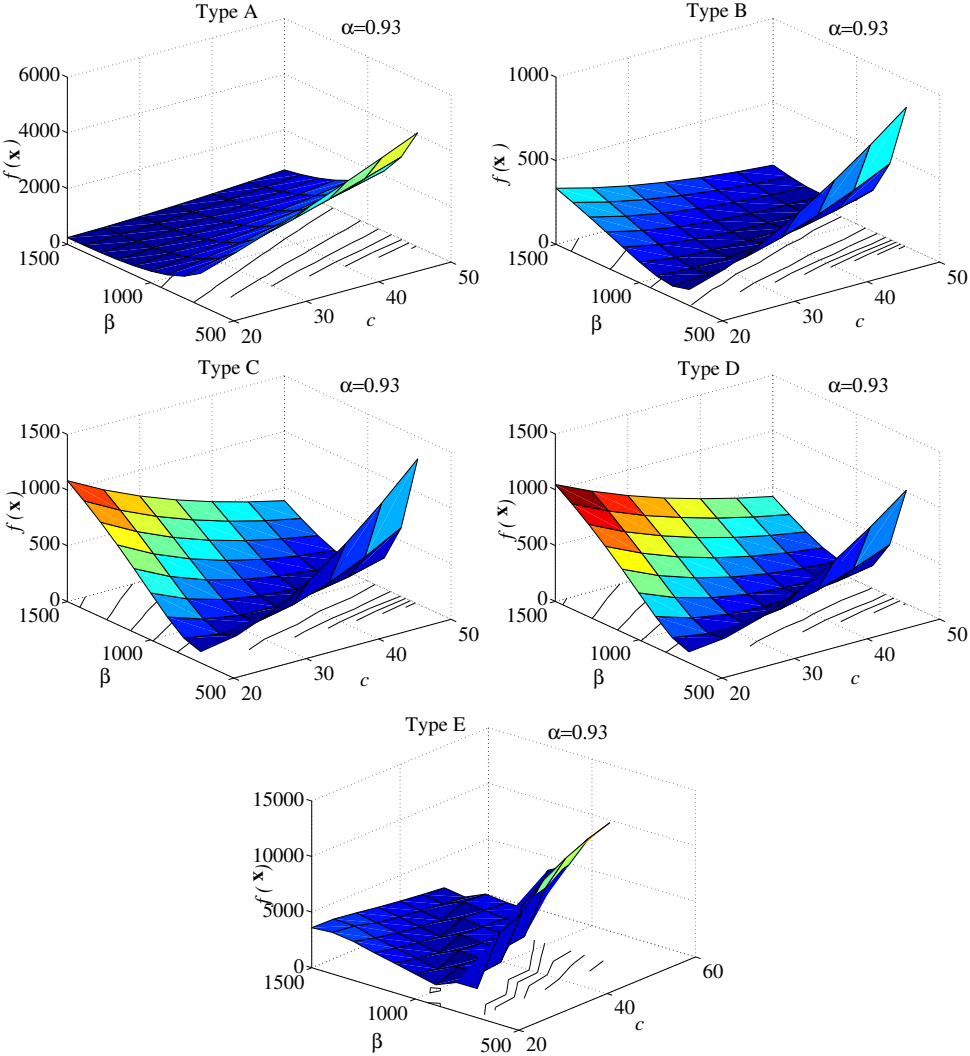


Figure 5.14: Objective function $f(\mathbf{x})$ corresponding to $\alpha=0.93$ for the different specimen sizes A-E of the experimental series n. 2.

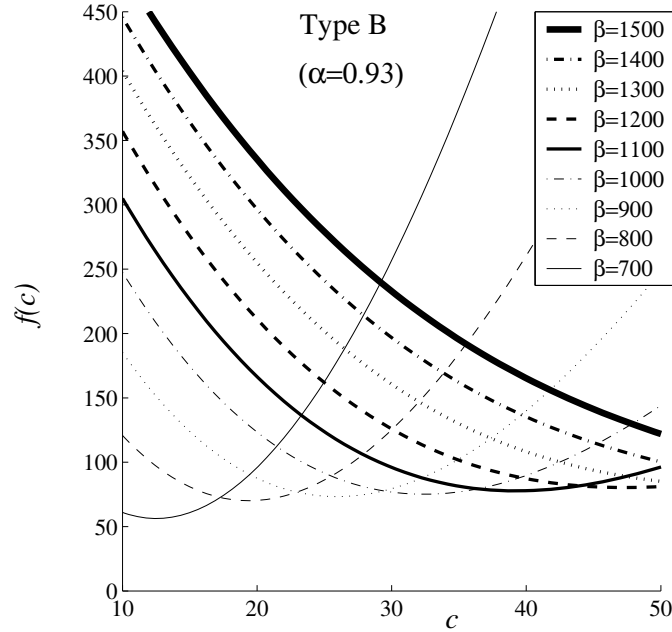


Figure 5.15: Sections of the objective function $f(\mathbf{x})$ with planes perpendicular to the β axis for $\alpha=0.93$, for specimen type B of experimental series n. 2.

	E[MPa]	ν	f_{ct}	η
specimen (concrete)	30000	0.2	2.2	15.91
loading platen	210000	0.3	-	-

Table 5.5: Values of the a priori known model parameters for experimental series n. 4 [42, 43].

the experimental series n. 4 [42, 43]. The values of the model parameters considered as a priori known for the experimental series n. 4 are listed in Table 5.5 (the platens are present only in the case of the double-edge notched tensile specimens KG). The narrow scatter band around the CMOD value of 0.26 mm behaves as a ‘singular’ point in Eq.(5.11), with the results that the experimental curve results better fitted by \mathbf{x}_1 , although \mathbf{x}_2 provides values around the peak and the tail that are closer to the experimental curve.

Usually, the tail of the load-deformation curve is characterized by smaller scatter values. Hence, the fitting process might be mainly driven by the tail.

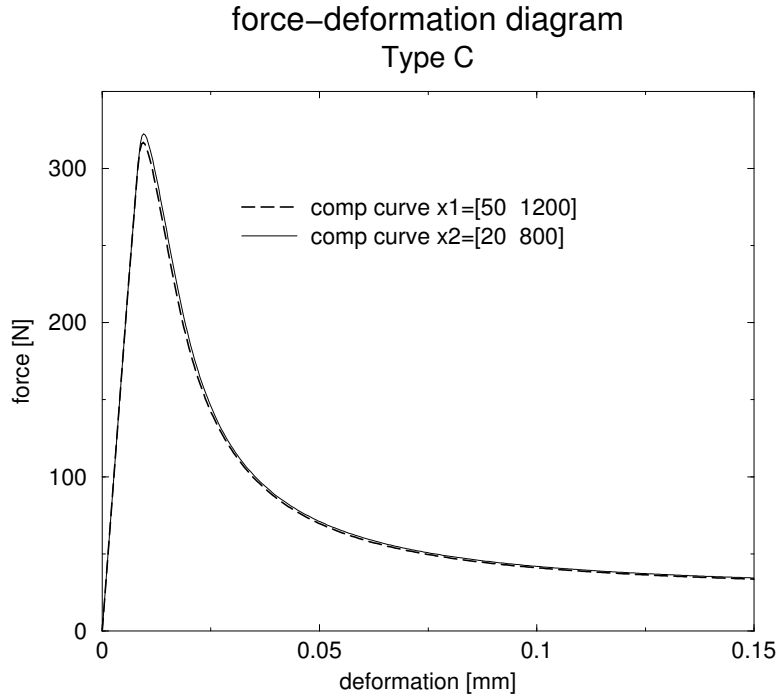


Figure 5.16: Force-deformation diagrams corresponding to the two different parameter sets $\mathbf{x}_1^T : [c = 50 \text{ mm}^2 \ \beta = 1200]$ and $\mathbf{x}_2^T : [c = 20 \text{ mm}^2 \ \beta = 800]$ ($\alpha = 0.93$) for specimen type C of the experimental series n. 2.

In order to avoid such misleading identification procedures, the last part of the tail of the diagram might be cut off for the identification of the c and β parameters and, subsequently, adjusting it only by means of α . Another reason for this tail cut off could be the length of the tail related to the length of the peak and post-peak part of the curve. In case of a long tail, even with a uniform scatter distribution along the curve, the main contribution in the computation of the objective function of Eq.(5.11) might be represented by the tail, and, as consequence, parameters sets that correspond mainly to the best fitting of the tail might be selected.

5.4.1.1 KF solution

Although the problem suffers from the lack of an unique and/or stable minimizer of the objective function $f(\mathbf{x})$, four KF procedures are considered in

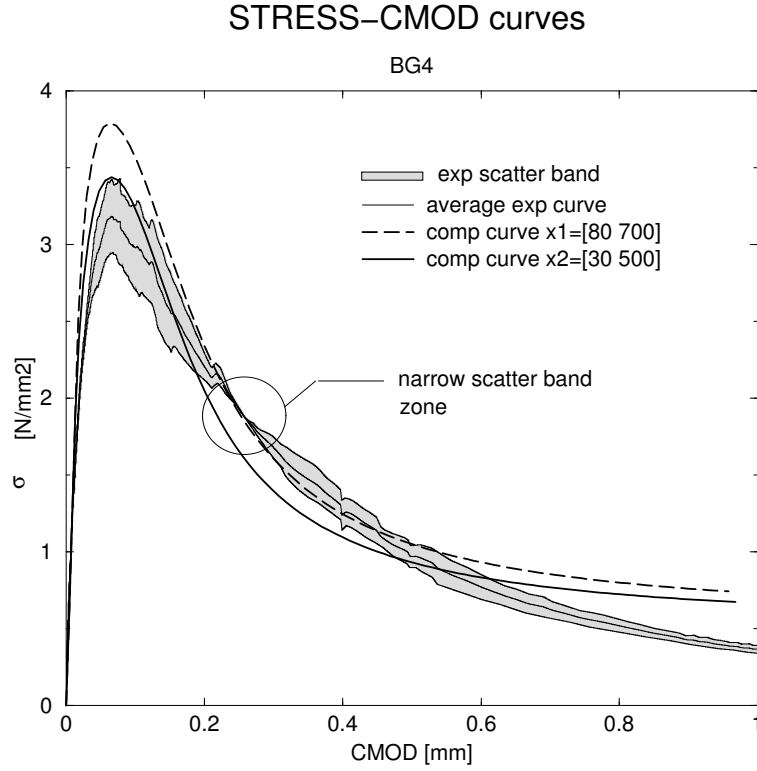


Figure 5.17: Experimental and computational stress-CMOD curves corresponding to the two parameter sets $\mathbf{x}_1^T : [c = 80 \text{ mm}^2 \beta = 700]$ and $\mathbf{x}_2^T : [c = 30 \text{ mm}^2 \beta = 500]$ for specimen BG4 of experimental series n. 4 [42, 43] ($\alpha = 0.92$). The computational curve generated by \mathbf{x}_1 results to be a better fitting due to the non-uniform experimental scatter distribution.

order to investigate the influence of \mathbf{C}_0 , \mathbf{C}_{exp} and the number of KF steps on the estimated parameter values in case of specimen type B of the experimental series n. 2. The related data are reported in Table 5.6, expressing the covariances matrices in terms of uncertainty on the mean value and considering plausible values of \mathbf{C}_0 according to the expertise and experience of the user.

In all four cases only c and β are involved in the identification procedure, with a fixed value for $\alpha = 0.95$, starting from the initial guess $\mathbf{x}_0^T = [c_0 \ \beta_0] = [40.0 \ 1200.0]$. The initial guess, the final parameter estimates of the four KF procedures and the minima of the neighborhood function of Eq. (3.5) (or Eq.

KF procedure	\mathbf{C}_0 [%]	\mathbf{C}_{exp} [%]	n. steps
KFI (ref.)	40	50.0 (real)	20
KFII	10	50.0	20
KFIII	40	5.0	20
KFIV	40	50.0	30

Table 5.6: KF procedures data

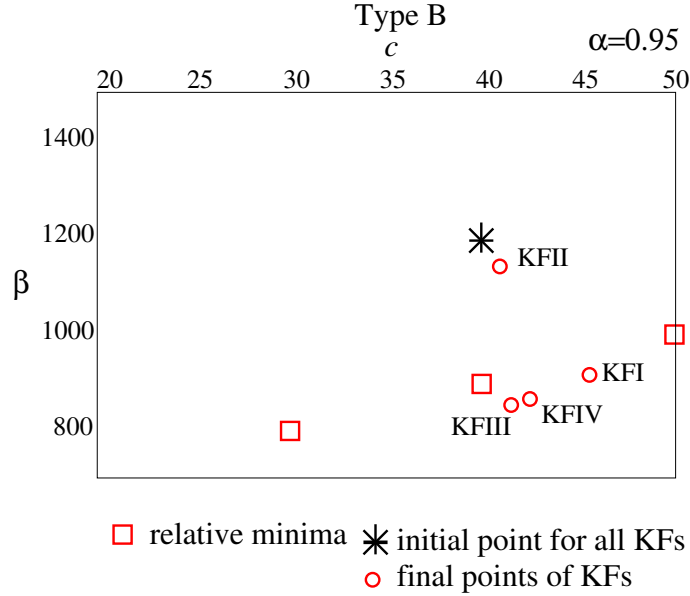


Figure 5.18: Estimated parameter sets for KFI, KFII, KFIII and KFIV.

(5.11)) (obtained through the KNN method) are reported in the parameters space $c - \beta$ in Figure 5.18. Interesting remarks can be made comparing the four KF procedures and observing Figure 5.18:

- the covariance matrix \mathbf{C}_0 associated with \mathbf{x}_0 is a measure of the uncertainty on the initial guess, and *the final solution remains confined within an area surrounding \mathbf{x}_0 proportional to \mathbf{C}_0* . Hence, the final estimate computed by KFII, characterized by the smallest covariance \mathbf{C}_0 , is close to the initial guess \mathbf{x}_0 (see Figures 5.19 and 5.20). Therefore, \mathbf{x}_0 and the related covariance have an important role in the identification procedure. In fact, if an additional penalty term concerning the initial guess is introduced in the neighborhood function of Eq. (3.5)

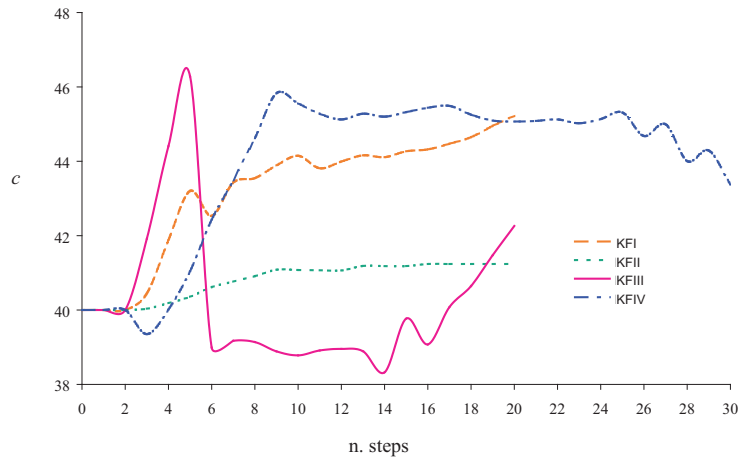


Figure 5.19: c parameter estimation vs KF step number for the four KF procedures (the last step values correspond to the c values of the four circle points of Figure 5.18).

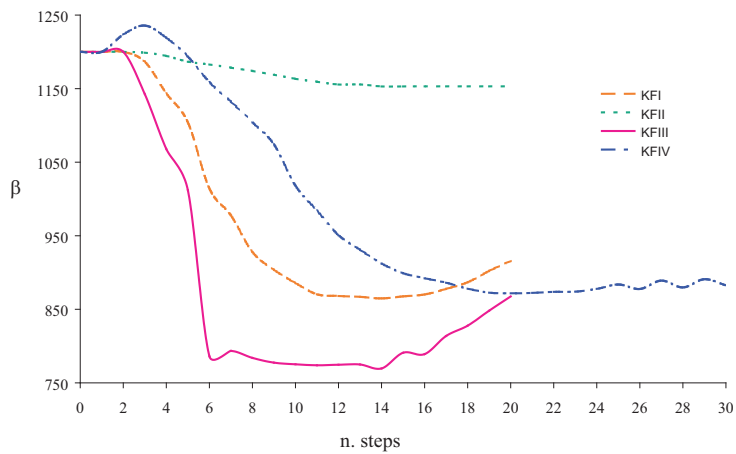


Figure 5.20: β parameter estimation vs KF step number for the four KF procedures (the last step values correspond to the β values of the four circle points of Figure 5.18).

$$f(\mathbf{x}) = (\mathbf{y}_{\text{exp}} - \mathbf{y}_{\text{comp}}(\mathbf{x}))^T \mathbf{C}_{\text{exp}}^{-1} (\mathbf{y}_{\text{exp}} - \mathbf{y}_{\text{comp}}(\mathbf{x})) + (\mathbf{x} - \mathbf{x}_0)^T \mathbf{C}_0^{-1} (\mathbf{x} - \mathbf{x}_0), \quad (5.13)$$

the function $f(\mathbf{x})$ takes a convex shape that is related to \mathbf{C}_0 , as shown in Figure 5.21. This points out the important role of \mathbf{C}_0 and \mathbf{x}_0 in the final parameters estimate.

- An area of uncertainty proportional to \mathbf{C}_{exp} may be defined around the mean value $\mathbf{y}_{\text{exp}}^t$. Numerical solutions within that area are considered good approximations of the experimental solution. Hence, a narrow band around the mean value leads to select a computational curve close to the mean value. In fact, in case of the KFIII, with the smallest \mathbf{C}_{exp} , the final estimate \mathbf{x} is forced to correspond to a numerical solution $\mathbf{y}_{\text{comp}}^t(\mathbf{x})$ close to $\mathbf{y}_{\text{exp}}^t$, approaching the local minimum of the neighborhood function.

Hence, from the above two points the following conclusion can be drawn:

- if a discrepancy between the computational and the experimental curve exists, the KF performs well in minimizing this discrepancy only if a narrow band around the experimental average curve is defined by \mathbf{C}_{exp} and a large enough band around the computational curve corresponding to the initial guess is defined by \mathbf{C}_0 (see Figure 5.22).

Moreover:

- the final estimate is improved by increasing the number of KF steps, as in the case of KFIV (see Figure 5.18).
- The parameter sets identified by the four KF procedures converge to the same local minimum (except KFII), being the starting point in that attraction basin.

In addition, as already mentioned in Section 3.4, the KF procedure updates, at each step t , the model parameters estimate on the basis of the current experimental information, so that the evolution of internal length scale parameter may be investigated during the fracture process. In the case of the specimen type B and procedure KFIII, for instance, Figure 5.23 shows that the first part of the post peak experimental force-deformation curve is

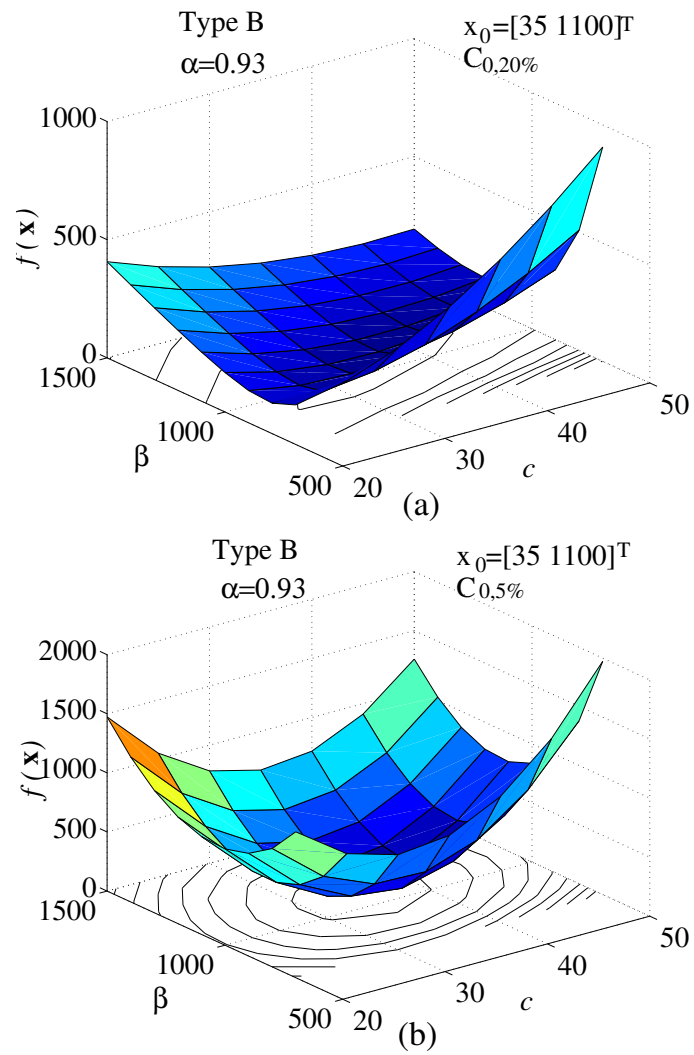


Figure 5.21: The effect of the covariance \mathbf{C}_0 associated to the initial guess \mathbf{x}_0 on the neighborhood function $f(\mathbf{x})$: (a) the case of $\mathbf{C}_0=20\%$ and (b) the case of $\mathbf{C}_0=5\%$

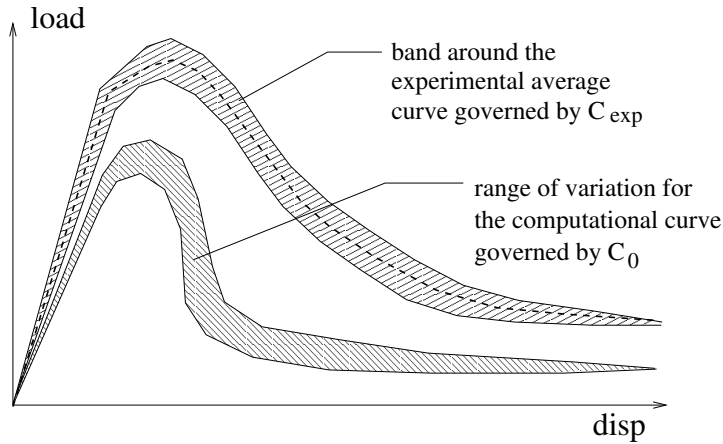


Figure 5.22: Meaning of C_0 and C_{exp} .

better fitted using higher values of c , the central part of the softening branch corresponds to a smaller roughly constant value of the length scale, while, at the end, c tends to increase because of the tail. However, this tail effect, as already previously mentioned, may be better regulated by adjusting the α parameter.

5.4.2 Global curves of different sizes

The ill-posedness of the inverse problem is not solved if global force vs. deformation curves of different specimen sizes are considered in the identification problem. The load-displacement curves corresponding to two equivalent parameter sets are presented in Figure 5.24 for the dog-bone shaped specimens of the experimental series n. 2 [87, 88]: similar curves are found for all specimen sizes using two equivalent parameter sets. The promising areas (diagonal lines), corresponding to the best parameters sets, are plotted in Figure 5.25 on the parameters grid used for the KNN method, for all sizes of the experimental series n. 2 (projection of the saddles of the objective function $f(\mathbf{x})$ of Figure 5.14 on the $c - \beta$ plane). A similar coupling between the two parameters c and β is found, in the same direction for all specimen sizes. Hence, involving the force-deformation curves of different specimen sizes in the objective function (Eq. (3.5)) does not provide uniqueness and/or stability to the inverse solution.

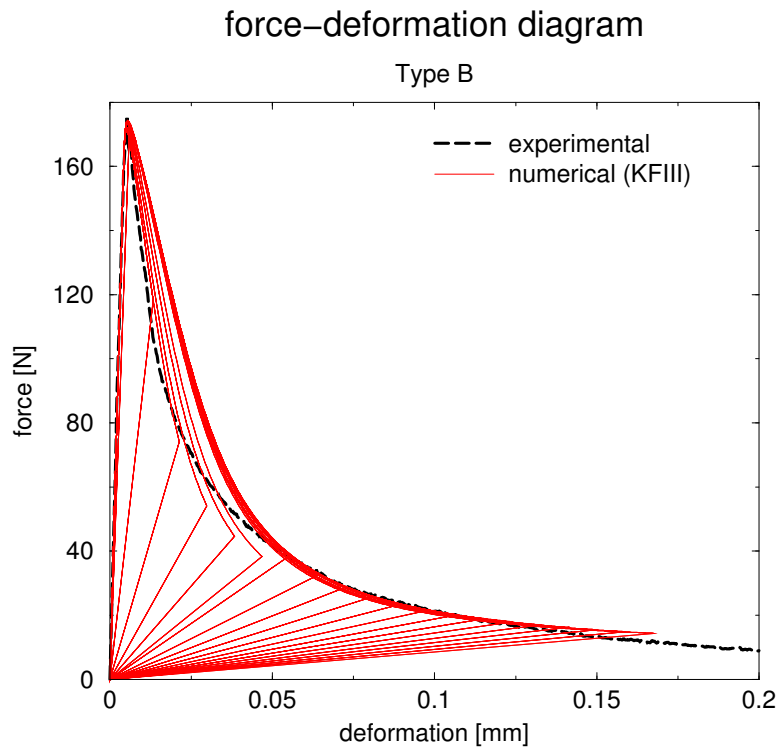


Figure 5.23: Experimental and computational (KFIII) force deformation curves for the concrete dog-bone shaped specimen Type B of the experimental series n. 2 [87, 88].

5.5 Size effect

As already mentioned in Section 2.1, the size effect phenomenon can be exploited in an inverse procedure to identify the model parameters [22, 55, 73, 81]. In this case only the peak loads of the force-deformation curves of different specimen sizes are considered in the solution of the inverse problem. However, since only peak loads are the objective of the data fitting, the ill-posedness of the parameter identification problem remains, analogously to the previous case.

Moreover, the gradient-enhanced damage model seems to incorrectly reproduce the entire experimental size effect curve using only one parameters set for all specimen sizes. This is shown, for instance, in Figure 5.26 in case

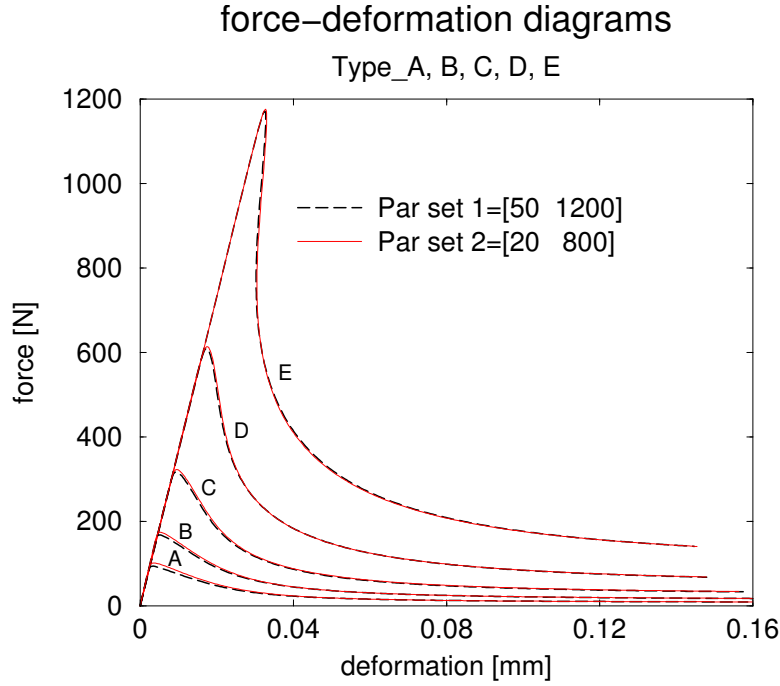


Figure 5.24: Force-deformation curves of all sizes of the dog-bone shaped specimens of the experimental series n. 2 [87, 88], for two equivalent parameter sets $\mathbf{x}_1^T : [c = 50 \text{ mm}^2 \ \beta = 1200]$ and $\mathbf{x}_2^T : [c = 20 \text{ mm}^2 \ \beta = 800]$ ($\alpha = 0.93$).

of the experimental series n. 2. Considering the curve corresponding to the parameter set $[c = 50 \text{ mm}^2 \ \beta = 1500]$ as a reference curve, a decrement of the gradient parameter c ($=20$) or of the parameter β ($=700$) causes mainly a shift in the vertical direction or a very small rotation of the computational curve. An analogous trend is shown in Figure 5.27 in case of the bending specimens of the experimental series n. 4. Hence, the computational size effect curve remains too flat compared to the experimental one.

A possible explanation for this is related to the limits of the model in reproducing experimental tests characterized by a certain statistical effect: the statistical distribution of the model parameters, or the statistical variation of the local material properties and weak spots in the different sizes may play an important role that can not be properly reproduced by the adopted deterministic model [54, 75, 89]. Moreover, the thickness of the specimen is

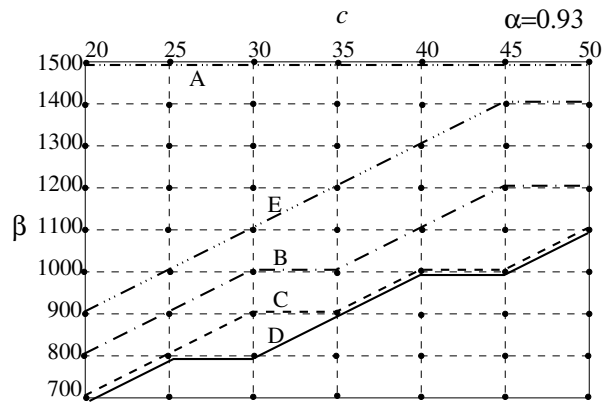


Figure 5.25: Diagonal promising lines for the various sizes of the dog-bone shaped specimens of the experimental series n. 2 [87, 88] (projection of the saddles of the objective function $f(\mathbf{x})$ of Figure 5.14 on the parameters grid) ($\alpha = 0.93$).

constant for all sizes. As a consequence, in the specimens type A and B, in addition to the strain gradients in the plane of the dog-bone specimen due to the load eccentricity, also out-of-plane strain gradients could develop, which are not included in the two-dimensional plane stress numerical model [29, 87]. Furthermore, it could be questionable if the model parameters, or some of them, are only constants to be calibrated according to a simple data fitting or they are variables as a result of all error sources discussed in Chapter 3.

The fact that the experimental average nominal strength of the smallest specimen type A is lower compared to the larger specimen sizes can be caused by different factors, as reported in [87]. The strength values for the specimen type A show a scatter which is much larger than the other specimen sizes. This is partially due to the higher number of repeated tests for the smallest size and partially to the small aspect ratio between the smallest structural dimension ($0.6D=30$ mm) and the maximum aggregate size ($=8$ mm). The ultimate strength of the specimen can have a smaller or higher value depending on whether a large aggregate is present or not in the middle section of the specimen (where failure takes place, considering the shape of the specimens). In fact, in the first case large stress concentrations develop in the neighborhood of the aggregate. This reduces the ultimate load, since restricted stress redistribution are possible in the small cross section of the specimen type A. The small specimen dimension has also an influence regarding the wall

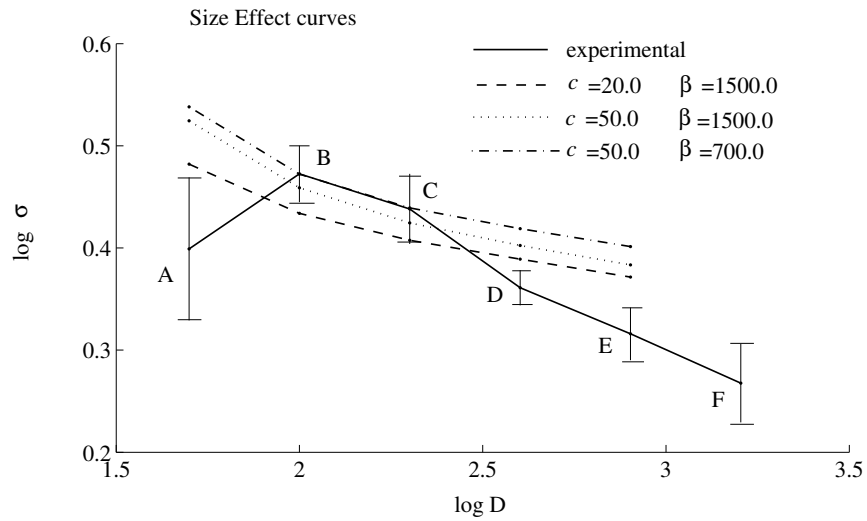


Figure 5.26: Experimental and computational size effect curves for the dog-bone shaped specimens (A to F size) of the experimental series n. 2 [87, 88] ($\alpha = 0.93$).

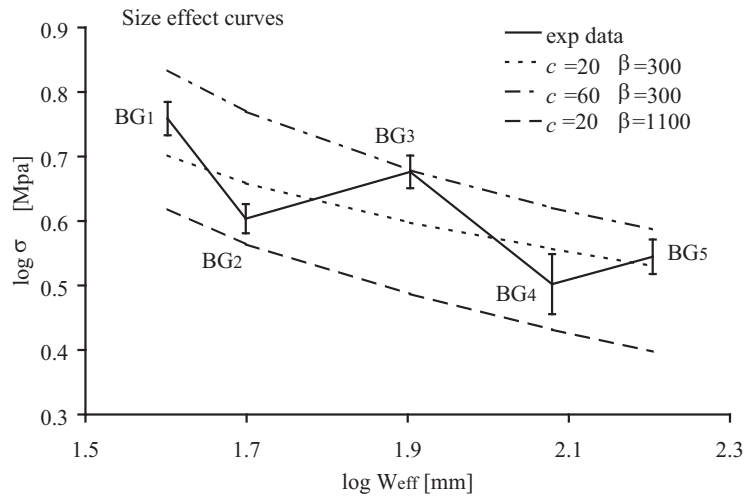


Figure 5.27: Experimental and computational size effect curves for the single-edge notched bending specimens (BG1 to BG5 size) of the experimental series n. 4 [42, 43] ($\alpha = 0.92$).

effect, which is responsible for a poor concrete quality in the zone along the specimen edges. These zones represent a considerable part for the smallest specimen, so that a larger variation of concrete strength can be expected for this specimen size. Increasing the size of the specimen the influence of the wall effect reduces. Finally, the lower value of strength for the specimen type A can also be partially due to a lower degree of hydration compared to the larger specimens. In fact, due to the larger specific area of the specimen type A, the dry process is faster and less water is left for hydration of the cement [87].

By using a single parameter set for all specimen sizes, only an *unstable average* fitting of the size effect curve can be reached. In other words, different parameter sets can be found which correspond to slightly different computational size effect curves representing an average fitting of the experimental curve. This is shown in Figures 5.28 and 5.29 for the case of the bending tests of the experimental series n. 4 (belonging the parameter set [$c = 25 \text{ mm}^2$ $\beta = 350$] to the saddle of the objective function $f(\mathbf{x})$).

In addition, a single parameters estimate that provides an acceptable fitting of the entire force-deformation curves of a few specimen sizes does not necessarily correspond to a correct prediction of the peak loads, as shown in Figures 5.30 and 5.31 for the case of the dog-bone shaped specimens of the experimental series n. 2. This aspect might also be emphasized by the errors due to the averaging operation, already mentioned in Section 3.3. In fact, the average load-deformation curve might be characterized by a peak load that is different from the average of the peaks, since the various curves, corresponding to the repeated experiments, might be slightly shifted along the strain axis.

Different parameter sets, for the various specimen sizes, are necessary to reproduce the real size effect curve. For the experimental series n. 4, the parameter sets that provide the best fitting of only the peak load (circle points) or of the entire force-deformation curve (cross points) are reported in the parameters space of Figure 5.32a for each specimen size, while the corresponding peak loads are shown in Figure 5.32b. Hence, not only the best estimates are different for the various sizes, but they also result to be different depending on whether only the peak load or the entire force-deformation curve is involved in the inverse problem.

However, in order to obtain a satisfactory fitting, it might be better to consider a size dependent length scale parameter (see Chapter 6). For instance, in the case of the double-edge notched tensile specimens of the ex-

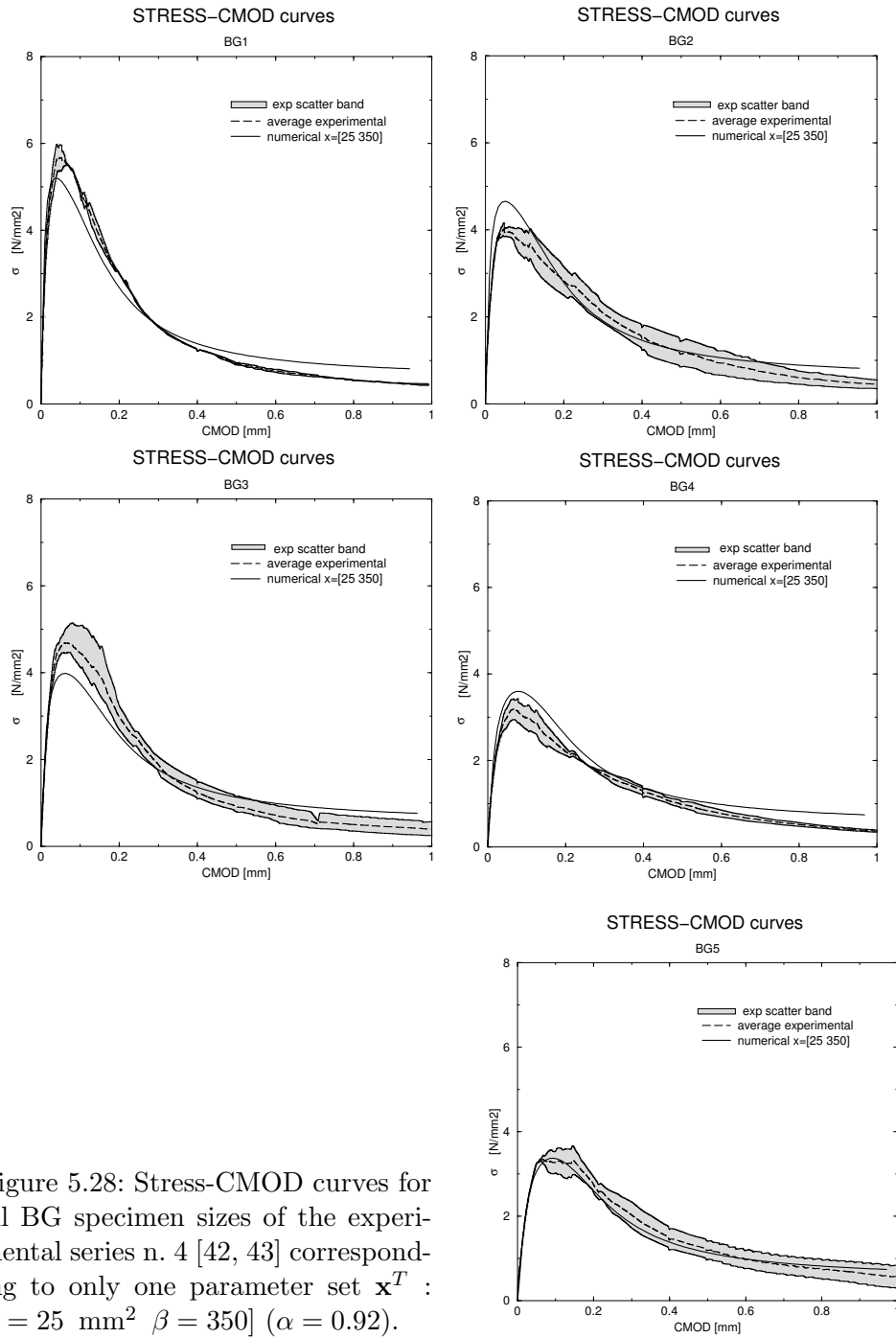


Figure 5.28: Stress-CMOD curves for all BG specimen sizes of the experimental series n. 4 [42, 43] corresponding to only one parameter set \mathbf{x}^T : $[c = 25\ \text{mm}^2\ \beta = 350]$ ($\alpha = 0.92$).

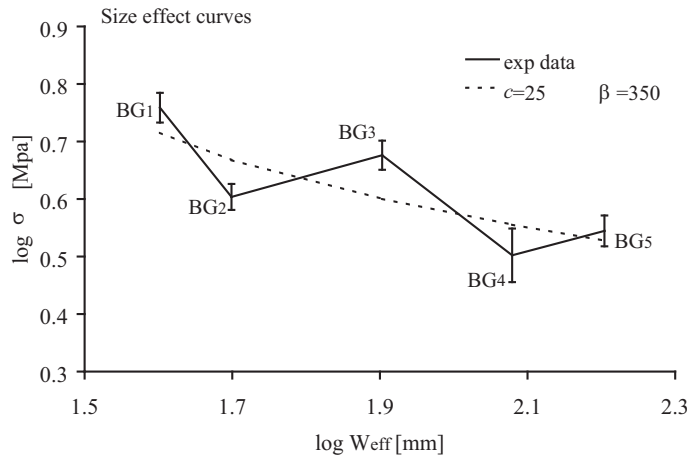


Figure 5.29: Experimental and computational size effect curves corresponding to the stress-CMOD curves of Figure 5.28 for the single-edge notched bending specimens (BG1 to BG5 size) of the experimental series n. 4 [42, 43] ($\alpha = 0.92$).

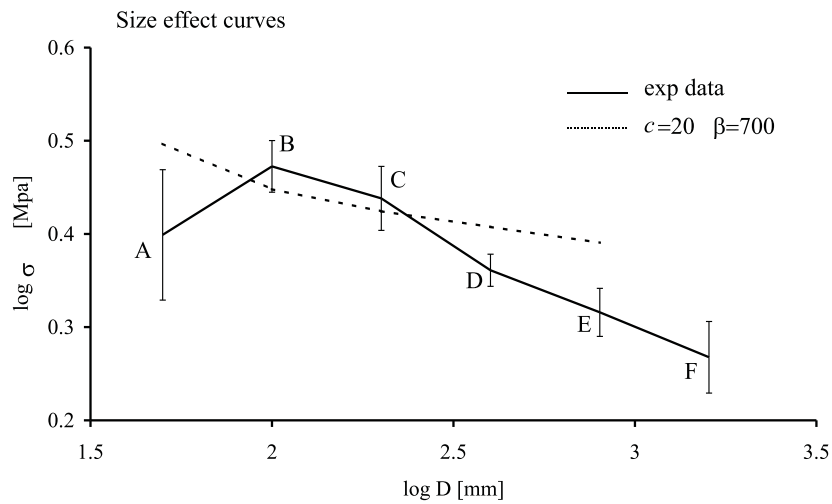


Figure 5.30: Experimental and computational size effect curves corresponding to the load-deformation curves of Figure 5.31 for the dog-shaped specimens (A to F size) of the experimental series n. 2 [87, 88] ($\alpha = 0.93$).

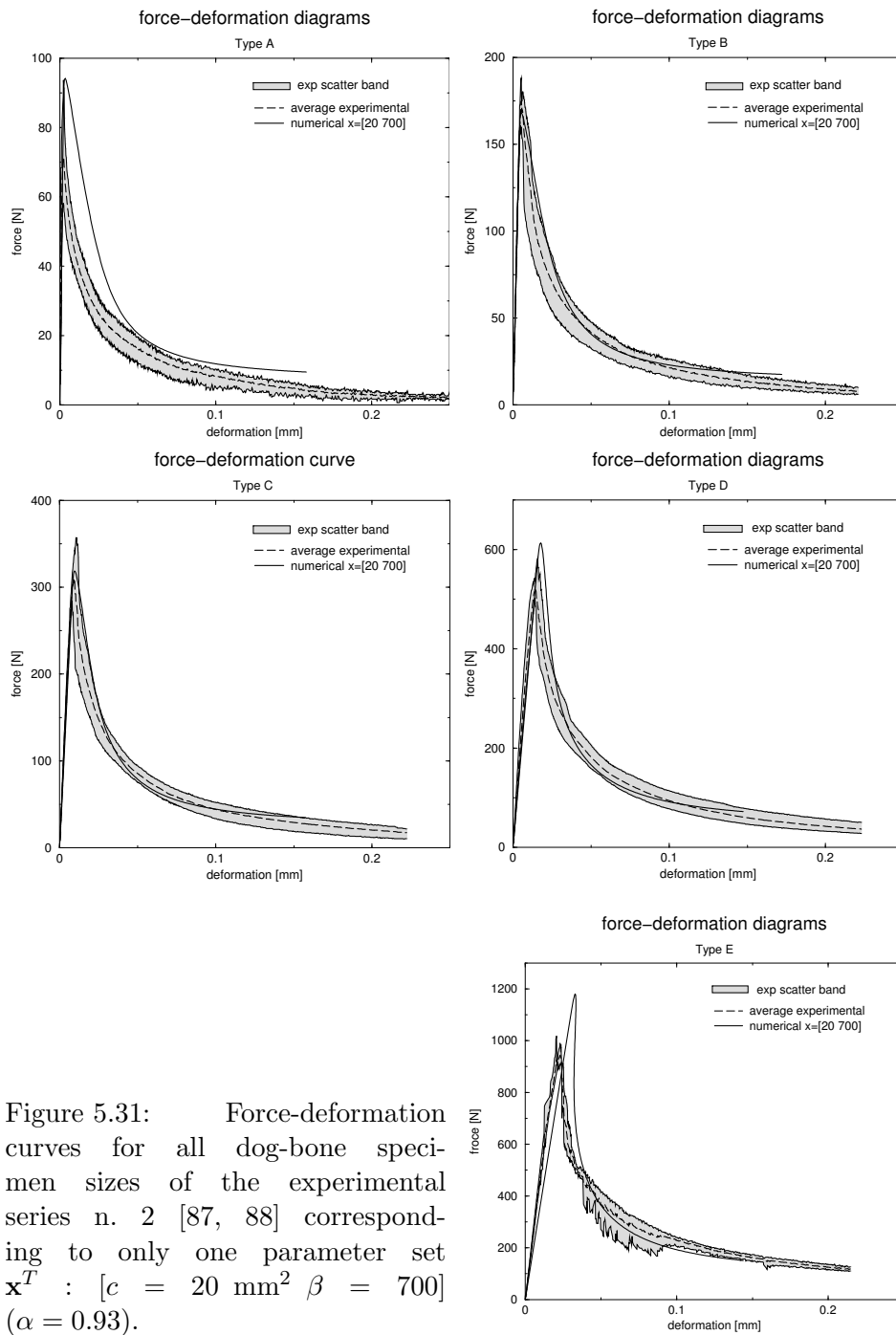


Figure 5.31: Force-deformation curves for all dog-bone specimen sizes of the experimental series n. 2 [87, 88] corresponding to only one parameter set $\mathbf{x}^T : [c = 20 \text{ mm}^2 \beta = 700]$ ($\alpha = 0.93$).

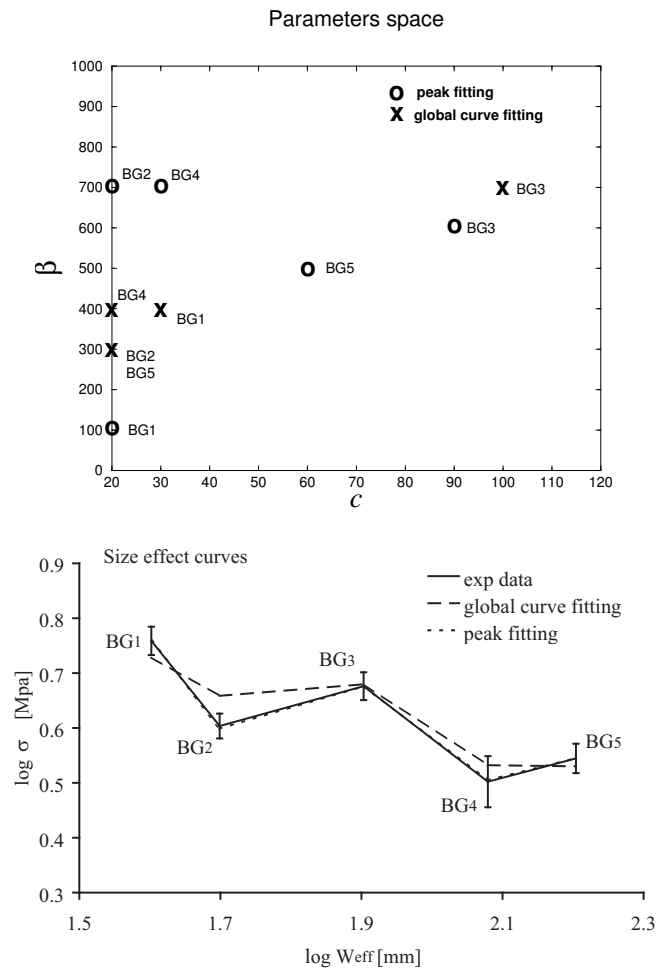


Figure 5.32: (a) Parameter sets that provide the best fitting of only the peak load (circle points) or of the entire global stress-CMOD curve (cross points), in the parameters space, for each specimen size of the experimental series n. 4 [42, 43] (BG1 to BG5) and (b) corresponding computational size effect curves. ($\alpha = 0.92$)

perimental series n. 4, an acceptable size effect fitting (only peak loads) may be achieved considering a fixed value of $\beta = 500$ and different values of the gradient parameter c , as shown in Figures 5.33 and 5.34 (note the reduced parameters grid). Nevertheless, choosing a size dependent length scale is not an acceptable solution, since this parameter is considered to be independent of size.

Finally, the size effect curves reproduced by the numerical model, using a single parameters set for all specimen sizes, present a curvature of the same type as the Carpinteri MFSL law. The comparison between the computational size effect curves (using the parameter sets corresponding to the global responses of Figures 5.28 and 5.31), Bažant SEL and Carpinteri MFSL curves (corresponding to the fitting of the experimental peak loads) are shown in Figures 5.35 and 5.36 for the experimental series n. 2 and n. 4, respectively.

5.6 Global and local data

The correlation between the two model parameters c and β , shown in Section 5.4 (see Figures 5.14, 5.16 and 5.24), suggests the use of additional experimental information. These data may be used as criteria for selecting a proper parameters vector between those vectors equivalent in terms of structural global response and represented by the saddle shaped area of the objective function $f(\mathbf{x})$ (see Figure 5.14). However, the main issue is to establish which type of data is necessary for this purpose.

5.6.1 Global and local curves of one single size

5.6.1.1 Experimental series n. 3

The experimental results of the three-point bending tests on notched concrete beams of the series n. 3 are considered [32]. In this case, in addition to the global force-deformation curve, the deformations in some points in the neighborhood of the macrocrack are also registered during the fracture process (see strain gauges positions in Figure 4.3). The values of the parameters considered as a priori known for the experimental series n. 3 are reported in Table 5.7.

The results indicate that parameter sets equivalent in terms of global response correspond also to a similar development of strains in points that are

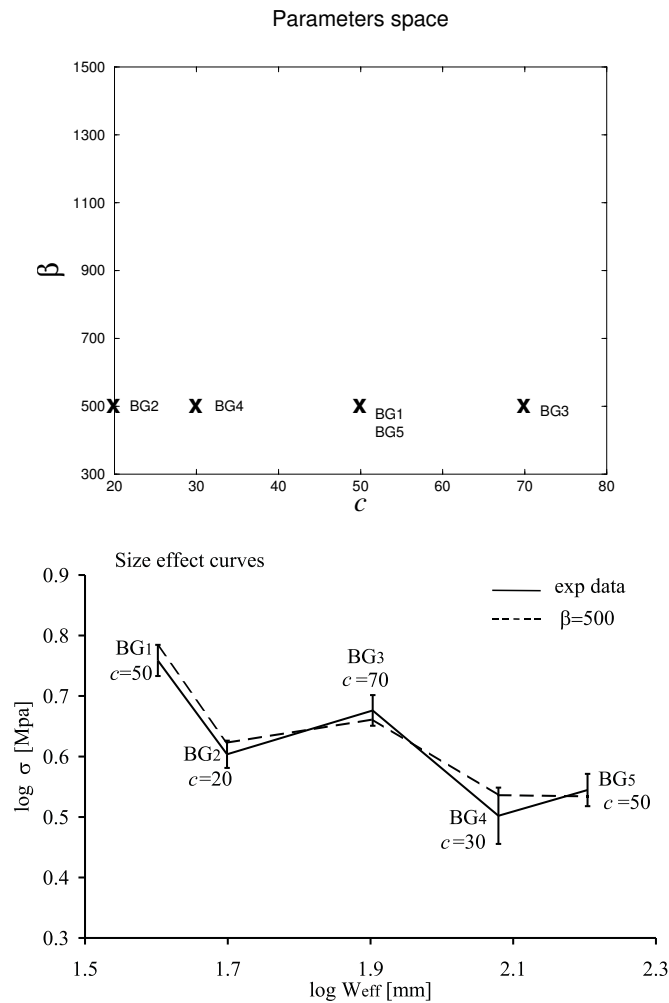


Figure 5.33: (a) Parameter sets that provide the best peaks fitting keeping constant β , in the parameters space, for each specimen size of the experimental series n. 4 [42, 43] (BG1 to BG5) and (b) corresponding computational size effect curve. The stress-CMOD curves related to these parameter sets are shown in Figure 5.34. $\alpha = 0.92$

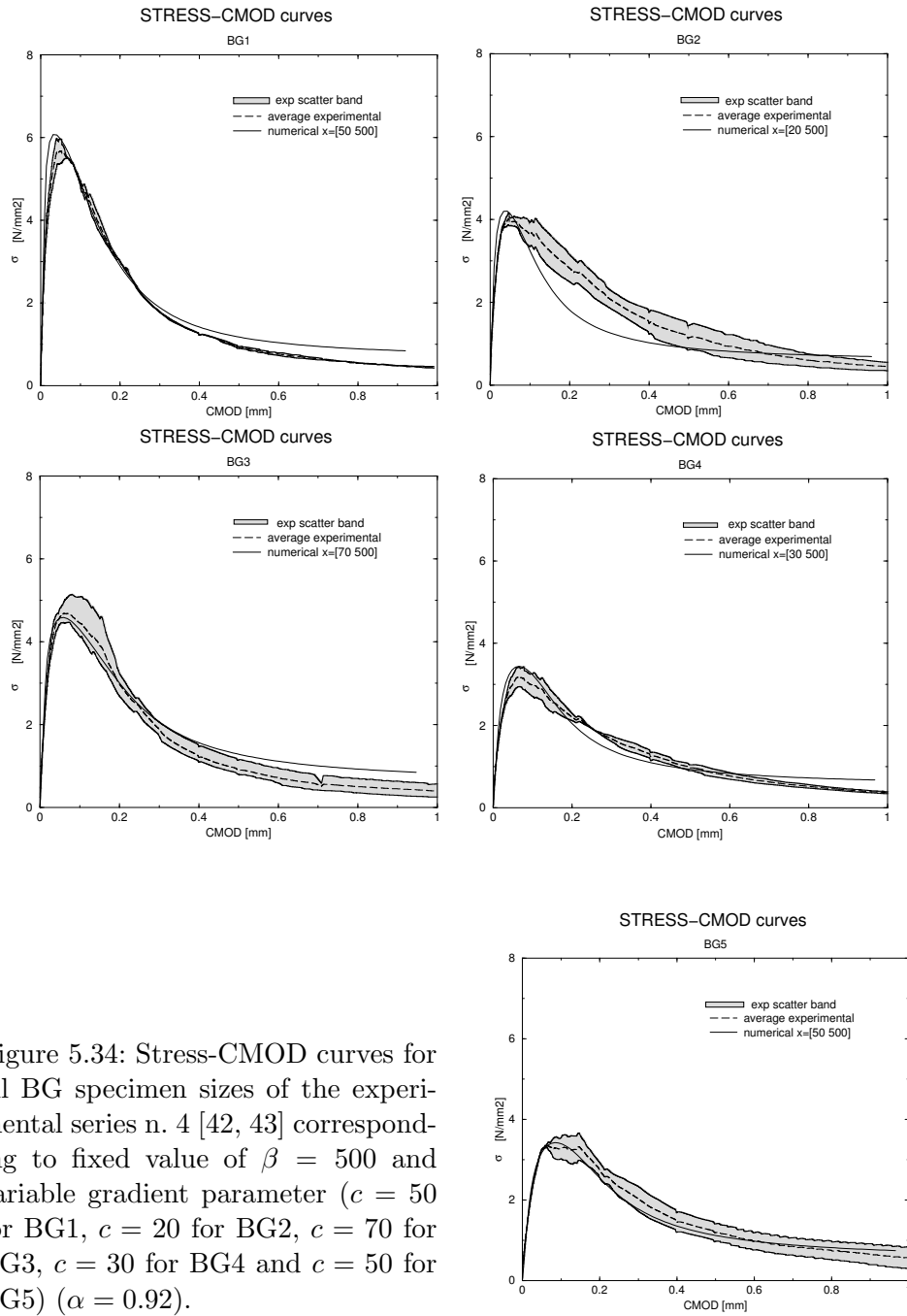


Figure 5.34: Stress-CMOD curves for all BG specimen sizes of the experimental series n. 4 [42, 43] corresponding to fixed value of $\beta = 500$ and variable gradient parameter ($c = 50$ for BG1, $c = 20$ for BG2, $c = 70$ for BG3, $c = 30$ for BG4 and $c = 50$ for BG5) ($\alpha = 0.92$).

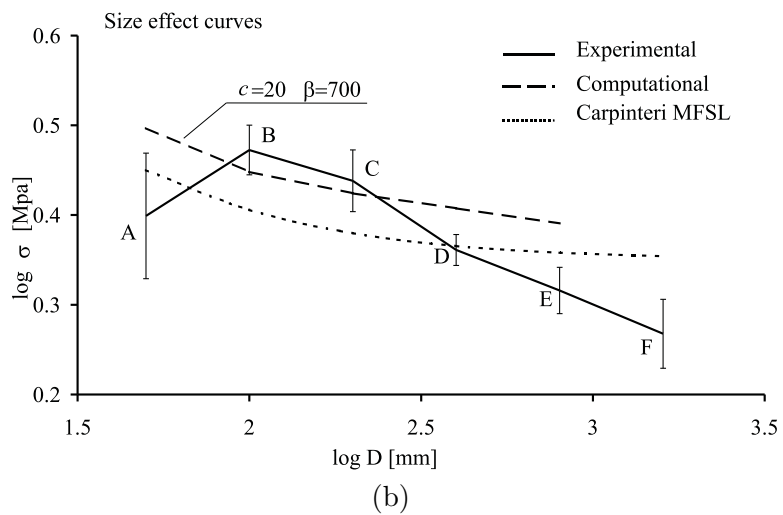
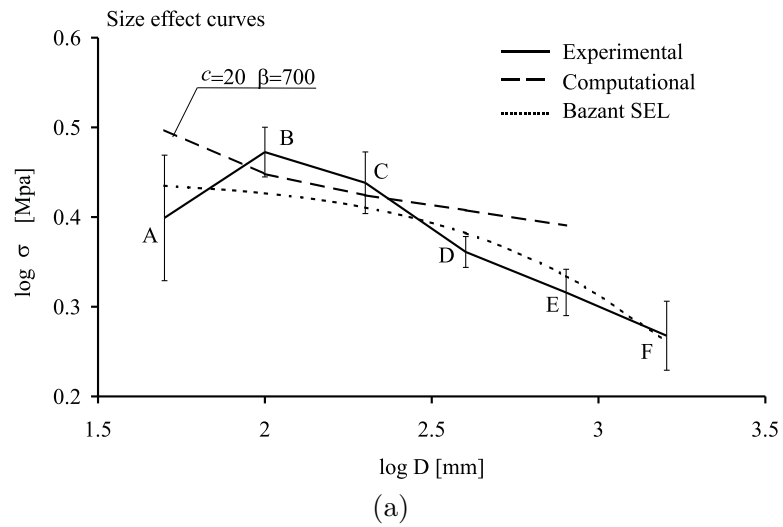


Figure 5.35: Experimental, computational and (a) Bažant SEL (b) Carpinteri MFSL fitting size effect curves for the dog-bone shaped specimens (A to F size) of the experimental series n. 2 [87, 88] ($\alpha = 0.93$).

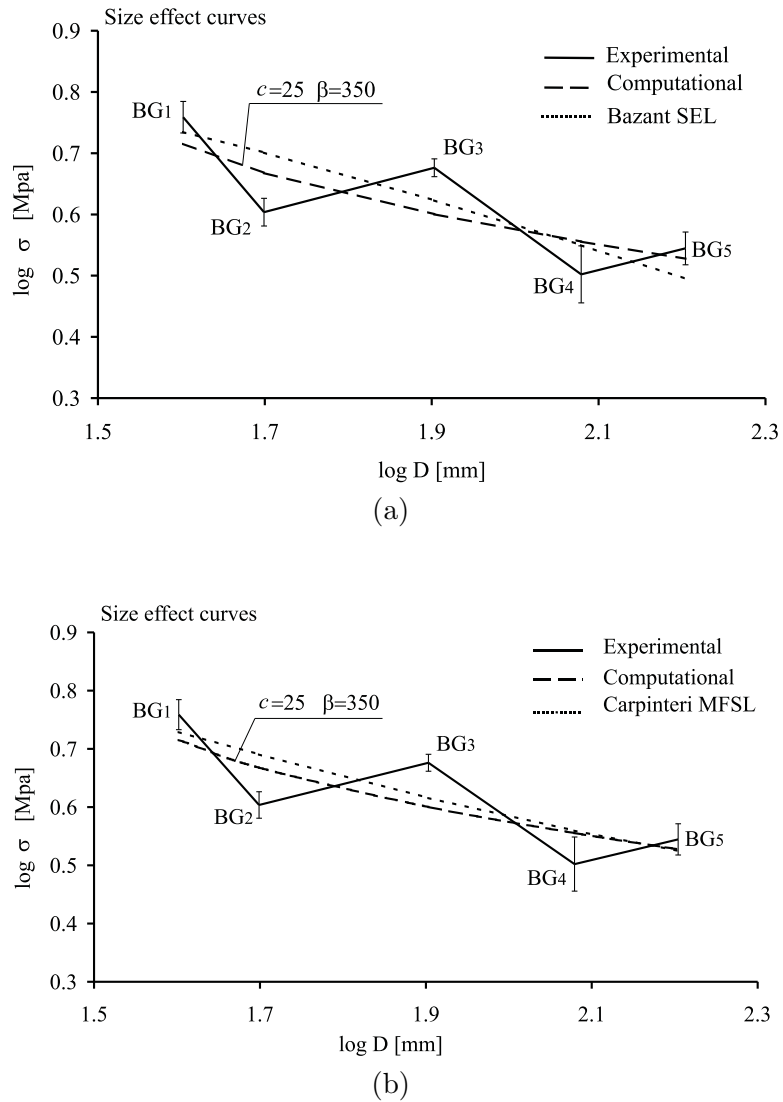


Figure 5.36: Experimental, computational and (a) Bažant SEL (b) Carpinteri MFSL fitting size effect curves for the single-edge notched bending specimens (BG1 to BG5 size) of the experimental series n. 4 [42, 43] ($\alpha = 0.92$).

E[MPa]	ν	f_{ct}	η
34760	0.2096	3.38	11.73

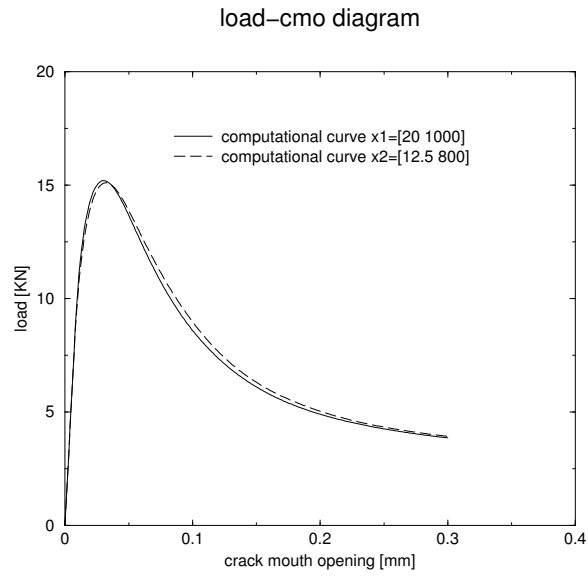
Table 5.7: Values of the a priori known model parameters for the experimental series n. 3 [32].

outside the area where damage and strains localize. In Figure 5.37a the computational load-CMO curves corresponding to two equivalent parameter sets are reported. The two parameter sets provide a similar evolution of the deformations at the points where the inductive displacement transducer IDT3 and the strain gauges SG3/SG6 are placed (see Figure 4.3), as shown in Figures 5.37b and 5.38. Hence, involving deformation data related to points outside the localization zone does not provide additional criteria for the selection of a unique solution. Instead, for points within that area no comparison between the numerical and the experimental deformation is possible, since limited values in the case of the real discrete crack (as the ones registered by the strain gauges SG2/SG5) correspond to high numerical values in the computational continuum smeared approach.

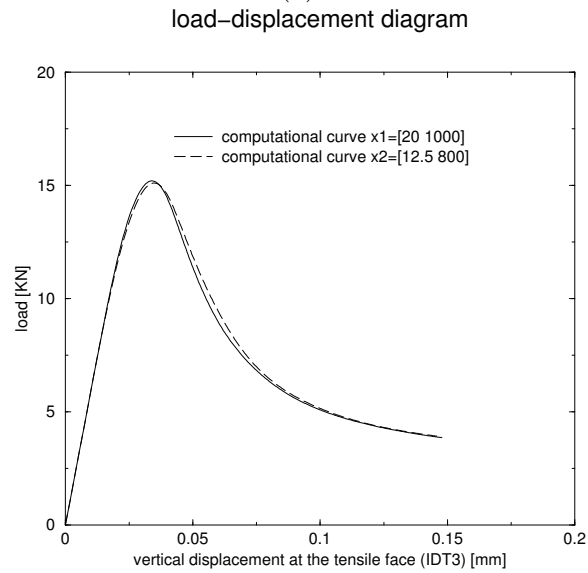
5.6.1.2 One-dimensional bar

These results promote the idea of considering *averaged local* information, instead of *localized* data, in the solution of the inverse problem. In fact, numerical simulations show that parameter sets equivalent in terms of global response correspond to different strain profiles along the main direction of the specimen and different widths of the fracture process zone (FPZ) (e.g. [36]).

The effect of adding local experimental information in the definition of the neighborhood function Eq. (3.5) is investigated in the simple case of a one-dimensional bar in tension, with a weak zone in the middle part, where deformation and damage localize. The load-deformation curve, the damage profile and the equivalent strain profile along the bar represent the solution of the forward problem. Pseudo-experimental data are created artificially considering analytical curves that are close to the computational curves corresponding to the following reference parameters set: $\mathbf{x}^T = [c \ \beta] = [30.0 \ 1500]$ (see Figure 5.39). The remaining model parameters, considered as a priori known, are $E=20000$ [MPa], $\nu=0.0$ $\alpha=0.95$, $\kappa_i=0.0001/0.00009$ (the smaller value for the weak part of the bar) and $\eta=14.00$. Geometrical data are: bar length 100.0 mm, length of the weak part 10 mm, cross-section area 10 mm².



(a)



(b)

Figure 5.37: (a) Computational force-CMO curve and (b) computational force-displacement curve at the tensile face IDT3 (see Figure 4.3) for two equivalent parameter sets \mathbf{x}_1^T : [$c = 20.0 \text{ mm}^2$ $\beta = 1000$] and \mathbf{x}_2^T : [$c = 12.5 \text{ mm}^2$ $\beta = 800$] for the experimental series n. 3 [32].

The neighborhood function $f(\mathbf{x})$ may be rewritten in the following form, with three separate contributions:

$$f(\mathbf{x}) = \underbrace{\frac{(\mathbf{y}_{\text{exp}} - \mathbf{y}_{\text{comp}}(\mathbf{x}))^T (\mathbf{y}_{\text{exp}} - \mathbf{y}_{\text{comp}}(\mathbf{x}))}{(\mathbf{y}_{\text{exp}})^T (\mathbf{y}_{\text{exp}})}}_1 + \underbrace{\frac{(\boldsymbol{\omega}_{\text{exp}} - \boldsymbol{\omega}_{\text{comp}}(\mathbf{x}))^T (\boldsymbol{\omega}_{\text{exp}} - \boldsymbol{\omega}_{\text{comp}}(\mathbf{x}))}{(\boldsymbol{\omega}_{\text{exp}})^T (\boldsymbol{\omega}_{\text{exp}})}}_2 + \underbrace{\frac{(\boldsymbol{\varepsilon}_{\text{eq,exp}} - \boldsymbol{\varepsilon}_{\text{eq,comp}}(\mathbf{x}))^T (\boldsymbol{\varepsilon}_{\text{eq,exp}} - \boldsymbol{\varepsilon}_{\text{eq,comp}}(\mathbf{x}))}{(\boldsymbol{\varepsilon}_{\text{eq,exp}})^T (\boldsymbol{\varepsilon}_{\text{eq,exp}})}}_3, \quad (5.14)$$

where in the vectors $\boldsymbol{\omega}$ and $\boldsymbol{\varepsilon}_{eq}$ points are collected along the final damage profile curve and final equivalent strain profile curve (see Figure 5.39b and c), respectively. Using the KNN method, a population of model parameter sets \mathbf{x}_i is chosen and the approximation of the neighborhood function is built from the evaluations of $f(\mathbf{x}_i)$. The plots and contour plots of $f(\mathbf{x})$ are reported in Figure 5.40 considering the various contributions in Eq. (5.14). The second and third term in Eq. (5.14) lead, separately, to a correlation between c and β in a different direction with respect of the one related to the first term (note the different directions of the saddle areas in Figure 5.40). Hence, considering both terms, the final solution \mathbf{x} can be univocally defined as a crossing point of two correlation zones or three correlation zones (see Figure 5.40).

5.6.1.3 Experimental series n. 4

For realistic parameter identifications the data of the experimental series n. 4 are used. In this case, *local* FPZ width-deformation curves (i.e. FPZ widths measurements during the entire fracture process) are available in addition to the *global* stress-CMOD curves. Hence, the width of the damaged area d (i.e. the area that is not completely virgin) may be used as additional experimental data in the solution of the inverse problem.

The idea of considering averaged local quantities seems to be consistent with the fact that the real discrete fracture process is described through a continuum smeared approach. However, the main difficulty is to establish a method for relating the computational strain and/or damage distribution to

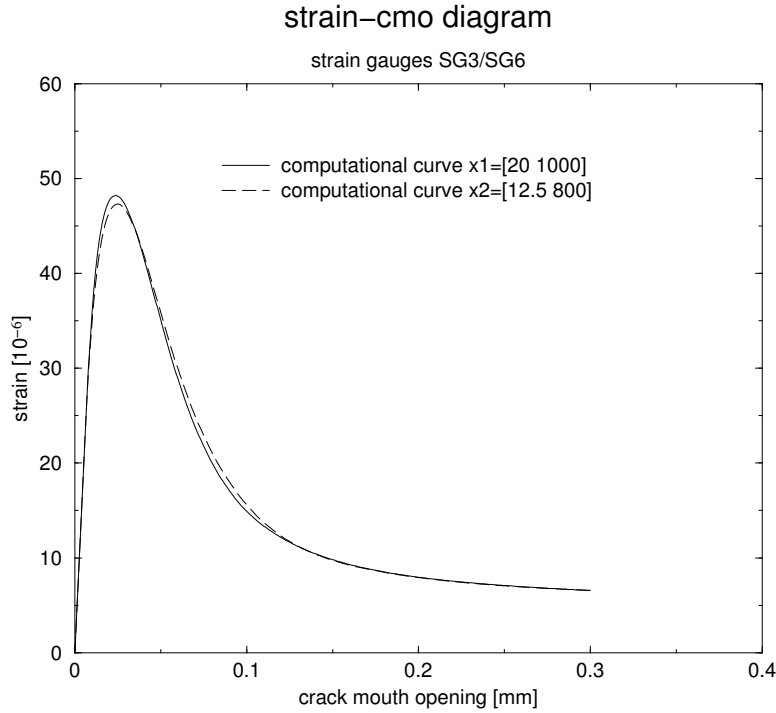


Figure 5.38: Computational strain-CMO curve corresponding to the strain gauges SG3/SG6 (see Figure 4.3) for two equivalent parameter sets $\mathbf{x}_1^T : [c = 20.0 \text{ mm}^2 \beta = 1000]$ and $\mathbf{x}_2^T : [c = 12.5 \text{ mm}^2 \beta = 800]$ for the experimental series n. 3 [32].

the macrocracks, side branches and/or bridges that can be observed during the experiments. In other words, a criterion is necessary in order to define the FPZ width d from a strain distribution.

Experimentally, the use of in-plane Electronic Speckle Pattern Interferometry (ESPI) in the experimental series no. 4 provides whole field displacements and strain distributions along the main sensitivity direction perpendicular to the notches. Hence, the FPZ width is defined as the width of the area where the strain exceeds a certain threshold value (defined relatively to the peak value). Widths of the FPZ are recorded during the entire fracture process, so that FPZ width vs. deformation curves are available for the experimental series no. 4.

Numerically, at each time step t , the nonlocal equivalent strain profile

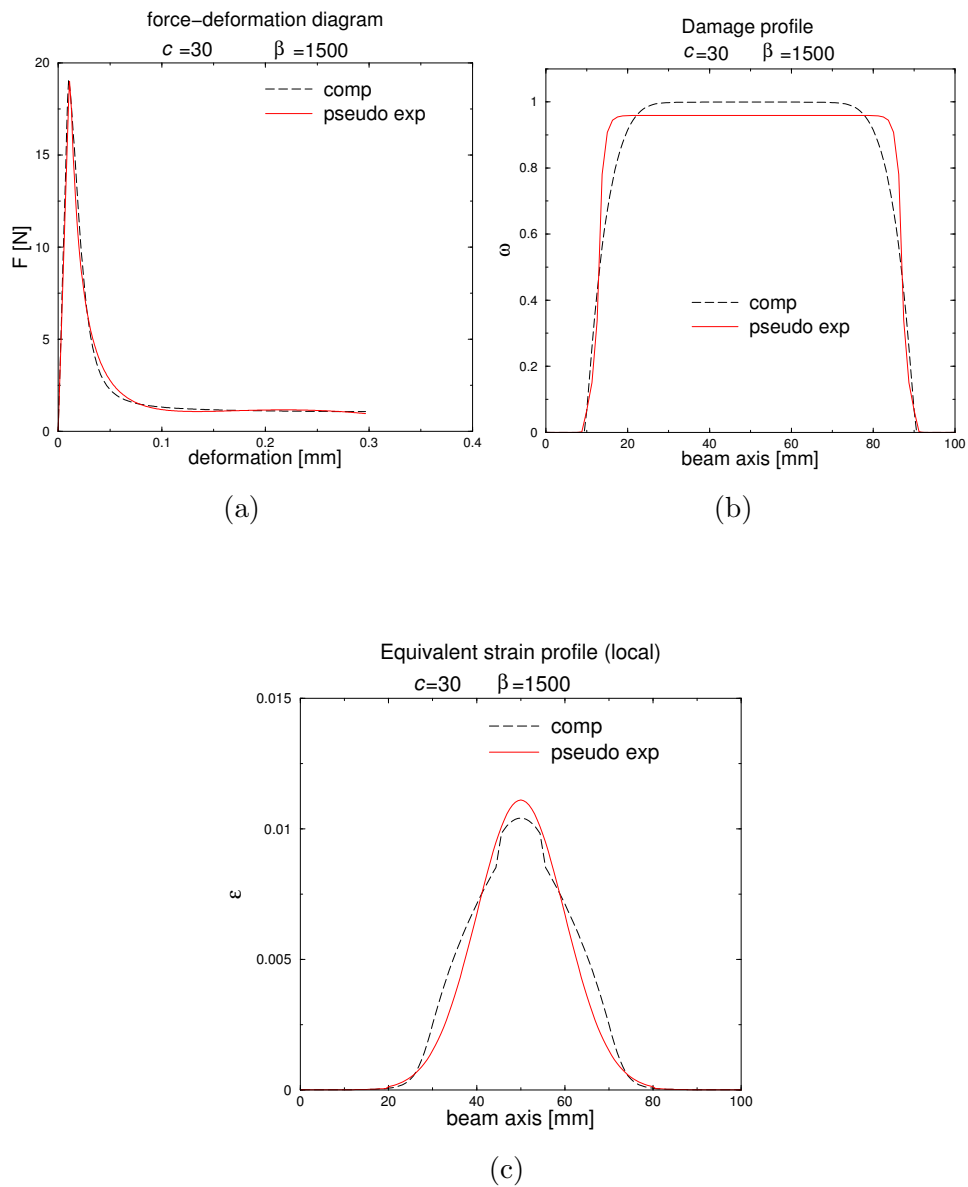


Figure 5.39: Pseudo experimental data in the one-dimensional bar case: (a) force deformation diagram (b) final damage profile along the bar (c) final equivalent strain profile along the bar.

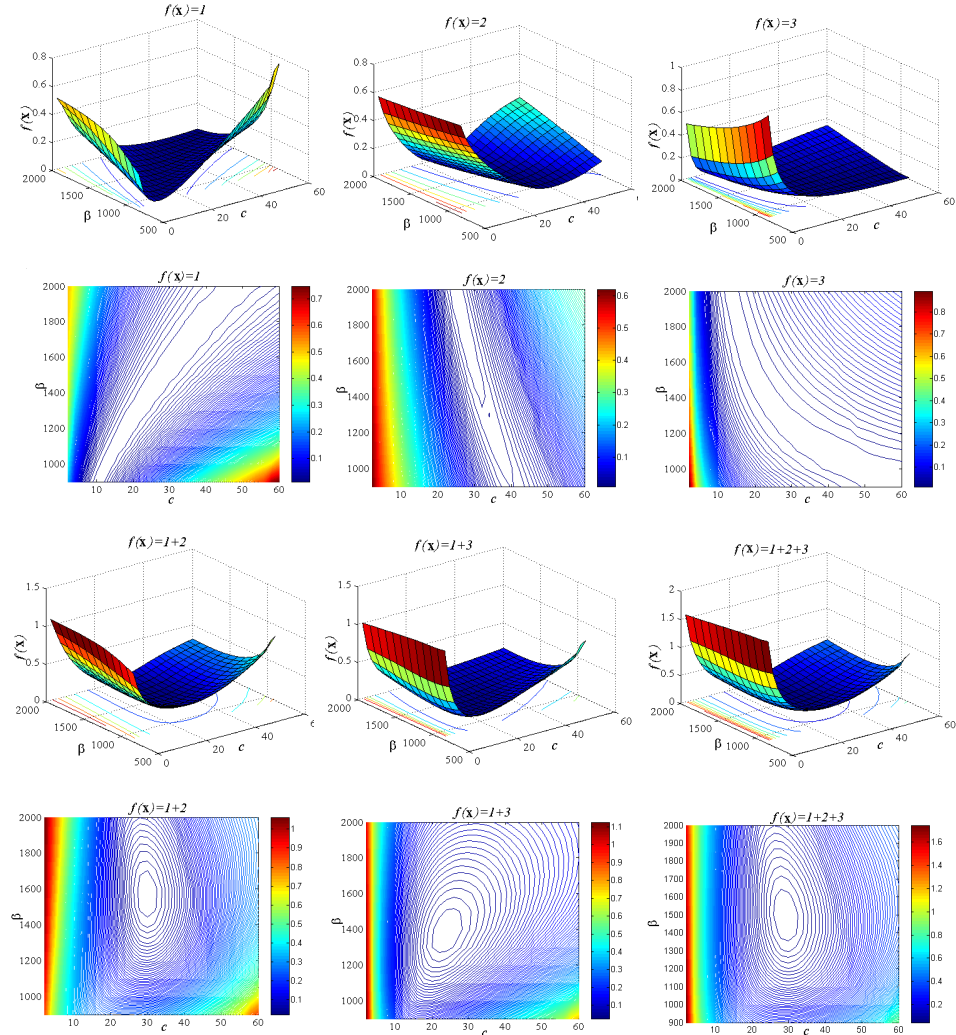


Figure 5.40: Objective function and projection in the parameters grid considering different information contribution for the one-dimensional tension bar case ($\alpha = 0.95$).

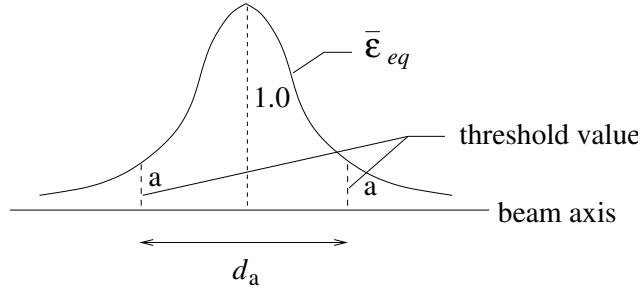


Figure 5.41: Nonlocal equivalent strain profile along the beam mid-height axis, used for the FPZ width definition d_{comp} .

along the beam mid-height axis may be considered (alternatively, the damage profile or the local equivalent strain profile might be used). Hence, analogously to the experimental case, the computational value $d_{\text{comp}}^t(\mathbf{x})$ may be defined as the width of the area where the nonlocal strain $\bar{\epsilon}_{eq}$ is larger than a certain fixed percentage (the same used during the experiments) of the peak value (see Figure 5.41).

As already mentioned in Section 4.4, it could be argued that this way of determining the FPZ width is arbitrary and debatable and that the final estimate of the model parameters vector is influenced by both the experimental technique adopted for the measurement of d_{exp} and the method and threshold value used for the definition of the numerical corresponding value d_{comp} . However, the essential aspect and requirement is that all coefficients, assumptions, and procedures used for the calibration of the numerical model are kept constant and consistent for all specimens sizes and loading conditions, so that the predictive capacity of the model may be assessed. Therefore, the strain threshold value used for the definition of the FPZ width, which should be consistent with the experimental data, may be seen as a tuning parameter of the so-calibrated model.

Hence, the width of the damaged area d may be included in the definition of the objective function $f(\mathbf{x})$, so that Eq. (3.5) may be rewritten as

$$f(\mathbf{x}) = p_1 \frac{(\mathbf{y}_{\text{exp}} - \mathbf{y}_{\text{comp}}(\mathbf{x}))^T \mathbf{C}_{\text{exp}}^{-1} (\mathbf{y}_{\text{exp}} - \mathbf{y}_{\text{comp}}(\mathbf{x}))}{\mathbf{y}_{\text{exp}}^T \mathbf{y}_{\text{exp}}} + p_2 \frac{(\mathbf{d}_{\text{exp}} - \mathbf{d}_{\text{comp}}(\mathbf{x}))^T \mathbf{C}_{\text{d-exp}}^{-1} (\mathbf{d}_{\text{exp}} - \mathbf{d}_{\text{comp}}(\mathbf{x}))}{\mathbf{d}_{\text{exp}}^T \mathbf{d}_{\text{exp}}}, \quad (5.15)$$

where \mathbf{y}_{exp} and \mathbf{y}_{comp} are represented by Eqs. (3.3) and (3.4), respectively, while \mathbf{d}_{exp} and \mathbf{d}_{comp} may be defined as

$$\mathbf{d}_{\text{exp}} = [d_{\text{exp}}^1 \quad d_{\text{exp}}^2 \quad \cdots \quad d_{\text{exp}}^{n_{yd}}]^T, \quad (5.16)$$

$$\mathbf{d}_{\text{comp}}(\mathbf{x}) = [d_{\text{comp}}^1(\mathbf{x}) \quad d_{\text{comp}}^2(\mathbf{x}) \quad \cdots \quad d_{\text{comp}}^{n_{yd}}(\mathbf{x})]^T, \quad (5.17)$$

with d^t points along the local FPZ width-deformation curve, analogously to the case of forces along the global force-deformation curve (see Figure 3.6). In Eq. (5.15) p_1 and p_2 are two weight factors with which the two contributions, global and local data, are taken into account, while $\mathbf{y}_{\text{exp}}^T \mathbf{y}_{\text{exp}}$ and $\mathbf{d}_{\text{exp}}^T \mathbf{d}_{\text{exp}}$ are two normalizing factors, necessary because of the different orders of magnitude between force and FPZ width values. The maximum value of each contribution between all parameters population \mathbf{x}_i may be used, alternatively, as normalizing factor, so that each component in Eq. (5.15) is a dimensionless number between zero and one. Normalization is also necessary if the responses of different specimen sizes are involved in the objective function, since they are characterized by rather different values of forces.

Alternatively, Eq. (3.5) may remain the same, but the two vectors \mathbf{y}_{exp} and \mathbf{y}_{comp} are redefined as

$$\mathbf{y}_{\text{exp}} = \left[\sqrt{\frac{p_1}{\mathbf{y}_{\text{exp}1}^T \mathbf{y}_{\text{exp}1}}} \mathbf{y}_{\text{exp}1}^T \quad \sqrt{\frac{p_2}{\mathbf{y}_{\text{exp}2}^T \mathbf{y}_{\text{exp}2}}} \mathbf{y}_{\text{exp}2}^T \right]^T, \quad (5.18)$$

$$\mathbf{y}_{\text{exp}1} = [F_{\text{exp}}^1 \quad \cdots \quad F_{\text{exp}}^{n_y}]^T, \quad (5.19)$$

$$\mathbf{y}_{\text{exp}2} = [d_{\text{exp}}^1 \quad \cdots \quad d_{\text{exp}}^{n_{yd}}]^T, \quad (5.20)$$

$$\mathbf{y}_{\text{comp}}(\mathbf{x}) = \left[\sqrt{\frac{p_1}{\mathbf{y}_{\text{exp}1}^T \mathbf{y}_{\text{exp}1}}} (F_{\text{comp}}^1(\mathbf{x}) \quad \cdots \quad F_{\text{comp}}^{n_y}(\mathbf{x})) \right. \\ \left. \sqrt{\frac{p_2}{\mathbf{y}_{\text{exp}2}^T \mathbf{y}_{\text{exp}2}}} (d_{\text{comp}}^1(\mathbf{x}) \quad \cdots \quad d_{\text{comp}}^{n_{yd}}(\mathbf{x})) \right]^T. \quad (5.21)$$

Equivalently, the equations of the KF procedure may remain the same considering instead of Eqs. (5.1) and (5.2) the following vectors

$$\mathbf{y}_{\text{exp}}^t = \left[\sqrt{\frac{p_1}{\mathbf{y}_{\text{exp}1}^T \mathbf{y}_{\text{exp}1}}} F_{\text{exp}}^t \quad \sqrt{\frac{p_2}{\mathbf{y}_{\text{exp}2}^T \mathbf{y}_{\text{exp}2}}} d_{\text{exp}}^t \right]^T \quad t = 1..n_y(n_{yd}), \quad (5.22)$$

$$\mathbf{y}_{\text{comp}}^t(\mathbf{x}) = \left[\sqrt{\frac{p_1}{\mathbf{y}_{\text{exp}1}^T \mathbf{y}_{\text{exp}1}}} F_{\text{comp}}^t(\mathbf{x}) \quad \sqrt{\frac{p_2}{\mathbf{y}_{\text{exp}2}^T \mathbf{y}_{\text{exp}2}}} d_{\text{comp}}^t(\mathbf{x}) \right]^T. \quad (5.23)$$

Regarding the choice of the two weights p_1 and p_2 , some comments can be made. In case of multi-objective or multi-criteria optimization problems, one of the possible approaches available in literature is to use a weighted summation of the objective functions. This approach, belonging to the ‘a priori’ methods, provides that preferences may be included by the user at the beginning of the search process. So, the user assigns subjective weights to each criterion, according to engineering intuition, knowledge and specific requirements. For instance, the user might prefer to emphasize the fitting of the global response instead of the local response or vice versa. However, two procedures can be followed that may help the user in this matter. Firstly, a study of the sensitivity of the global and local results with respect to the model parameters is suggested. If, for instance, the influence of the model parameters on the global response is stronger than that on the local response, a higher value for the corresponding weight may be selected. Hence, a parametric study of the influence of the ratio p_1 over p_2 may be carried out. A second procedure may be to assign to both weights unit values, so that the only effective weight for each experimental data is the corresponding experimental covariance for the local and global set. Consequently, experimental values characterized by significant noise (or scatter or uncertainty) are considered a less important target.

For the specimen BG1 of the experimental series n. 4, for instance, the two parameters sets $\mathbf{x}_1^T : [c = 60.0 \text{ mm}^2 \ \beta = 600]$ and $\mathbf{x}_2^T : [c = 20.0 \text{ mm}^2 \ \beta = 300]$ belong to the saddle area of the objective function defined using only the global stress-CMOD curves (see Figure 5.42a). However, the first parameter set corresponds to a better fitting of the local FPZ width-CMOD curve (see Figure 5.42b). Hence, by using the objective function definition of Eq. (5.15), with unitary weights and using a strain threshold of 20% (in Figure 5.41, $a=0.20$) of the peak values for the definition of the FPZ width (the same as used experimentally), the equivalence between the two parameters sets may be removed.

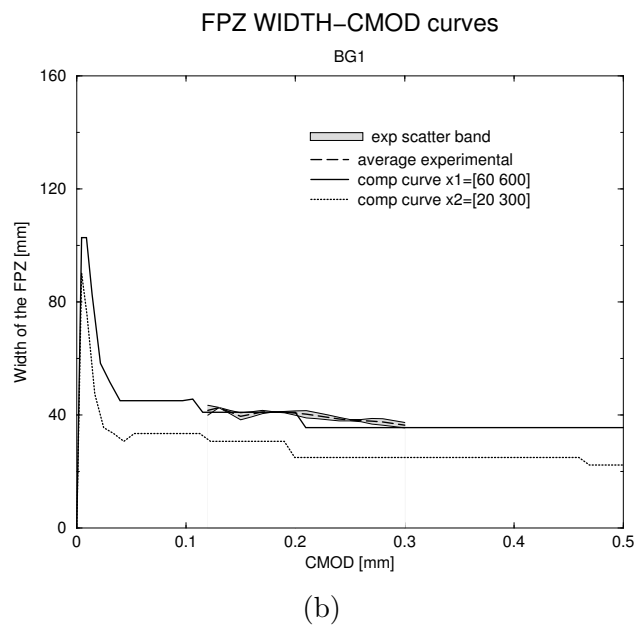
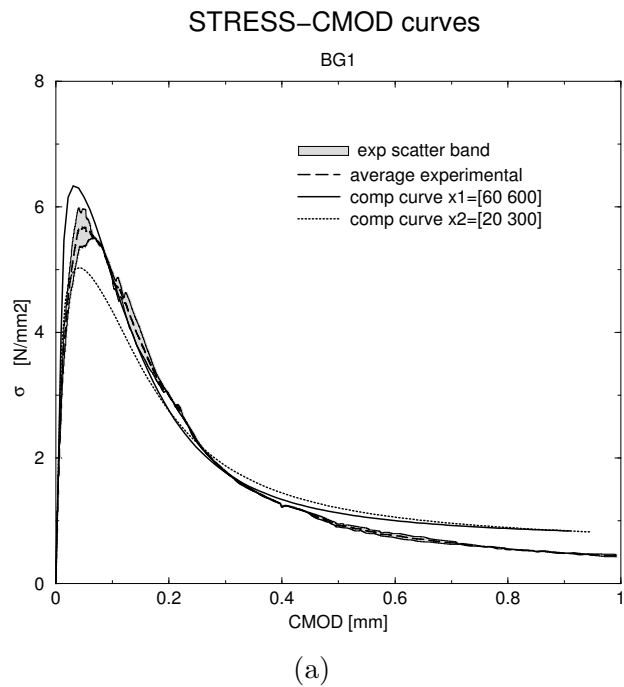


Figure 5.42: Specimen BG1 of the experimental series n. 4 [42, 43]: (a) stress-CMOD curves and (b) FPZ width-CMOD curves corresponding to two parameter sets that belong to the saddle area of the objective function, if only global information is used ($\alpha = 0.92$).

However, the influence of structural factors (such as the specimen size, the specimen geometry, load and boundary conditions) on the width of the damaged area d_{exp} can not be completely ignored as well as on the global force-deformation response of the specimen. Hence, parameter identification procedures based on the global and local curve of one single specimen size, do not guarantee a satisfactory prediction of the peak loads and global curves of other specimen sizes, as already discussed in the previous Sections. Hence, a wide range of experimental global and local data is required, for reliable model calibration that can be used for prediction purposes.

5.6.2 Global and local curves of different sizes

In this case the inverse problem is well-posed and an *average, stable* fitting of the size effect curve and of all global force-deformation curves may be obtained. However, a rigorous fitting of all sizes is not achieved when only a single model parameter set is used.

Hence, if only global data or only local data of *all specimen sizes* of the experimental series n. 4. are used in Eq. (5.15), the objective function remains characterized by a saddle (see Figure 5.43a and b). Considering both the global and local contribution, with unit weights ($p_1 = p_2 = 1.0$), a single stable solution may be identified (see Figure 5.43c). Reducing the local data weight p_2 , the area of possible solutions enlarges (see Figure 5.43d).

The optimum solution $\mathbf{x}_1^T : [c = 80 \ \beta = 600]$ (see Figure 5.43c) represents an *average compromise* solution between global and local data ($p_1 = 1.0$ and $p_2 = 1.0$) of all specimen sizes, as shown in Figures 5.44 and 5.45 (the experimental local curve for the largest size is not available).

In Figures 5.44 and 5.45 also the curves related to two other parameter sets $\mathbf{x}_2^T : [c = 60 \ \beta = 600]$ and $\mathbf{x}_3^T : [c = 25 \ \beta = 350]$ are shown for a comparison. The two parameter sets are *unstable* solutions in case of $p_1 = 1.0$, $p_2 = 0.2$ and $p_1 = 1.0$, $p_2 = 0.0$, respectively. Of course, the best average fitting of only global data of all sizes is obtained in case of \mathbf{x}_3 (see also Figure 5.29), while, although local data are involved, global data fitting is considered more relevant in the case of \mathbf{x}_2 . In other words, between the three parameter sets, \mathbf{x}_3 corresponds to the best global curves and the worst local curves fitting, \mathbf{x}_1 vice versa, since the two type of data fitting are equally taken into account, and \mathbf{x}_2 presents curves in between the ones related to \mathbf{x}_1 and \mathbf{x}_3 . Hence, in this case, if a smaller threshold value (for instance 5% of the peak value) for the FPZ definition is considered, the local curves corresponding to the parameter set \mathbf{x}_3 move towards upper width values. Consequently, this

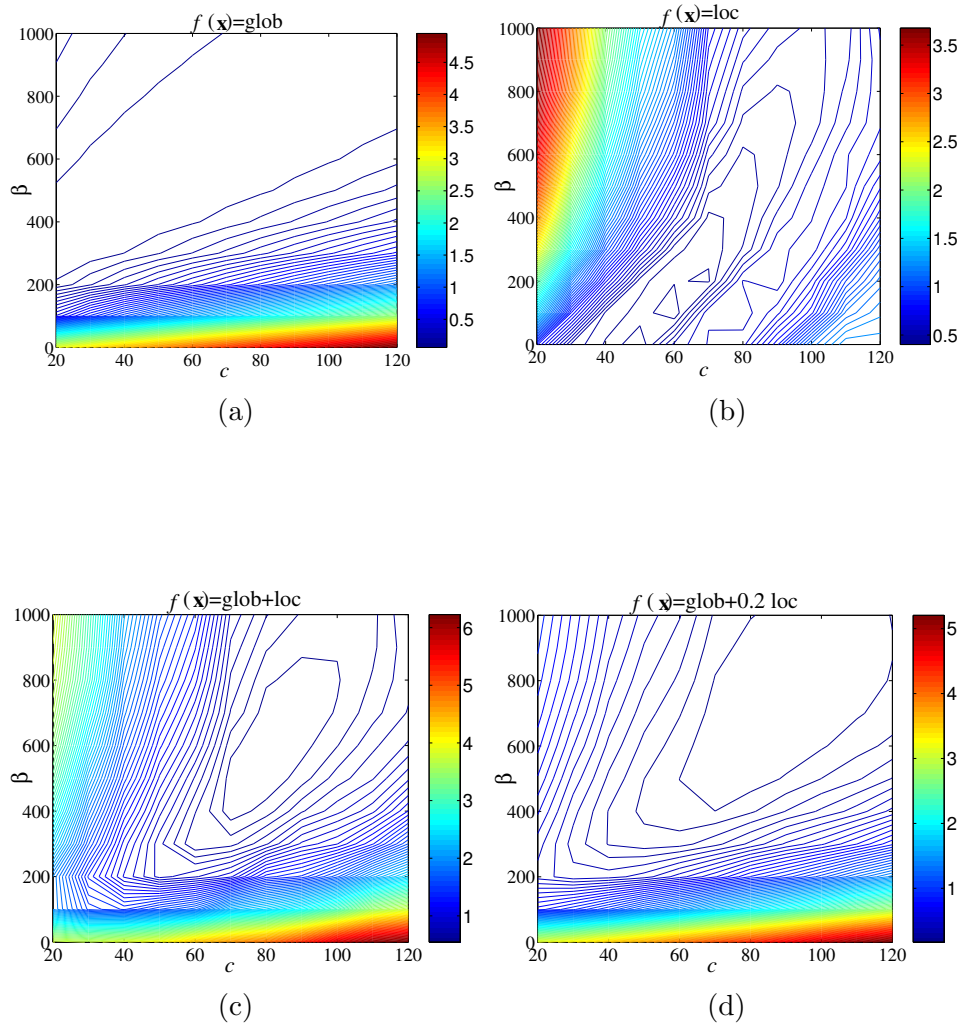


Figure 5.43: Contourplot of the objective function $f(\mathbf{x})$ of Eq. (5.15) considering all BG specimen sizes of the experimental series n. 4 [42, 43] and involving (a) only the global data (b) only the local data (c) global and local data with $p_1 = 1.0$ and $p_2 = 1.0$ (d) global and local data with $p_1 = 1.0$ and $p_2 = 0.2$ ($\alpha = 0.92$).

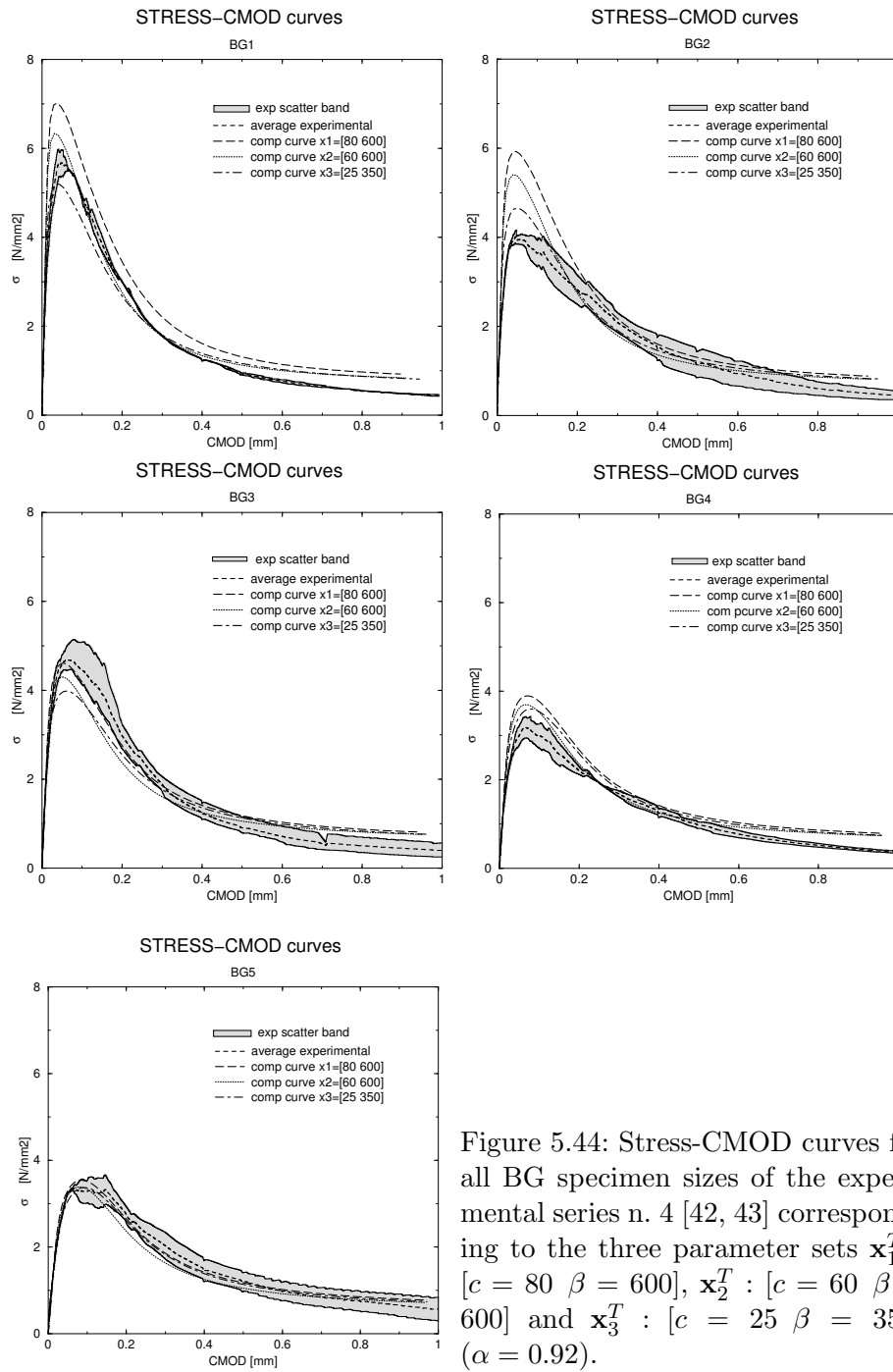


Figure 5.44: Stress-CMOD curves for all BG specimen sizes of the experimental series n. 4 [42, 43] corresponding to the three parameter sets $\mathbf{x}_1^T : [c = 80 \ \beta = 600]$, $\mathbf{x}_2^T : [c = 60 \ \beta = 600]$ and $\mathbf{x}_3^T : [c = 25 \ \beta = 350]$ ($\alpha = 0.92$).

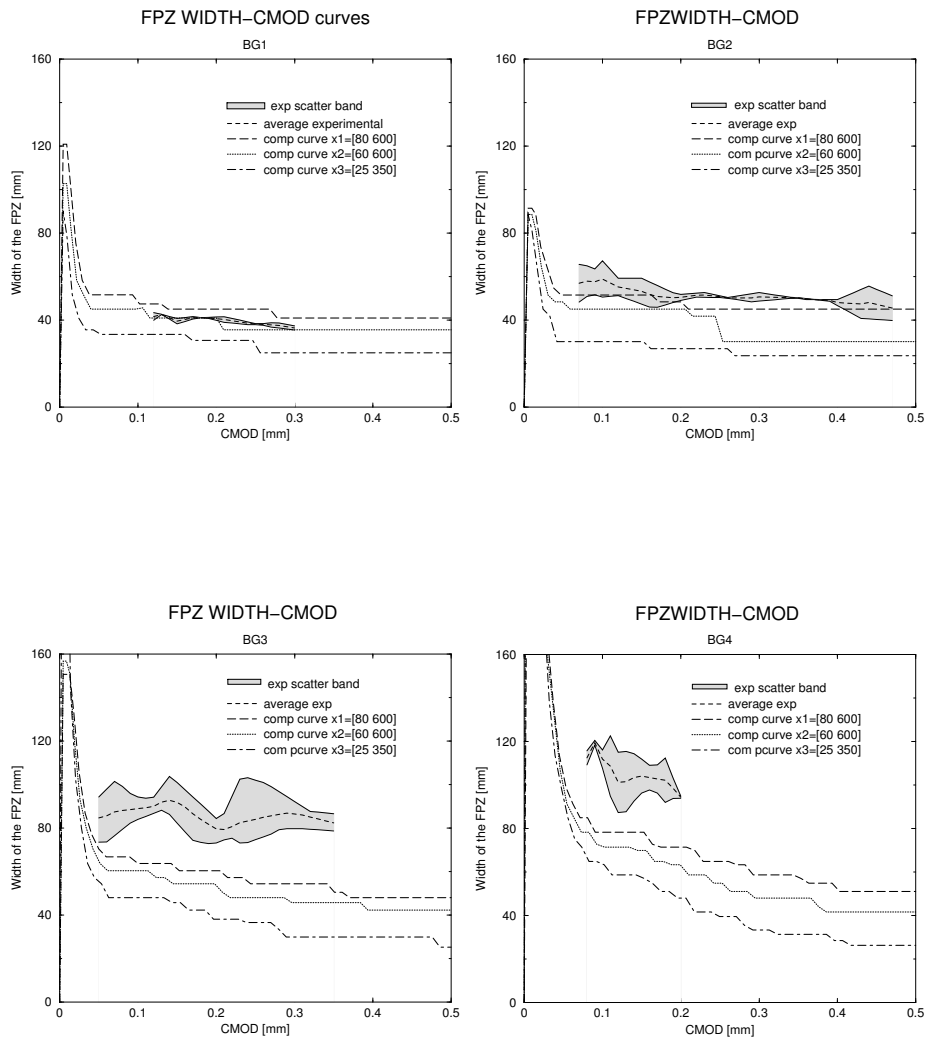


Figure 5.45: FPZ width-CMOD curves for all BG specimen sizes of the experimental series n. 4 [42, 43] corresponding to the three parameter sets $\mathbf{x}_1^T : [c = 80 \ \beta = 600]$, $\mathbf{x}_2^T : [c = 60 \ \beta = 600]$ and $\mathbf{x}_3^T : [c = 25 \ \beta = 350]$ ($\alpha = 0.92$).

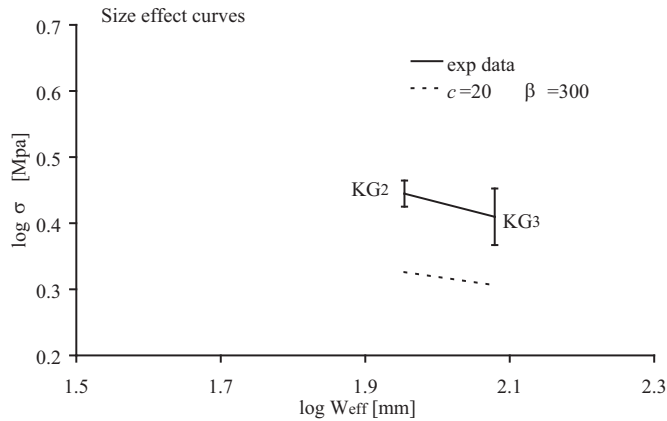


Figure 5.46: Experimental and computational size effect curves corresponding to $\mathbf{x}_1^T : [c = 20 \ \beta = 300]$ for double-edge notched tensile specimens (KG2 and KG3 sizes) of the experimental series n. 4 [42, 43] ($\alpha = 0.92$).

would lead to a better fitting of local and global data.

Nevertheless, even with a decreased threshold for the FPZ width definition, considering a single parameter set for all specimen sizes, a computational range of variation for the FPZ width is produced (with regards to the specimen size) that is smaller than the experimental one (see Figure 5.45). Hence, not only the size effect on the peak loads, but also the size effect on the FPZ width is badly captured by the adopted model, with a single parameter set.

5.6.3 Global and local curves of different sizes and different structures

This represents the most complete experimental range of data that can be involved for the validation of a numerical model. However, also in this case, the predictions of the model using only a single parameter set, may be unsatisfactory, as shown in Figure 5.46 for the case of the double-edge notched tensile tests of the experimental series n. 4. Using a parameter set that provides an acceptable average fitting of the bending tests (see Figure 5.27) does not correspond to reliable model predictions for the tensile tests ([67], [85]). Structural effects on the length scale parameter are encountered.

Chapter 6

Parameter identification strategy

This Chapter is intended to summarize the inverse strategy proposed for parameter identification problems of computational models for localized failure. Although, in the present work, the strategy has been developed and applied for the parameter identification of the gradient-enhanced continuum damage model, it remains valid for other computational regularized continuum models, because of the generality and the simplicity of implementation of the inverse methods (see Sections 3.4 and 5.2). The considered inverse techniques (K-Nearest Neighbors and Kalman filter) may be used to solve parameter identification problems also in the case of numerical models which follow the discrete approach. In this case, however, the local data that might be needed in the parameter estimation problem should be related to other quantities different than the width of the fracture process zone.

Moreover, as already discussed in Section 5.1, the parameter identification problem presented in this thesis mainly focuses on the gradient parameter c (or equivalently on the length scale parameter l) and on the slope of the softening branch of the constitutive law represented by the parameter β (see Figure 2.1).

6.1 Parameter identification procedure

Two inverse techniques are used in a serial fashion in the proposed parameter identification strategy: the K-Nearest Neighbors method (KNN) and the Kalman filter (KF) method (see Section 3.4).

The first technique allows a preliminary study of the parameters space, so that possible ill-posedness of the inverse problem and promising searching regions may be easily detected. In Section 5.4.1, in fact, a correlation between the gradient parameter c and the slope of the softening branch of the constitutive law β is shown using the KNN method. A preliminary investigation of the promising searching regions may speed up the convergence of the identification process, starting from an optimal choice of the initial guess of the model parameters. Moreover, this preliminary study may detect local minima of the objective function. Hence, it may be possible to avoid that the inverse procedure, sticking into a local minimum, provides model parameter estimates that are not correct and that are influenced by the initial guess, as starting point of the searching process belonging to the attraction basin of the local minimum. Using only the global force-deformation curves (even for different specimen sizes) leads to an ill-posed inverse problem (lack of uniqueness and/or stability of the inverse solution). For this reason, examination of local data (widths of the damaged area during the fracture process) is also provided by the inverse strategy scheme (see Sections 5.4, 5.5 and 5.6). Moreover, the adopted computational model reveals limits in reproducing all the complex mechanisms that result in the size effect phenomenon, using a single parameters set for all specimen sizes (see Section 5.5). Hence, the possibility of identifying a size dependent length scale parameter is also envisaged in the procedure. The KF method represents the refining final searching tool, which takes into account also the uncertainties related to both the experimental data and to the parameters estimate (see Section 5.3).

The strategy is composed of five steps, representing each step a checking point of the data fitting or a changing point of the procedure itself.

Step ①

Hence, the first step of the strategy, developed in this thesis, consists of the identification of the initial guess \mathbf{x}_0 by means of the KNN method. For this purpose, a parameters grid $\beta - c$ may be selected and a number of forward analyses may be carried out for each $\beta - c$ couple of the considered parameters population (see Section 3.4.1). If the identification procedure is based on global and local experimental curves of different specimen sizes, as suggested in Chapter 5, the following objective function needs to be computed for each point of the parameters grid (as in the case reported in Section 5.6.2):

$$\sum_{j=1}^n p_1 f_{1_sizej} + \sum_{j=1}^n p_2 f_{2_sizej}, \quad (6.1)$$

where f_{1_sizej} and f_{2_sizej} are the global and local contribution, respectively, related to the specimen size j (i.e. first and second component of Eq. (5.15)). Hence, for each specimen size, two matrices with the global and local contributions may be built, being each element of the matrix related to one couple of the parameters grid. Of course, f_{1_sizej} and f_{2_sizej} represent the normalized value of these matrices (for instance, as already mentioned in Section 5.6.1.3, dividing each element by the maximum value of the matrix). Regarding the choice of the two weights p_1 and p_2 the reader is referred to Section 5.6.1.3.

Step ② and Step ③

In these two steps a comparison between the experimental and computational curves (corresponding to \mathbf{x}_0), of all specimen sizes, is performed. First regarding the global data (Step ②) and, subsequently, regarding the local data (Step ③a and ③b), as shown in Figure 6.1. However, as already discussed in Sections 5.4.2, 5.5 and 5.6.2, only an average fitting through all specimen sizes can be obtained using a single parameters set. Hence, the experimental-computational comparison basically results in one of the following cases: i) both the global and local data fitting is acceptable ii) the average fitting of one of the two types of data is not acceptable iii) the fitting of both the global and local data is not satisfactory.

Step ④ and Step ⑤

The phases subsequent to the three cases presented above are presented here. In the first case, the preliminary study may be ended and the searching process may be refined using the KF method. The global and local data of all sizes are exploited in the KF method for the unique parameters set estimate (Step ④aa in Figure 6.1).

In the second case (Step ④ab or Step ④ba in Figure 6.1), the ratio between the two weights p_1/p_2 or the nonlocal equivalent strain threshold for the FPZ definition might be modified (see, for instance, the case discussed in Section 5.6.2 and shown in Figures 5.44 and 5.45). Hence, the procedure is restarted from Step ①.

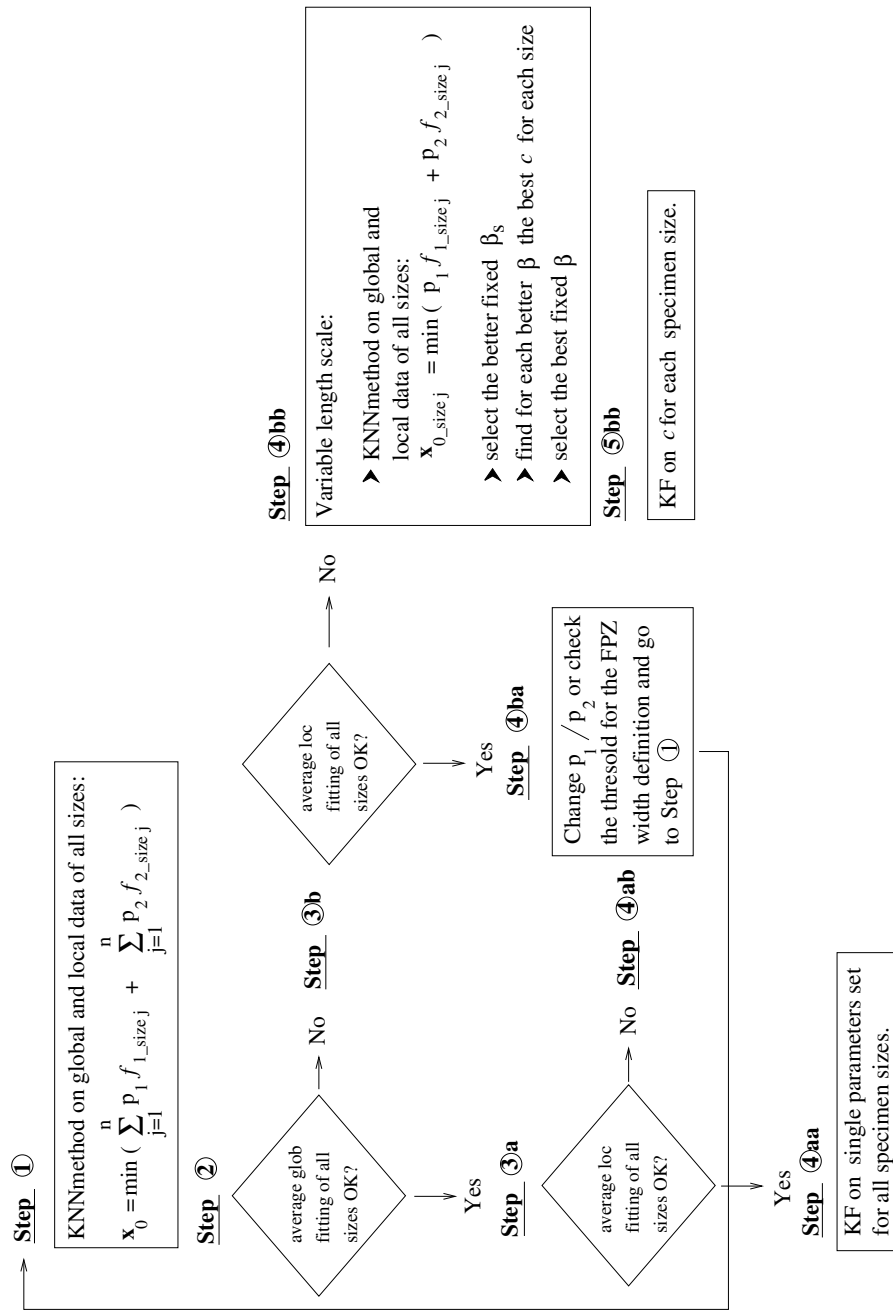


Figure 6.1: Inverse strategy scheme.

Finally, in the third case, a better rigorous fitting of the global and local size effect might be obtained considering, for instance, the following sub-procedure (Step ④bb) (see Figures 5.33 and 5.34):

identify the best parameters set estimate for each specimen size corresponding to the minimum of the following objective functions (see Figure 6.2)

$$p_1 f_{1_sizej} + p_2 f_{2_sizej} \quad (6.2)$$

identify the better fixed β s (i.e. the better representatives β s of the best sets population) (see Figure 6.2)

identify, for each better β , the best c for each specimen size (see Figure 6.3)

compare the experimental and numerical curves (global and local) and select the best ‘fixed β ’ row.

Note that the above suggested ‘sub-procedure’, does not require additional computational analyses, since the various contributions f_{1_sizej} and f_{2_sizej} for the different sizes have already been calculated in Step①. The various steps of the ‘sub-procedure’ can be performed by simply examining the matrices built using f_{1_sizej} and f_{2_sizej} of the different sizes.

Also in the third case, the searching process may be refined performing different KF methods only on the length scale parameter for each specimen size (using global and local data) (Step ⑤bb).

The unsatisfactory fitting of the experimental size effect curve provided by the examined model, with a fixed value of the length scale parameter, might be the consequence of different phenomena. Firstly, as already cited in Section 5.5, the considered numerical model is deterministic. Hence statistical influences in the size effect curve can not be reproduced by the model. Moreover, the length scale parameter might depend not only on the initial undamaged microstructure, but also on all deformation mechanisms occurring during the damage process. These mechanisms change the microstructure in a progressive way. In other words, the length scale might not be constant during the entire fracture process, but it could be variable according a suitable evolution law, for instance, in terms of cracking strain or damage variable, in a sort of self-adaptive strategy implemented at the level of the material

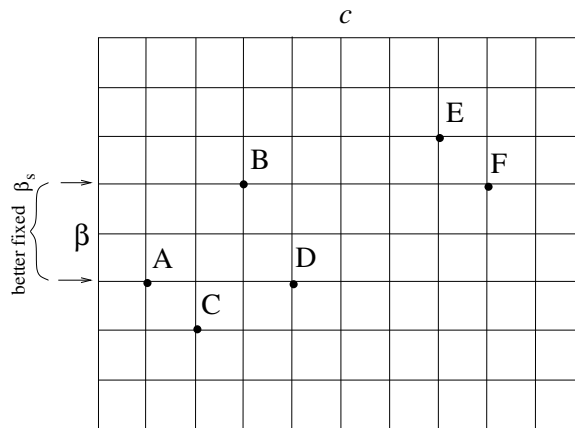


Figure 6.2: Step ④bb: example of identification of the best parameters set for each specimen size (A to F) in the parameters grid and selection of the better fixed β_s .

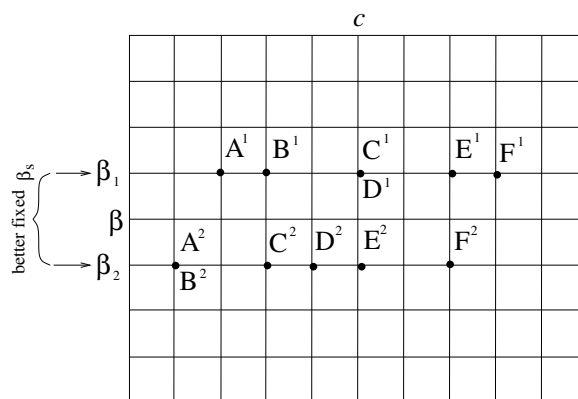


Figure 6.3: Step ④bb: example of identification of the best c for each specimen size (A to F) for each better fixed β in the parameters grid.

constitutive law [38], [85]-[68]. Finally, the fact that the numerical size effect curve remains too flat compared to the experimental one might be the consequence of a series of different possible sources of error, already cited in Section 3.3. These errors are intrinsic deficiencies of the ‘S’ or of the ‘M’ box (see Figure 3.2) and not all easily detectable and corrected.

On the other hand, considering the possibility of a length scale that depends on the specimen size or on the fracture process state, not only invalidates the model assumption of constant material properties, but it also makes the inverse procedure for parameter identification more complex (a length scale function should be identified). Moreover, in this way, the use of the model for prediction purposes would be limited. In fact, the model calibrated on the basis of the experimental results of a certain specimen size or loading condition might provide unreliable predictions for other specimen sizes and loading conditions. Hence, the hypothesis of a variable length scale is debatable and not easily accepted in the fracture mechanics research community.

Alternative possibilities require a step back: a deeper model analysis, since the inverse problem has highlighted some limitations. As consequence, a different and maybe more complex model might be needed. For instance, a model that includes statistical aspects of the size effect phenomenon or more mechanisms of the fracture process phases or with more parameters for describing the complex material microstructure. Alternatively, different modelling approaches (i.e. not only the continuum approach) for the different phases of the fracture process might be considered. Hence, for instance, the continuum approach might be used to model the pre-peak micro cracking regime, while the discrete approach might be used to model the post-peak macro cracking regime, as proposed in [85]. In any case, the model weakness may be minimized if the model contains parameters which have a determined and clear physical or mechanical meaning. In this regard, more defined physical argumentation for the length scale definition, might help in the identification process of this parameter. Also the possibility of coupling multiscale analyses with inverse analysis should be investigated. For instance, information resulting from analyses performed at the meso/microscale might be used to solve the ill-posedness at the macroscale level. Alternatively, parameter identification procedures solved at the macroscale might provide information for analyses on a lower scale. However, for simultaneous parameter identifications at different scales directly from experimental data, also measurements on different scales should be available.

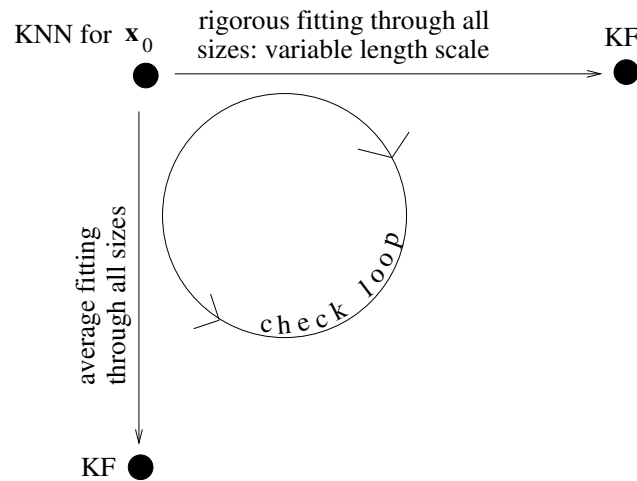


Figure 6.4: Schematic representation of the inverse strategy.

In conclusion, the entire inverse strategy may be schematically seen as composed of an initial starting analysis (KNN method on all sizes) and one check loop with two tangential directions depending on whether the average fitting for all specimen sizes is considered acceptable or not (see Figure 6.4). In the first case a single model parameters set is selected for the description of the local and global size effect (i.e. the FPZ width-deformation curves and the force-deformation curves of all specimen sizes). Errors in the model predictions are considered small for the specific purposes for which the model needs to be used. In the second case, the required rigorous fitting through the different sizes can be achieved only using a size dependent length scale parameter, which is not an acceptable solution. In both cases, the search process ends with a refined parameters estimate, obtained through the KF method.

Chapter 7

Extension to other material models for localized failure

Although numerically elaborated and applied to the parameter identification of the gradient enhanced continuum damage model, the inverse strategy and/or the tools developed in this thesis are also valid for other types of models for the description of localized failure, whether in tension or in compression [83]. Particularly, in case of tensile fracture in quasi-brittle materials (e.g. concrete), the procedures hold either in case the model follows the continuum approach or in case it follows the discrete approach (see Section 2.1). Moreover, some examined issues, for instance, related to the well-posedness of the inverse problem or to the factors that may have an influence on the final parameter estimates, remain crucial points that can not be neglected when solving the parameter identification problem for other models.

The KNN method and the Kalman filter method, are general, flexible and they may be simply implemented as a shell around various finite element codes. An example of application of the KF method for the parameter identification of a cohesive crack model may be found in [17]. Hence, also in case of models following the discrete approach the implementation scheme of the inverse methods, shown in Figure 5.3, remains valid. The vector \mathbf{y}_{comp} may contain information on the force-deformation response of the specimen. Hence, the KNN method may be used as a preliminary study of the parameters space and the objective function and the KF method may subsequently refine the search process. From the implementation point of view, also in this case, the main difficulties consist of creating the continuous interaction and exchange of information between the FE code and the KF code, such that

all iterations of the inverse method can be automatically executed, one after another. For this purpose, the FE code should automatically stop after a definite number of forward analyses, pass the required output to the KF code, update the recorded model parameters value and re-initialize the forward problem for the next KF step. Hence, it is necessary to know where and how all the involved variables are stored in the adopted FE program and how and when they are possibly exchanged between the different subroutines of the FE code.

7.1 Higher order continuum models

Regarding the continuum approach for softening and localization phenomena, different enriched models have been proposed, which are regularized through the introduction of higher-order spatial or time derivative terms in the description of the material (e.g. viscoplastic model [65], Cosserat model [64], nonlocal continuum model [10, 72] and the examined gradient-enhanced continuum damage model (see Section 2.3.1)). Also, for this class of models, containing a length scale parameter, uniqueness and/or stability problems might be encountered in the solution of the parameter identification procedure if only force-displacement curves are involved. Hence, in this case, not only the inverse techniques represented by the KNN and KF methods may be used, but also the inverse strategy, proposed in Chapter 6 and related to the use of both local and global data, may be adapted, since it depends on the specific model parameter set to be determined.

7.2 Discrete crack models

A possible future extension of the present work might focus on the parameter identification problem of discrete numerical models [92]. The investigation of the type of experimental data which are necessary and sufficient for the particular case of discrete modelling is needed for the well-posedness of the inverse problem. Since a crack in a discrete model is confined to a line, no width of the FPZ is available for this class of models and a comparison between experimental local data and computational local data is not possible. However, the crack length might be used, if necessary, to solve the ill-posedness of the inverse problem. Because no width of the FPZ is involved, the inverse problem seems to be better conditioned. Hence, the inverse strategy, presented in Chapter 6, might be slightly modified, in the sense of data type

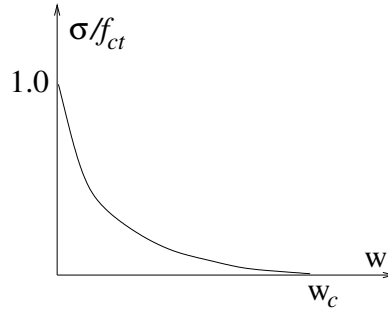


Figure 7.1: Hordijk stress-crack opening relation [44].

and data handling sequences, although the KNN and KF methods remain valid. In this way, also for this approach of modeling localized failure, possible deficiencies of the model might be highlighted and possible limits in its applicability might be established.

7.3 Smearred crack model

Finally, a fracture energy based approach [7] may be followed to overcome mesh dependency of the numerical results. In this case, the fracture energy (as material parameter) is related to the size of the finite element (i.e. a localization limiter or a length scale is introduced) and strain localization always occurs in one element. Within this framework, an indicative example is represented by the smeared crack model obtained by translating the Hordijk stress-crack opening law [44] into a stress-strain relation. The Hordijk relation for a fictitious crack, illustrated in Figure 7.1, is defined by the following relation

$$\frac{\sigma}{f_{ct}} = \left\{ 1 + \left(c_1 \frac{w}{w_c} \right)^3 \right\} \exp\left(-c_2 \frac{w}{w_c}\right) - \frac{w}{w_c} (1 + c_1^3) \exp(-c_2), \quad (7.1)$$

where c_1 , c_2 and w_c (critical crack opening corresponding to zero stress) are material parameters. The integration $G_f = \int \sigma dw$ gives for Eq. (7.1) the following expression of fracture energy

$$G_f = f_{ct} w_c \left\{ \frac{1}{c_2} \left[1 + 6 \left(\frac{c_1}{c_2} \right)^3 \right] - \left[\frac{1}{c_2} + c_1^3 \left(\frac{1}{c_2} + \frac{3}{c_2^2} + \frac{6}{c_2^3} + \frac{6}{c_2^4} \right) + \frac{1}{2} (1 + c_1^3) \right] \exp(-c_2) \right\} \quad (7.2)$$

In the smeared crack model, the strain is computed by distributing the crack opening w over a crack band length, which represents a localization limiter being dependent on element size.

For this model, the KNN method is applied, using the test results of the concrete dog-bone shaped specimen Type B of the experimental series n. 2 (see Figure 4.2) [87, 88]. The approximation of the objective function of Eq. (5.11) is built starting from forward analyses with parameter sets corresponding to a grid of the fracture energy parameter G_f and the parameter c_1 of Eq. (7.1) [27]. Increasing c_1 in the stress-crack opening law, given in Eq. (7.1) and shown in Figure 7.1, leads to an increase of the ductility. This trend is opposite to that related to the parameter β of Eq. (2.9), since an increment of β corresponds to less ductile stress-strain law (see Figure 2.1b).

The projection of the objective function $f(\mathbf{x})$ on the parameters grid, shown in Figure 7.2, suggests that, also for this model, using only global data in the parameter identification problem might result into a non-unique and/or unstable solution. However, in this case, the involvement of local data to solve the ill-posedness of the inverse problem would be meaningless, since the numerical strain profile in the cracked zone does not have a physical interpretation. The profile is dependent on element size, because strain localization takes place in the smallest possible zone. Therefore, a link between numerical and experimental local data is meaningless. Hence, this indicates the importance of a computational model in providing not only a correct reproduction of the force-displacement curve, but also a correct physical description of the fractured area.

7.4 Coupling data of different models

Finally, the proposed strategy and/or tools may be applied not only in order to obtain quantitatively correct results from numerical models, but also in order to convert parameter values passing from one model to another. In fact, while in the first case the target solution is represented by experimental (real)

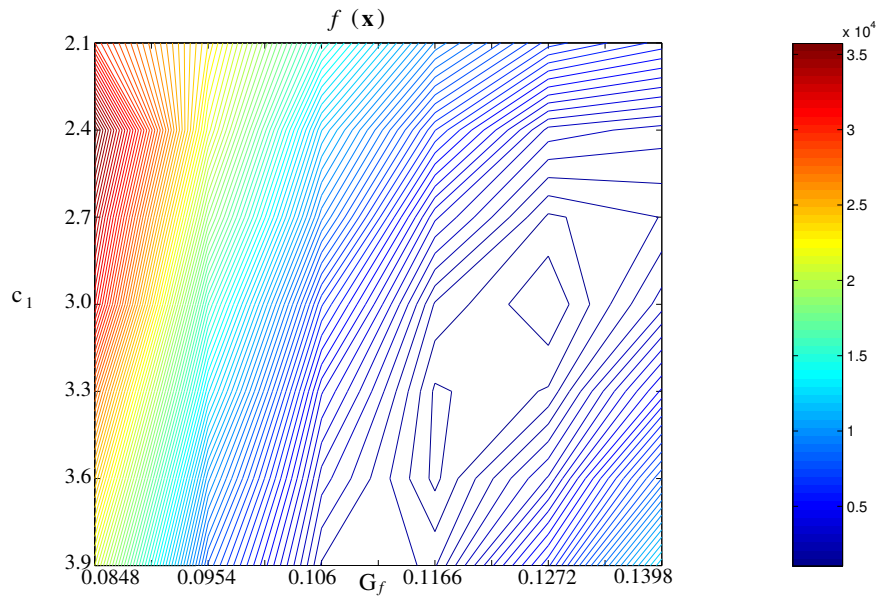


Figure 7.2: Contourplot of the KNN objective function $f(\mathbf{x})$ for the smeared crack model, using only global data of the concrete dog-bone shaped specimen Type B of the experimental series n. 2 [87, 88].

results, in the second case it is represented by the computational output of one of the two models.

However, in all cases examined in this Chapter, the most important issue remains the definition of a well-posed parameter identification problem for the given model(s). In other words, for every model, it is crucial to choose the experimental data needed for a unique and stable parameters solution.

Chapter 8

Conclusions and recommendations

Numerical models for the tensile behaviour of quasi-brittle materials may correctly describe localized failure phenomena only if all model parameters are correctly estimated. For this purpose, the development of inverse procedures is needed, since not all parameters may be directly measured during laboratory tests. This is the main aim of the present research, focusing, as an example, on the parameter identification of the gradient-enhanced continuum damage model. Particularly, the estimate of the length scale parameter and the slope of the softening branch of the stress-strain constitutive law are chosen to be the main unknowns of the analysed inverse problem. Conclusions, achievements, open issues, future outlook, other domains of applicability and recommendations, resulting from the study of the various issues related to both the *forward* and the *inverse problem*, are reported in this Chapter.

8.1 Conclusions and achievements of the research

An inverse strategy for parameter identification of numerical models for localised failure in quasi-brittle material is developed in the present work. The strategy is based on the aim of extracting intrinsic material properties (constitutive parameters at the material point level in the computational continuum approach) from measured experimental responses (representing sometimes a combination of structural and material behaviour). Hence, a link between advanced computational and experimental techniques is established.

The final parameters estimate can be influenced by the initial guess of the

model parameters (representing the starting point of the search process), by the associated covariance (representing the uncertainty on the initial guess) and by the scatter distribution of the experimental data (see Section 5.4.1). Hence, the KNN method, for the preliminary study of the parameters space and the possible iterative use of the KF procedure are proposed as remedies to the nonlinearity and, as consequence, to the non-guaranteed convexity of the inverse problem. A good quality of experimental data and a possible cut-off of the tail of the load-deformation curves may avoid or limit problems caused by the experimental covariance.

The well-posedness (in terms of uniqueness and/or stability of the solution) of the inverse problem is investigated, providing an insight in the problem of selecting the type of experimental data to be used in the solution of the identification problem. In fact, considering only the global force-displacement curve of one single specimen size, a correlation between the gradient parameter c (related to the length scale parameter) and the slope of the softening branch of the stress-strain constitutive law β is obtained (see Section 5.4.1). Hence, different parameter sets are equivalent in terms of global response and the inverse problem appears to be ill-posed.

Involving the force-deformation curves of different specimen sizes in the solution of the identification problem does not solve the ill-posedness, since the direction of correlation between the two parameters is similar for the various specimen sizes (see Section 5.4.2).

Considering additional deformation measurements in points located in the neighborhood of the macrocrack in the parameter estimation problem does not provide satisfactory additional criteria for the selection of a stable and unique solution. In fact, the results indicate that parameter sets, equivalent in terms of global response, correspond also to a similar development of strains in points that are outside the area where damage occurs and strains localize. Instead, for points within that area no comparison between the numerical and the experimental deformation is possible, since limited values in the case of the real discrete crack correspond to high numerical values in the computational continuum smeared approach (see Section 5.6.1.1).

However, if local data, as the development of the width of the fracture process zone during the fracture process, are involved in the identification problem, the well-posedness may be recovered and a unique and stable solution may be obtained (see Section 5.6.1.3).

A study of the limits of validity and of the predictive capacity of the calibrated model is also carried out, analysing possible structural influences

on the parameters estimate, as a consequence of the structural effects on the experimental data used in the identification process. For this purpose experimental results related to specimens of different sizes, geometries and loading conditions are considered (see Sections 4.2 and 4.4).

The analysed model seems to incorrectly reproduce the entire experimental size effect curve using only one parameter set for all specimen sizes. It leaves the computational size effect curve, as a whole, too flat compared to the experimental one. The model reveals limits in reproducing experimental tests characterized by a certain statistical size effect. Using a single parameters set for all specimen sizes, the real size effect curve may be fitted only in an average way (see Section 5.5).

In addition, a single parameters estimate that provides an acceptable fitting of the entire force-deformation curves of a few specimen sizes does not necessarily correspond to a correct prediction of the peak loads. Hence, not only the best parameter estimates are different for the various sizes, but they also appear to be different depending on whether only the peak load or the entire force-deformation curve is involved in the inverse problem (see Section 5.5).

Moreover, considering a single parameter set for all specimen sizes, a computational range of variation for the FPZ width is produced (a different FPZ width for a different specimen size) that is smaller than the experimental one (see Section 5.6.2). Hence, not only the size effect on the peak loads, but also the size effect on the FPZ width is badly captured by the adopted model, with a single parameter set for all sizes.

If different sizes and different structures (three point bending tests and uniaxial tensile tests) are considered, unsatisfactory predictions of the model are obtained, using only one single parameter set. In other words, using a parameter set that provides an acceptable average fitting for the bending tests does not correspond to reliable model predictions for the tensile tests (see Section 5.6.3).

In conclusion, solving the inverse problem turns out to be a valid tool for the model assessment and the analysis of weak points in the description of the forward problem.

8.2 Open issues and future outlook

The issue of a length scale as a parameter with a physical meaning or as a computational remedy to the loss of ellipticity of the model equations remains

controversial.

Moreover, the possibility of a length scale parameter that depends on the specimen size, on the loading conditions or on the fracture process state might be one of the causes or the effects of erroneous modelling ('loop of material modelling'), as already discussed in Section 3.3. However, this possibility not only invalidates the model assumption of geometry-independent material properties, but it also makes the inverse procedure for the parameter identification more complex and model predictions for specimen sizes and load situations different than the ones used for the calibration more difficult.

Hence, it remains unclear and debatable if future research should be addressed towards an extension of the examined gradient damage model (for instance, including statistical aspects of the size effect phenomenon or more parameters for describing the complex material microstructure) or towards different modelling approaches (i.e. not only the continuum approach) for the different phases of the fracture process. In other words, it is questionable if a single complex model, with many parameters to be calibrated, might provide a better performance than interacting different simple models that contain parameters with a determined and clear physical or mechanical meaning. In the last case, for instance, as already cited in Chapter 6, the continuum approach might be used to model the pre-peak micro cracking regime, while the discrete approach might be used to model the post-peak macro cracking regime, as proposed in [85].

Also the possibility of coupling multiscale analyses with inverse analysis should be investigated. For instance, as mentioned in Chapter 6, information resulting from analyses performed at the meso/microscale might be used to solve the ill-posedness at the macroscale level. Alternatively, parameter identification procedures solved at the macroscale might provide information for analyses on a lower scale. However, for simultaneous parameter identifications at different scales directly from experimental data, also measurements on different scales should be available.

Finally, the description of failure in compression represents a further step that should be examined, for a complete understanding of the mechanical behaviour of quasi-brittle materials.

8.3 Recommendations

As already pointed out in Section 3.2, the complete understanding of a real phenomenon is not possible if laboratory experiments and model develop-

ments are kept apart. Even complex experiments and complex models have limited relevance if a continuous interaction between them is neglected and comparison of the results is made only at the end for the model calibration. A fully coupled analysis of the phenomenon provides not only extraction of the maximum information out of the examined process, but also significant improvements of both the experiments (optimal experiment design), the model and the computational analysis.

In conclusion, considerable efforts should be addressed in the definition of the validity domain of the model as a tool for design, monitoring, and prediction problems, avoiding that the calibration process reduces to a mere data fitting.

Bibliography

- [1] Alifanov, O. M., Artyukhin, E. A., and Rumyantsev, S. V. (1995). *Extreme Methods for Solving Ill-Posed Problems with Applications to Inverse Heat Transfer Problems*. Begell House.
- [2] Bažant, Z. P. (1984). Size effect in blunt fracture: Concrete, rock, metal. *ASCE Journal of Engineering Mechanics*, 110(4):518–535.
- [3] Bažant, Z. P. (1991). Why continuum damage is nonlocal: Micromechanics arguments. *ASCE Journal of Engineering Mechanics*, 117(5):1070–1087.
- [4] Bažant, Z. P., Belytschko, T., and Chang, T.-P. (1984). Continuum theory for strain-softening. *ASCE Journal of Engineering Mechanics*, 110(12):1666–1693.
- [5] Bažant, Z. P. and Jirásek, M. (1994). Nonlocal model based on crack interactions: a localization study. *Journal of Engineering Materials and Technology*, 116:256–259.
- [6] Bažant, Z. P. and Lin, F.-B. (1988). Nonlocal yield limit degradation. *International Journal for Numerical Methods in Engineering*, 26:1805–1823.
- [7] Bažant, Z. P. and Oh, B. (1983). Crack band theory for fracture of concrete. *RILEM Materials and Structures*, 16:155–177.
- [8] Bažant, Z. P. and Ožbolt, J. (1990). Nonlocal microplane model for fracture, damage and size effect in structure. *Journal of Engineering Mechanics*, 116:2482–2504.
- [9] Bažant, Z. P., Ožbolt, J., and Eligehausen, R. (1994). Fracture size effect: Review of evidence for concrete structures. *Journal of Structural Engineering*, 120:2377–2398.

-
- [10] Bažant, Z. P. and Pijaudier-Cabot, G. (1988). Nonlocal continuum damage, localization instability and convergence. *Journal of Applied Mechanics*, 55:287–293.
- [11] Bažant, Z. P. and Pijaudier-Cabot, G. (1989). Measurement of characteristic length of nonlocal continuum. *ASCE Journal of Engineering Mechanics*, 115(4):755–767.
- [12] Beck, J. V. and Arnold, K. J. (1977). *Parameter Estimation in Engineering and Science*. Wiley Series in Probability and Mathematical Statistics. John Wiley & Sons, New York.
- [13] Beck, J. V. and Woodbury, K. A. (1998). Inverse problems and parameter estimation: integration of measurements and analysis. *Measurement Science and Technology*, 9:839–847.
- [14] Belytschko, T., Bažant, Z. P., Hyun, Y.-W., and Chang, T.-P. (1986). Strain-softening materials and finite-element solutions. *Computers and Structures*, 23:163–180.
- [15] Bittanti, S., Maier, G., and Nappi, A. (1984). Inverse problem in structural elastoplasticity: a kalman filter approach. In Sawczuk, A. and Bianchi, G., editors, *Plasticity Today*, pages 311–329, London. Elsevier Applied Science Publ.
- [16] Bolognini, L., Riccio, F., and Bettinali, F. (1993). A modal technique for the identification of stiffness and mass parameters in large structures. *Computational Methods and Experimental Measurements VI*, 2.
- [17] Bolzon, G., Fedele, R., and Maier, G. (2002). Parameter identification of a cohesive crack model by kalman filter. *Computer Methods in Applied Mechanics and Engineering*, 191:2847–2871.
- [18] Brekelmans, W. A. M. (1993). Nonlocal formulation of the evolution of damage in a one-dimensional configuration. *International Journal of Solids and Structures*, 30(11):1503–1512.
- [19] Brown, R. G. and Hwang, P. Y. C. (1992). *Introduction to Random Signals and Applied Kalman Filtering*. Second Edition, John Wiley & Sons, Inc.
- [20] Bui, H. D. (1994). *Inverse Problem in the Mechanics of Materials: an Introduction*. CRC Press, London.

- [21] Bui, H. D. and Constantinescu, A. (2000). Spatial localization of the error on constitutive law for the identification of defects in elastic bodies. *Archive of Mechanics*, 52 (4-5):511–522.
- [22] Carmeliet, J. (1999). Optimal estimation of gradient damage parameters from localization phenomena in quasi-brittle materials. *Mechanics of cohesive-frictional materials*, 4:1–16.
- [23] Carpinteri, A., Chiaia, B., and Ferro, G. (1994). Multifractal scaling law for the nominal strength variation of concrete structures. In M. Mihashi, H. O. and Bažant, Z. P., editors, *Size Effect in concrete structures*, pages 173–185. E&FN Spon.
- [24] Catlin, D. E. (1989). *Estimation, Control, and the Discrete Kalman Filter*. Springer Verlag, Applied Mathematical Sciences, Berlin.
- [25] Chen, J.-S., Wu, C.-T., and Belytschko, T. (2000). Regularization of material instabilities by meshfree approximations with intrinsic length scales. *International Journal for Numerical Methods in Engineering*, 47:1303–1322.
- [26] Chen, Z. and Schreyer, H. L. (1994). On nonlocal damage models for interface problems. *International Journal of Solids and Structures*, 31(9):1241–1261.
- [27] de Boer, A. (2006). *Influences of crack energy and softening branch on the load displacement diagram of the dog-bone simulation, RWS-BD-CT-P2553-06010*. Bouwdienst RWS, The Netherlands.
- [28] Dems, K. and Mróz, Z. (2001). Identification of damage in beam and plate structures using parameter dependent frequency changes. *Engineering Computations*, 18:96–120.
- [29] Dyskin, A. V., van Vliet, M. R. A., and van Mier, J. G. M. (2001). Size effect in tensile strength caused by stress fluctuations. *International Journal of Fracture*, 108:43–61.
- [30] Emery, A. F. and Nenarokomov, A. V. (1998). Optimal experiment design. *Measurement Science and Technology*, 9:864–876.
- [31] Eringen, A. C. and Edelen, D. G. B. (1972). On nonlocal elasticity. *International Journal of Engineering Science*, 10:233–248.

- [32] Feist, C. (2003). 2D and 3D experimental investigation of the crack development in plain concrete specimens. In *NW-IALAD, 'Integrity Assessment of Large Concrete Dams'*.
- [33] Ferrara, L. and di Prisco, M. (2001). Mode I fracture behavior in concrete: non local damage modeling. *ASCE Journal of Engineering Mechanics*, 127(7):678–692.
- [34] Ferrara, L. and di Prisco, M. (2002). A nonlocal approach with evolutionary internal length for the analysis of mode I fracture processes in concrete. In *15th ASCE Engineering Mechanics Conference, Columbia University, New York, NY*.
- [35] Gauss Karl Friedrich, . (1809). *Theory of the Motion of the Heavenly Bodies Moving about the Sun in Conic Sections*. Reprinted by Dover Publications, Inc., New York, 1963.
- [36] Geers, M. G. D. (1997). *Experimental Analysis and Computational Modelling of Damage and Fracture*. PhD thesis, Eindhoven University of Technology, The Netherlands.
- [37] Geers, M. G. D. (1999). *Continuum Damage Mechanics: fundamentals, higher-order theories and computational aspects*. Lecture notes, Eindhoven University of Technology, The Netherlands.
- [38] Geers, M. G. D., Borst, R. D., and Peijs, T. (1999). Mixed numerical-experimental identification of nonlocal characteristics of random-fibre-reinforced composites. *Composites Science and Technology*, 59:1569–1578.
- [39] Gelb, A. (1974). *Applied Optimal Estimation*. MIT Press, Cambridge, MA.
- [40] Grewal, M. S. and Andrews, A. P. (1993). *Kalman Filtering Theory and Practice*. Upper Saddle River, NJ USA, Prentice Hall.
- [41] Gutiérrez de la Merced M. A., . (1999). *Objective simulation of failure in heterogeneous softening solids*. PhD thesis, Delft University of Technology, The Netherlands.
- [42] Hariri, K. (2000). Bruchmechanisches Verhalten jungen Betons, Laser-Speckle-Interferometrie und Modellierung der Rissprozesszone. Deutscher Ausschuss für Stahlbeton ISSN:0171-7197 509. Berlin : Beuth, ISBN 3-410-65709-6.

- [43] Hariri, K. (2001). Fracture mechanics behaviour of concrete at early age. In *Improved Production of Advanced Concrete Structures-IPACS*. Department of Civil & Mining Engineering, Luleå University of Technology, Sweden.
- [44] Hordijk, D. A. (1991). *Local approach to fatigue of concrete*. PhD thesis, Delft University of Technology, The Netherlands.
- [45] Jacobs, O. L. R. (1993). *Introduction to Control Theory*. Second Edition, Oxford University Press.
- [46] Kailath, T., Sayed, A. H., and Hassibi, B. (2000). *Linear Estimation*. Prentice Hall, London.
- [47] Kalman, R. (1960). A new approach to linear filtering and prediction problems. (*ASME*) *J. Basic Eng.*, 82D:34–45.
- [48] Kleiber, M. (1993). Shape and nonshape structural sensitivity analysis for problems with any material and kinematic nonlinearity. *Computer Methods in Applied Mechanics and Engineering*, 108:73–97.
- [49] Kröner (1967). Elasticity theory of materials with long range cohesive forces. *International Journal of Solids and Structures*, 3:731–742.
- [50] Ladevèze, P. (1996). *Mécanique non linéaire des structures: Nouvelles approches et méthodes de calcul non incrémentales*. Hermès, Paris.
- [51] Laplace Pierre Simon (Marquis de), . (1799). *Mécanique céleste*. Tome III, No. 39.
- [52] Leblond, J. B., Perrin, G., and Devaux, J. (1994). Bifurcation effects in ductile metals with nonlocal damage. *Journal of Applied Mechanics*, 61:236–242.
- [53] Legendre Adrien-Marie, . (1806). *Nouvelles Méthodes pour la Détermination des Orbites des Comètes*.
- [54] Lehký, D. and Novák, D. (2002). Modeling of size effect in concrete under uniaxial tension. In *4th International Ph.D. Symposium in Civil Engineering*, volume 1.
- [55] Le Bellégo, C., Dubé, J. F., Pijaudier-Cabot, G., and Gérard, B. (2003). Calibration of nonlocal damage model from size effect tests. *European Journal of Mechanics. A/Solids*, 22:33–46.

- [56] Lemaitre, J. and Chaboche, J.-L. (1990). *Mechanics of Solid Materials*. Cambridge University Press, Cambridge.
- [57] Lewis, R. (1986). *Optimal Estimation with an Introduction to Stochastic Control Theory*. John Wiley & Sons, Inc.
- [58] Mahnken, R. and Kuhl, E. (1999). Parameter identification of gradient enhanced damage models with the finite element method. *European Journal of Mechanics. A/Solids*, 18:819–835.
- [59] Maier, T. (2003). Nonlocal modeling of softening in hypoplasticity. *Computers and Geotechnics*, 30:599–610.
- [60] Marcher, T. and Vermeer, P. A. (2000). Macromodeling of softening in noncohesive soils. In *Proceedings International Symposium on Continuous and Discontinuous Modelling of Cohesive Frictional Materials, Stuttgart*.
- [61] Maybeck, P. S. (1979). *Stochastic Models, Estimation and Control*. Vol. 1, Academic Press, Inc.
- [62] Mosalam, K. M. and Paulino, G. H. (1997). Evolutionary characteristic length method for smeared cracking finite element models. *Finite Elements in Analysis and Design*, 27:99–108.
- [63] Mühlhaus, H.-B. and Aifantis, E. C. (1991). A variational principle for gradient plasticity. *International Journal of Solids and Structures*, 28:845–857.
- [64] Mühlhaus, H.-B. and Vardoulakis, L. (1987). The thickness of shear bands in granular materials. *Geotechnique*, 37:271–283.
- [65] Needleman, A. (1988). Material rate dependence and mesh sensitivity in localization problems. *Computer Methods in Applied Mechanics and Engineering*, 67:68–85.
- [66] Oreskes, N., Shrader-Frechette, K., and Belitz, K. (1994). Verification, validation, and confirmation of numerical models in the earth sciences. *Science*, 263:641–646.
- [67] Ožbolt, J. (1993). General microplane model for concrete. In Wittmann, F., editor, *1st Bolomey Workshop Numerical Models in Fracture Mechanics of Concrete*, pages 173–187. A.A. Balkema, Rotterdam.

- [68] Pamin, J. (1994). *Gradient-dependent plasticity in numerical simulation of localization phenomena*. PhD thesis, Delft University of Technology.
- [69] Papalambros, P. Y. and Wilde, D. J. (2000). *Principles of Optimal Design, Modeling and Computation*. Cambridge University Press.
- [70] Peerlings, R. H. J. (1999). *Enhanced Damage Modelling for Fracture and Fatigue*. PhD thesis, Eindhoven University of Technology, The Netherlands.
- [71] Peerlings, R. H. J., de Borst, R., Brekelmans, W. A. M., and de Vree, J. H. P. (1996). Gradient-enhanced damage for quasi-brittle materials. *International Journal for Numerical Methods in Engineering*, 39:3391–3403.
- [72] Pijaudier-Cabot, G. and Bažant, Z. P. (1987). Nonlocal damage theory. *ASCE Journal of Engineering Mechanics*, 113(10):1512–1533.
- [73] Planas, J., Guinea, G. V., and Elices, M. (1998). Size effect and inverse analysis in concrete fracture. *International Journal of Fracture*.
- [74] Powell, M. J. D. (1998). Direct search algorithms for optimization calculations. *Acta Numerica*, 7:287–336.
- [75] Pukl, R., Jansta, M., Červenka, J., Vořechovský, M., Novák, D., and Rusina, R. (2006). Spatial variability of material properties in nonlinear computer simulation. In G. Meschke, R. de Borst, H. M. and Bićanić, N., editors, *Computation Modelling of Concrete Structures*, pages 891–896. Euro-c Conference, Austria, Taylor & Francis/Balkema.
- [76] Simone, A., Wells, G. N., and Sluys, L. J. (2003). From continuous to discontinuous failure in a gradient-enhanced continuum damage model. *Computer Methods in Applied Mechanics and Engineering*, 192:4581–4607.
- [77] Sluys, L. J. (1992). *Wave propagation, localisation and dispersion in softening solids*. PhD thesis, Delft University of Technology, The Netherlands.
- [78] Sluys, L. J., de Borst, R., and Mühlhaus, H.-B. (1993). Wave propagation, localization and dispersion in a gradient-dependent medium. *International Journal of Solids and Structures*, 30(9):1153–1171.
- [79] Sorenson, H. W. (1970). Least squares estimation: from Gauss to Kalman. *IEEE Spectrum*, 7:63–68.

- [80] Stavroulakis, G. E. and Antes, H. (2000). Unilateral crack identification: a filter-driven, iterative, boundary element approach. *Journal of Global Optimization*, 17(1/4):339–352.
- [81] Tang, T., Ouyang, C., and Shah, S. P. (1996). A simple method for determining material fracture parameters from peak loads. *ACI Materials Journal*, 93:147–157.
- [82] Tarantola, A. (1987). *Inverse Problem Theory. Methods for Data Fitting and Model Parameter Estimation*. Elsevier Applied Science, Southampton.
- [83] van Mier, J. G. M. (1984). *Strain-softening of concrete under multiaxial loading conditions*. PhD thesis, Eindhoven University of Technology, The Netherlands.
- [84] van Mier, J. G. M. (1997). *Fracture Processes of Concrete*. CRC Press, Boca Raton, Florida.
- [85] van Mier, J. G. M. (2004). Reality behind fictitious cracks? In Li, V. C., Leung, C. K. Y., Willam, K. J., and Billington, S. L., editors, *Fracture Mechanics of Concrete Structures*, pages 11–30.
- [86] van Mier, J. G. M. and Shi, C. (2002). Stability issues in uniaxial tensile tests on brittle disordered materials. *International Journal of Solids and Structures*, 39(13/14):3359–3372.
- [87] van Vliet, M. R. A. (2000). *Size Effect in Tensile Fracture of Concrete and Rock*. PhD thesis, Delft University of Technology, The Netherlands.
- [88] van Vliet, M. R. A. and van Mier, J. G. M. (2000). Experimental investigation of size effect in concrete and sandstone under uniaxial tension. *Engineering Fracture Mechanics*, 65 (2/3):165–188.
- [89] Vořechovský, M. and Matesová, D. (2006). Size effect in concrete specimens under tension: interplay of sources. In G. Meschke, R. de Borst, H. M. and Bićanić, N., editors, *Computation Modelling of Concrete Structures*, pages 905–914. Euro-c Conference, Austria, Taylor & Francis/Balkema.
- [90] Vree, J. H. P., Brekelmans, W. A. M., and Gils, M. A. J. (1995). Comparison of nonlocal approaches in continuum damage mechanics. *Computers and Structures*, 55:581–588.

-
- [91] Weibull, W. (1939). A statistical theory of the strength of materials. In *Royal Swedish Academy of Eng. Sci. Proc.*, volume 151, pages 1–45.
- [92] Wells, G. N. and Sluys, L. J. (2001). A new method for modelling cohesive cracks using finite elements. *International Journal for Numerical Methods in Engineering*, 50 (12):2667–2682.
- [93] Xia, S., Takezono, S., and Tao, K. (1994). A nonlocal damage approach to analysis of the fracture process zone. *Engineering Fracture Mechanics*, 48(1):41–51.

Summary

Procedures for parameter estimates of computational models for localized failure, by Cecilia Iacono

In the last years, many computational models have been developed to reproduce tensile fracture phenomena in concrete. However, their reliability is significantly related to the correct estimate of the model parameters, which not all may be directly measured during laboratory tests. Hence, the development of inverse procedures is needed, that may provide the parameters estimate minimizing, iteratively, the discrepancy between experimental and computational data. This is the main aim of the present research, focusing on the identification of the length scale parameter (or of the gradient parameter) and the slope of the softening branch of the stress-strain constitutive law of the gradient-enhanced continuum damage model.

Various issues related both to the *forward* model and to the *inverse* parameter identification problem are analyzed in the present study: the well-posedness of the inverse problem (also influenced by the choice of experimental data, in terms of quality and quantity, involved in the solution), the choice of the adopted inverse strategy (as a suitable searching scheme in terms of effectiveness, efficiency and robustness) and the assessment of the so-calibrated numerical model (in terms of limits of the predictive capabilities of the model related to size effects and loading condition effects).

For this purpose the results of four experimental series are considered: i) cable-loaded uniaxial tensile tests performed on single-edge notched sandstone specimens [86], ii) tensile size effect tests on concrete dog-bone shaped specimens [87, 88], iii) three-point bending tests on notched concrete beams [32] and iv) double-edge notched uniaxial tensile tests and single-edge notched bending tests on specimens made of the same concrete [42, 43].

The developed inverse strategy is based on two techniques used in cascade: the K-Nearest Neighbors method (KNN) and the Kalman filter (KF) method. The first method provides a preliminary study of the parameters space, while the second method represents a refining searching technique that allows to take into account the uncertainties related to both the experimental data and the model parameters estimate.

The results show that involving only global force-displacement curves of one single specimen size or of different specimen sizes in the inverse problem, a correlation between the gradient parameter c and the β parameter

exists. Hence, the uniqueness and/or stability of the inverse solution is not guaranteed. Additional local data, such as the evolution of the width of the fracture process zone during the fracture process, are needed to recover the well-posedness of the inverse problem.

Using only a single parameter set for all specimen sizes, the analyzed computational model can reproduce size effect phenomena, both related to global and local data, that are less pronounced with respect to the ones obtained in the experiments.

Moreover, parameter estimates based only on the peak loads of different specimen sizes may lead to an incorrect prediction of the model for the post peak regime.

Finally, structural effects (from three points bending tests and uniaxial tensile tests) significantly influence the inversely determined value for the length scale parameter.

Samenvatting

Strategieën voor het bepalen van modelparameters bij het simuleren van gelokaliseerde schadeprocessen, door Cecilia Iacono

De voorbije jaren werd een groot aantal modellen ontwikkeld om het bezwijkgedrag van beton onder trekbelasting adequaat te simuleren. De betrouwbaarheid van de resultaten hangt echter sterk samen met de correcte schatting van de modelparameters. Omdat deze niet allemaal rechtstreeks bepaald kunnen worden aan de hand van laboratoriumproeven winnen inverse procedures aan belang. Hierbij worden de onbekende parameters geschat door iteratief de verschillen tussen experimentele en gesimuleerde resultaten te minimaliseren. Dit is het doel van voorliggend onderzoek. De aandacht gaat daarbij voornamelijk uit naar de bepaling van de lengteschaal (of de gradient-parameter) en de helling van de 'softening' tak van de constitutieve spannings-rek relatie van het gradient-verrijkt schade continuümmodel (gradient-enhanced continuum damage model).

Een aantal aspecten van zowel het *voorwaartse* model als het *inverse* parameter identificatieprobleem is geanalyseerd in de huidige studie: de stabiliteit van het inverse probleem (beïnvloed door de experimentele data, in termen van kwaliteit en kwantiteit), de motivatie voor de toegepaste inverse strategie (in termen van effectiviteit, efficiëntie en robuustheid) en de evaluatie van het op deze wijze gekalibreerde numerieke model (in termen van de voorspellende waarde van het model voor de simulatie van schaal- en belastingseffecten).

Hiertoe worden de resultaten van vier experimentele datasets beschouwd: i) éénassige trekproeven op éénzijdig gekerfde kalkzandsteen monsters [86], ii) éénassige trekproeven op 'hondebots'-vormige proefstukken van verschillende afmetingen [87, 88], iii) driepunts-buigproeven op gekerfde betonnen proefstukken [32] en iv) éénassige trekproeven op dubbelzijdig gekerfde monsters en buigproeven op éénzijdig gekerfde monsters [42, 43].

De ontwikkelde inverse strategie is gebaseerd op twee technieken die achtereenvolgend worden toegepast: de 'K-Nearest Neighbors' methode (KNN) en de 'Kalman filter' (KF). De eerste techniek wordt gebruikt voor een verkennende studie van de parameter-ruimte, terwijl de tweede methode een nauwkeuriger zoektechniek is die toelaat rekening te houden met de onzekerheden gerelateerd aan zowel de experimentele data als de geschatte modelparameters.

De resultaten tonen aan dat de gradient-parameter c en de β parameter geen onafhankelijke variabelen zijn bij een invers probleem dat enkel gebaseerd is op globale kracht-verplaatsingsdiagrammen van één proefstuk of meerdere proefstukken van verschillende afmetingen. Zodoende kan een unieke oplossing van de inverse analyse en/of de stabiliteit van de oplossingsmethode niet worden gegarandeerd. Aanvullende locale gegevens, zoals de evolutie van de breedte van de breukzone gedurende het breukproces zijn noodzakelijk om de goede conditionering van het inverse probleem te verzekeren.

De schaaleffecten die numeriek verkregen worden door gebruik te maken van één enkele parameterset voor alle verschillende proefstukafmetingen, zijn kleiner dan de schaaleffecten die experimenteel werden gevonden. Dit geldt zowel voor de schaaleffecten gerelateerd aan globale als aan locale data.

Parameterschattingen, gebaseerd op uitsluitend de bezwijkbelasting van de verschillende proefstukken van verschillende afmetingen, kunnen bovendien leiden tot een foutieve voorspelling van de respons in het 'post-peak' regime.

Tenslotte hebben constructie-invloeden (gerelateerd aan de proefopstelling voor driepunts-buigproeven en éénassige trekproeven) een significante invloed op the lengteschaal parameter die op inverse wijze is bepaald.

Curriculum vitae

Oct. 21 st , 1971	born in Ragusa, Italy, as Cecilia Iacono
July 1990	maturit� scientifica, Liceo Scientifico Enrico Fermi, Ragusa, Italy
Dec. 1996	laurea in Civil Engineering, Politecnico di Milano, Italy
April 1997 – Dec. 1999	structural Engineer Designer, BMS, Milano, Italy
Nov. 2001 – October 2006	PhD researcher, Faculty of Civil Engineering and Geosciences, Delft University of Technology, The Netherlands

Publications from this thesis

C. Iacono, L. J. Sluys and J. G. M. van Mier, (2006) Parameters identification of a nonlocal continuum damage model. G. Meschke, R. De Borst, H. Mang , N. Bicanic (eds.), In: Proceedings of the Euro-C Conference 2006, Computational Modelling of Concrete Structures, Mayrhofen, Austria, March 2006 p. 353 - 362, A.A. Balkema, ISBN 10: 0 415 39749 9.

C. Iacono, L. J. Sluys and J. G. M. van Mier, (2006) Estimation of model parameters in nonlocal damage theories by inverse analysis techniques. In Computer Methods in Applied Mechanics and Engineering, 195, p. 7211 - 7222.

C. Iacono, L. J. Sluys and J. G. M. van Mier, (2005) Inverse estimates of fracture model parameters. In: Proceedings of the ICF XI Conference 2005, International Conference on Fracture, Turin, Italy, March 2005.

A. Simone, C. Iacono and L. J. Sluys, (2004) Determination of length

scale effect in nonlocal media. In: Proceedings of the WCCM VI in conjunction with APCOM04, Computational Mechanics, Beijing, China, September 2004, Tsinghua University Press & Springer-Verlag.

C. Iacono, L. J. Sluys and J. G. M. van Mier, (2004) Parameter identification of computational fracture model. V. C. Li, C. K. Y. Leung, K. J. Willam and S. L. Billington (eds.), In: Proceedings of the FraMCoS-5 Conference 2004, Fracture Mechanics of Concrete Structures, Colorado, USA, April 2004 p. 447 - 454, ISBN 0 87031 135 2.

C. Iacono, L. J. Sluys and J. G. M. van Mier, (2004) Inverse procedure for parameters identification of continuum damage models. In: Proceedings of the IPDO Conference 2004, Inverse Problem Design and Optimisation, Rio de Janeiro, Brazil, March 2004 p. 223 - 230, Marcelo J. Colao, Helcio R. B. Orlande and George S. Dulikravich Editors, E-papers Publishing House Ltd., ISBN 85 7650 030 2.

C. Iacono, L. J. Sluys and J. G. M. van Mier, (2003) Development of an inverse procedure for parameter estimates of numerical models. N. Bicanic, R. De Borst, H. Mang and G. Meschke (eds.), In: Proceedings of the Euro-C Conference 2003, Computational Modelling of Concrete Structures, St. Johann im Pongau, Austria, March 2003 p. 259 - 268, A.A. Balkema, a member of Swets & Zeitlinger Publishers, ISBN 90 5809 536 3.

C. Iacono, (2003) Development of an inverse procedure for parameters estimate of a gradient-enhanced continuum damage model. TU Delft Report nr. CM 2003 - 004 Faculty of Civil Engineering and Geosciences - Section of Structural Mechanics. January 2003.

Propositions

Appended to the dissertation
*Procedures for parameter estimates of computational
models for localized failure*
by Cecilia Iacono

1. A proof ab absurdo of the model can be provided by an inverse analysis, starting from the hypothesis that the model describes the physical process correctly. Possible flaws might be found at the end of the inverse analysis, that may lead to re-discuss the hypothesis, giving input for model updating, corrections or discharges.
2. Parameter estimates of models for localized failure can not only be based on the *global* force-deformation data, leaving any information on the cracked area in *local* regimes out of consideration.
This thesis.
3. Experimental tests should not be kept separated from computational model developments and used only at the end for model calibration purposes. A continuous interaction between the model and the experiments is advantageous to both and provides the deepest understanding of the studied phenomenon.
This thesis.
4. Solving an inverse problem is like reading a book backwards: you already know the end and, then, you start thinking about the plot.
5. Sometimes, if we are not sure about a theory, it might be more interesting, cheaper and more courageous to carry out just one experiment, demonstrating that we are wrong, than many experiments demonstrating that we are right.
6. We, human beings, interpret reality with bias of our mind, so according to our modelling of reality.

7. The knowledge of mankind is the product of efforts, intuitions and experiences of many generations, in every country of the world. Keeping that in mind, every individual should be stimulated to add his/her contribution for the next generation, with a respectful attitude towards all people, nations and times.

Inspired by Albert Einstein, scientist, 1879-1955.

8. Very often significant advances in science do not concern the discovery of new phenomena, but new ways of thinking and new angles of looking at old facts, which have always been in front of our eyes. Therefore, beside logic and rationality, creative imagination is also a necessary skill for a good scientist.

9. The real peace is not only the absence of war, but also a serene state of the mind that leads a single individual to live harmoniously with himself/herself and other individuals.

10. Often people are labeled by the behaviour of its worst individuals, while the efforts, sacrifices and achievements of the best ones are neglected, and yet they redeem the pride and the hope of people.

In memory of Giovanni Falcone, 1939-1992, a Sicilian judge killed in the fight against the Mafia.

11. Sometimes we are in a perpetual state of dissatisfaction, always looking far away, in all directions, for something that we already have, but that we do not appreciate. That is probably why we can not find it.

Inspired by Plato, philosopher, 427-347 BC.

These propositions are considered defensible and as such have been approved by the supervisors, Prof. dr. ir. L. J. Sluys and Prof. dr. ir. J. G. M. van Mier.

Stellingen

Behorende bij het proefschrift
*Strategieën voor het bepalen van modelparameters
bij het simuleren van gelokaliseerde schadeprocessen*
door Cecilia Iacono

1. Een bewijs uit het ongerijmde van een model kan verkregen worden door middel van een inverse analyse, vertrekkend van de hypothese dat het model het fysische proces correct beschrijft. De inverse analyse kan mogelijke gebreken aan het licht brengen. Dit kan leiden tot het herevalueren van de hypothese en kan aangeven wat er in het model moet worden aangepast, gecorrigeerd of weggelaten.
2. Parameterschattingen voor modellen met gelokaliseerde schade mogen niet enkel gebaseerd worden op globale kracht-verplaatsingsgegevens omdat dan informatie over de beschadigde zone in lokale regimes buiten beschouwing wordt gelaten.
Dit proefschrift.
3. Het is niet zinvol om experimentele tests gescheiden te houden van de ontwikkeling van nieuwe rekenmodellen en ze enkel in de laatste fase te gebruiken om het model te kalibreren. Een continue wisselwerking tussen modelleren en experimenteren leidt tot voordeel voor beiden en draagt bij tot een beter begrip van het bestudeerde fenomeen.
Dit proefschrift.
4. Een invers probleem oplossen is vergelijkbaar met een boek achterstevoren lezen: je weet al hoe het zal eindigen en dan pas begin je te denken over het plot.
5. Indien we niet zeker zijn over een bepaalde theorie, kan het soms interessanter, goedkoper en moediger zijn om één enkele proef uit te voeren die ons ongelijk aantoon, dan vele experimenten te doen om ons gelijk trachten te bewijzen.
6. Wij, mensen, interpreteren de realiteit met de vooringenomenheid van onze geest, dus volgens onze voorstelling van de realiteit.

7. De kennis van de mensheid is het resultaat van inspanningen, intuïtie en ervaringen van vele generaties, in elk land op de wereld. Met die gedachte in het achterhoofd zou elk individu zich gesterkt moeten voelen om zijn/haar bijdrage te leveren voor de volgende generatie, met een respectvolle houding jegens alle bevolkingsgroepen, naties en tijden.

Geïnspireerd door Albert Einstein, wetenschapper, 1879-1955.

8. Significante wetenschappelijke vooruitgang berust vaak niet op de ontdekking van nieuwe fenomenen, maar hangt samen met nieuwe denkwijzen en nieuwe invalshoeken om reeds lang gekende feiten te bestuderen. Daarom is, naast logica en rationeel denken, ook creatieve verbeeldingskracht een noodzakelijke vaardigheid voor een goede onderzoeker.

9. Echte vrede is niet enkel de afwezigheid van oorlog, maar ook de rustige gemoedstoestand die een individu ertoe brengt om harmonieus samen te leven met zichzelf en met andere individuen.

10. Vaak worden bevolkingsgroepen beoordeeld op basis van het gedrag van de ergste enkelingen, en worden de inspanningen, offers en prestaties van de besten over het hoofd gezien. Maar toch verdienen zij de trots en de hoop van mensen.

Ter herdenking van Giovanni Falcone, 1939-1992, een Siciliaans rechter gedood in het gevecht tegen de Maffia.

11. Soms bevinden we ons in een niet aflatende staat van ontevredenheid, altijd en overal op zoek naar iets dat we eigenlijk reeds hebben, maar niet appreciëren. En waarschijnlijk daarom is het onvindbaar.

Geïnspireerd door Plato, filosoof, 427-347 BC.

Deze stellingen worden opponeerbaar en verdedigbaar geacht en zijn als zodanig goedgekeurd door de promotoren, Prof. dr. ir. L. J. Sluys en Prof. dr. ir. J. G. M. van Mier.